Arctic Multilayer Clouds

Masterarbeit im Fach Meteorologie
von

Maiken Vassel

Februar 2018

INSTITUT FÜR METEOROLOGIE UND KLIMAFORSCHUNG
KARLSRUHER INSTITUT FÜR TECHNOLOGIE (KIT)

Referentin:	Prof. Dr. Corinna Hoose
Korreferent:	Prof. Dr. Christoph Kottmeier
Betreuerin:	Dr. Luisa Ickes

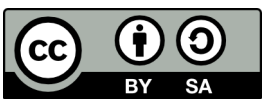

Abstract

The aim of this work is to investigate the microphysical and radiative interactions of Arctic multilayer clouds. Microphysical interaction can happen through seeding, which means that an ice crystal falls from an upper cloud into an lower cloud. In order to investigate the occurrence of seeding a detection algorithm is developed to analyse radiosounding and radar data during a one-year time period in Ny-Ålesund, Svalbard. First, height profiles of relative humidity from the radiosoundings with respect to ice are analysed to identify super- and subsaturated layers. Then the sublimation of an ice crystal of the initial size $r = 100\,\mu$m on its way through the subsaturated layer is calculated. Given that the ice crystal still exists when reaching a lower supersaturated layer, it is defined as a seeding case. Due to the fact that supersaturation does not always imply cloud activation, the seeding cases are combined with the radar images. Seeding occurs only if there also is a radar signal inside the subsaturated layer. Multilayer clouds defined by a clear interstice in the radar image do thereby not interact through seeding. A large number of supersaturation layers do not coincide with any radar cloud detection and these cases are rejected as cloud occurrence. The detection algorithm results in multilayer cloud occurrence in 37% of the investigated cases. These 37% are composited of 25% where only seeding, 6% where only non-seeding and 6% where both seeding and non-seeding occur within the same height profile. There is almost no seasonal trend. Regarding the radiative interactions of multilayer clouds a modelling study is carried out. The lower cloud does not influence the upper cloud through radiation. However, the lower cloud is influenced by the upper cloud. In case of an upper cloud the lower cloud shows less cloud top cooling. Thereby the lower cloud is thinner and contains less liquid and ice than in the case where an upper cloud is present. In the case of a lowered, more liquid and warmer upper cloud no adjustments of the lower cloud can be seen. As this stands in contrast to observations, its validity has to be questioned. The main problem of the model though seems to be the correct representation of the lower cloud in stable stratification. All in all, multilayer clouds being close enough interact trough seeding. As the distance between the multilayer clouds increases, seeding is not possible but then the multilayer clouds still interact through longwave radiation.

Zusammenfassung

Ziel dieser Arbeit ist es, die mikrophysikalischen und strahlungstechnischen Interaktionen von arktischen Multischichtwolken zu untersuchen. Mikrophysikalische Interaktion kann durch das Impfen (seeding), d.h. das Herunterfallen von Eiskristallen aus der oberen Wolke in die untere Wolke, stattfinden. Um die Häufigkeit dieses Impfens zu ermitteln, wird eine Klassifikation für Multischichtwolken entwickelt. Hierfür werden Radiosondenprofile und Radarmessungen eines einjährigen Zeitraums in Ny-Ålesund, Spitzbergen verwendet. Zuerst werden die Radiosondenprofile von relativer Feuchte bezüglich des Eises auf Über- und Untersättigung untersucht. Anschließend wird die Sublimation eines Eiskristalls der Anfangsgröße $r = 100\,\mu$m in der untersättigten Schicht berechnet. Wenn der Eiskristall noch existiert, wenn er die darunterliegende übersättigte Schicht erreicht, dann wird dieses als Impfen bezeichnet. Übersättigung geht nicht immer zwangsläufig mit Wolkenbildung einher. Aus diesem Grund wird das Auftreten von Impfen mit Hilfe von Radarmessungen verglichen. Es stellt sich heraus, dass das Impfen nur dann auftritt, wenn gleichzeitig auch ein Radarsignal gemessen wird. In Hinblick auf die Definition, nach der Multischichtwolken aus zwei Wolkenschichten mit einem sichtbaren wolkenfreien Bereich dazwischen bestehen, wird somit gezeigt, dass diese Art von Multischichtwolken nicht mikrophysikalisch interagieren können. Die Klassifikation bestätigt auch, dass ein hoher Anteil an Übersättigung nicht mit Wolkenbildung einhergeht. Diese Fälle werden daher aus der Klassifikation hinsichtlich Multischichtwolken herausgenommen. Die Klassifikation ergibt arktische Multischichtwolken in 37% der Fälle des untersuchten einjährigen Zeitraums. Diese 37% setzen sich zusammen aus 25%, bei denen nur Eiskristallimpfen, 6% bei denen zwar Untersättigung, aber kein Eiskristallimpfen und 6%, bei denen sowohl Eiskristallimpfen als auch kein Eiskristallimpfen in ein und demselben Höhenprofil stattfindet. Eine jahreszeitliche Schwankung ist kaum zu erkennen. Um die Interaktionen von arktischen Multischichtwolken in Hinblick auf Strahlung zu untersuchen, wird eine Modellstudie durchgeführt. Sie ergibt: Die untere Wolke beeinflusst die obere Wolke nicht durch Strahlung. Auf der anderen Seite wird aber die untere Wolke durch die obere Wolken beeinflusst. In Anwesenheit der oberen Wolke erfährt die untere Wolke weniger Abkühlung an ihrer Oberkante. Dadurch wird die untere Wolke dünner und enthält weniger Flüssigwasser und Eis als bei Abwesenheit der obere Wolke. In Falle einer nach unten verschobenen oberen Wolke, die mit einem höheren Flüssigwassergehalt und einer höheren Temperatur versehen ist, lässt sich kein zusätzlicher Einfluss auf die untere Wolke feststellen. Da dies im Gegensatz zu Beobachtungen steht, muss die Richtigkeit dieses Modellergebnisses in Frage gestellt werden. Eine weitere Schwierigkeit des Modells scheint es zu sein, die untere Wolke, die sich in sehr stabiler Schichtung befindet, überhaupt richtig darzustellen. Zusammenfassend lässt sich sagen, dass Multischichtwolken, wenn sie nah aneinander liegen, durch Impfen interagieren. Bei größerem

Abstand der beiden Wolken ist kein Impfen mehr möglich. In diesem Fall interagieren die beiden Wolken aber durch langwellige Ausstrahlung.

Contents

1 Motivation

Both climate prediction and weather forecast in the Arctic are challenging. This is mainly due to the lack of observations, highly variable sea ice extend and the incorrect representation of clouds in the models (Barrett et al., 2012; AROME-Arctic, 2015). Thereby often the amount of precipitation and the surface temperatures are poorly predicted. Clouds play a significant role on the surface energy budget and this is described through cloud forcing. In contrast to the mid-latitudes where clouds cool the surface, Arctic clouds, except for a few months in summer, warm the surface. This cloud forcing at the Arctic surface is mainly due to longwave cloud emission. Cloud occurrence in the Arctic is high, at about 70-95% (Intrieri et al., 2002b) and its correct description in weather models is essential. In order to do so, we need to understand Arctic clouds both in respect to their radiative impact on the surface and in respect to their microphysical composition.

Arctic boundary layer clouds are omnipresent, especially during summer, and strongly determined by their environment. The Arctic is characterised by cold air temperatures and thereby only little moisture in the air. Often does sea ice cause an insulation to the warmer sea water. When large meridional transport brings warm moist air into the Arctic, temperature and humidity inversions occur frequently (Nygård et al., 2014). Often this results in the formation of Arctic boundary layer clouds. These clouds can exist under very stable stratification and are thereby sill a great challenge in weather models when predicting the right surface temperature (Holtslag et al., 2013).

In the recent years the emphasis of research has been on Arctic mixed-phase clouds (Verlinde et al., 2007; Morrison et al., 2012; Loewe, 2017). These clouds occur frequently in the Arctic, at all heights, and exist in the temperature range between $-38\,°C$ to $0\,°C$. The microphysical challenge is here that these clouds consist of both liquid and water. Even if this is thermodynamically unstable, since the ice growths on expense of the liquid, these cloud show quasi-persistent behaviour. E.g. for the German weather model COSMO (Consortium for Small-Scale Modelling) a sophisticated description of clouds and precipitation processes has been developed (Seifert and Beheng, 2006). By using this, the hope is to account for the detailed characteristics of mixed-phase clouds and their influence on precipitation.

When Arctic boundary layer clouds and higher mixed-phase clouds coexist this is a multilayer cloud structure. There have only been a few studies on the interactions of these multilayer clouds. One example is the study of Morrison et al. (2009). They found that in models the problems connected to these Arctic multilayer clouds differ from the problems connected to Arctic single layer mixed-phase clouds. In order to improve the multilayer cloud representation in models, we first need to clarify the characteristics of Arctic multilayer clouds. Many questions about the frequency of occurrence, their impact on the surface in terms of temperature and precipitation are not answered yet. Though, before we can quantify the impacts of multilayer clouds on the surface, we first need to understand how these two clouds influence each other. For doing so, in this work I investigate the microphysical and radiative interactions of Arctic multilayer clouds. This could

help future representation of Arctic multilayer clouds in order to improve weather forecast in the Arctic.

2 Arctic Clouds: Theoretical framework

In this chapter the theoretical framework of Arctic clouds is presented. Firstly, in section 2.1 the aim is to give an insight to the microphysical processes in mixed-phase clouds and how these clouds determine cloud forcing in the Arctic. Literature used for this is mainly Lamb and Verlinde (2011); Andronache (2018); Petty (2006); Intrieri et al. (2002a,b). Secondly, in section 2.2 the concept of multilayer clouds is presented by a literature review.

2.1 Arctic Clouds

2.1.1 Cloud occurrence in the Arctic

Clouds can be divided into low boundary level clouds (up to the 800 hPa level), midlevel clouds (800 - 450 hPa) and high cirrus clouds (above the 450 hPa level) (ECMWF, 2017). As the cold temperatures in the Arctic have to be considered, the tropopause height is usually lower in the Arctic than in the mid-latitudes. Midlevel clouds therefore roughly correspond to an altitude of 1800 m to 6500 m (spring time) (Lampert, 2010) and high clouds seldom reach higher than 10 km. Out of many definitions for the Arctic, one is that of the region where the average temperature for the warmest month (July) is below 10 °C (Smithson et al., 2013). Here cloud cover is typically at about 70-95% (Intrieri et al., 2002b), but shows a great seasonal variation during a year. In figure 2.1 the monthly cloud cover frequency at different height levels is shown. In winter and springtime the percentage of clear sky is high. During polar night the energy budget of the Arctic is strongly negative, which means that more heat leaves than comes into the Arctic column (Petty, 2006; Persson and Vihma, 2017). The result is a polar surface high pressure and cold, dry and stable weather dominates. Frontal systems bringing warm, moist air masses into the Arctic are somewhat reduced compared to summer and autumn. In summertime cloud cover increases and is especially dominated by low clouds such as Arctic stratus. These clouds are generally formed through air mass modification as warm moist air is advected into the polar regions and cools radiatively. Often the Arctic stratus remains quasi-persistent for many days. In autumn, temperature contrasts between the mid-latitudes and the polar regions increase and frontal systems frequently reach the Arctic. Therefore mid-level and upper clouds become more important again compared to summertime (Curry et al., 1996; Herman and Goody, 1976; Lampert, 2010; Loewe, 2017).

2.1.2 Cloud formation: Aerosol, cloud particles and cloud phase

Aerosol occurs all over the atmosphere and is usually small particles at a size of about 0.01 to 1 μm. Aerosol is divided into primary and secondary aerosols. Primary aerosol is directly emitted into the atmosphere, either solid or fluid. Secondary aerosol has formed out of the gaseous phase due to oxidation or nucleation. Further, the origin of aerosol is either natural or anthropogenic. Examples of natural aerosol are dust, sea salt and organics like pollen or bacteria. Anthropogenic

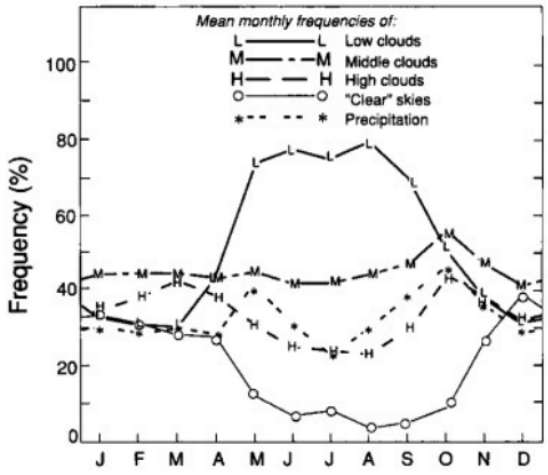

Figure 2.1: Monthly cloud cover frequency in the Arctic at different hight levels (Huschke, 1969; Houze Jr, 1993).

aerosol comes from pollution, e.g. due to burning processes. Examples are soot, sulphate and dust. In the Arctic biomass burning often occurs in Siberia and North America and dust often originates from Asia (Lathem et al., 2013). Also long-range transport of emissions from the mid-latitudes contributes to the Arctic aerosol concentration. Still, the Arctic is generally less polluted than the mid-latitudes. Variations in Arctic aerosol amount are common and here an annual cycle stands out. The maximum of the annual cycle often occurs in spring time and this is referred to as Arctic haze. This layer reaches upto 3 km height (Yamanouchi et al., 2005) and is caused by a high amount of aged aerosol, mostly containing sulphate. The aerosol originates from pollution in the mid-latitudes and reaches the Arctic due to enhanced meridional transport in late autumn. During wintertime strong surface cooling causes stable atmospheric stratification in the Arctic. Reduced turbulent mixing and little wet deposition means only few aerosol sinks. In this way, the aerosol stays in the atmosphere for a long time, slowly sinks down and accumulates in the lowermost kilometres of the Arctic atmosphere during spring. In summertime scavenging of aerosol increases and usually less aerosol is recorded.

This aerosol is needed to form liquid cloud droplets. First water saturation must be reached and secondly sufficient aerosol as cloud condensation nuclei (CCN) has to be available. In the Arctic measured CCN are often less than $100\,\mathrm{cm}^{-3}$ (Mauritsen et al., 2011). Homogeneous nucleation of cloud droplets without CCN is only possible at very high supersaturation and very unlikely in nature. Heterogeneous nucleation happens if condensation is initiated on CCN. The initial activation of the CCN is described by the Köhler theory and depends on the radius and the amount of solute. As the CCN is activated, condensation growth begins. The change of radius is given by:

$$r_d \frac{dr_d}{dt} = G(s - s_k) \tag{2.1}$$

with

$$G = \left[\frac{\rho_L R T_\infty}{M_w D_v e_s(T_\infty)} + \frac{\rho_L l_{lv}}{M_w k_T T_\infty} \left(\frac{l_{lv}}{R T_\infty} - 1 \right) s_k \right]^{-1} \tag{2.2}$$

Here r_d is the droplet radius, s the saturation of the environment and s_K the saturation equilibrium at the droplet surface due to the Köhler theory. Further there is the growth parameter G, the density of water ρ_L, the universal gas constant R, the temperature of the environment T_∞, the molecular mass of water M_w, the diffusion coefficient D_v, the equilibrium saturation pressure at the temperature of the environment $e_s(T_\infty)$, the heat transport k_T and the latent heat of condensation l_{lv}. For small radii, condensation growth is fast and slows down at bigger radii. Therefore it is only efficient until a radius of $20\,\mu$m. To form raindrops, which have sizes of approximately $100\,\mu$m, further growth processes are needed. Different particles collide due to different sizes and thereby different fall speeds. As the particles collide, they merge (coalescence). If the resulting particle is of the size of a raindrop, then the combination of collision and coalescence is called autoconversion (Lamb and Verlinde, 2011).

To form an ice crystal both homogeneous and heterogeneous ice nucleation happens. Homogeneous ice nucleation, without the help of aerosol, happens only at high supersaturation and temperatures below $-38\,°$C. For heterogeneous ice nucleation an ice forming nuclei (IN) is needed. Solid aerosols particles can act as IN, but much less aerosol is suitable to act as IN than as CCN. This depends mainly on size, chemical composition and a surface structure similar to a crystal. Especially dust, soot and organic material are IN active. There are different ways of how the solid particle and the supersaturated air can interact. Therefore heterogeneous ice nucleation is further divided into deposition freezing (vapour deposits at particle), condensation freezing (vapour condenses at particle and freezes instantaneously), contact freezing (supercooled droplet and particle collide and freeze then) and immersion freezing (particle is activated at temperatures above $0\,°$C and after cooling to a certain temperature the droplet freezes).

As soon as an ice crystal has formed, further growth is similar to condensation growth of a liquid droplet (see equation 2.1). Thereby usually regular ice crystal shapes such as plates, stellars and columns are formed (see figure 3.2). Another important ice growth mechanism is riming. Ice crystals collide with supercooled liquid and the liquid freezes at the ice surface. Besides for hail, this also plays a major role for ice growth in Arctic mixed-phase clouds (Mioche et al., 2017). Rimed particles are usually more complex and irregularly shaped and have larger fall speeds than particles only formed by condensation. Secondary ice processes, such as ice splintering, do also contribute to the amount of irregular formed ice crystals. The bounding of two or more ice crystals to a bigger snow flake is called aggregation. The ability of two ice crystals to aggregate depends on particle shape and temperature. Two stellars have elongated branches, fingers, which easily become entangled. In contrast, two columns bound less efficiently. At temperatures close to $0\,°$C, crystals might be covered by a thin film of liquid. If such two crystals collide, the liquid freezes, causes aggregation and thereby shape and size changes (Lamb and Verlinde, 2011; Loewe, 2017).

Given that enough CCN and IN are available, clouds form, when the water vapour content of air reaches saturation. Below saturation water uptake by air leads to more water vapour, while above saturation more water uptake leads to condensation. The equilibrium saturation pressure $e_l^\star$ depends on temperature T and is given by:

$$e_l^\star(T) = p_1 \exp\left(-\frac{l_{lv}}{R_v}\left(\frac{1}{T} - \frac{1}{T_1}\right)\right) \tag{2.3}$$

In the case of water saturation the latent heat of condensation l_{lv} is $2.5008 \times 10^6\,\mathrm{J\,kg^{-1}}$. p_1 and T_1 are reference values for pressure p and temperature T. At temperatures below 0 °C one has to distinguish between liquid (l) and ice (i). Saturation pressure regarding ice is given by $e_i^\star(T)$ and is calculated using the latent heat of sublimation $l_{iv} = 2.8345 \times 10^6\,\mathrm{J\,kg^{-1}}$. Since $l_{iv} > l_{lv}$, we get $e_l^\star(T) > e_i^\star(T)$. At a given temperature below 0 °C ice and supercooled water, which is liquid water at temperatures below 0 °C, can coexist. In this temperature regime and with additionally high supersaturation both ice and liquid growths. At lower supersaturation, ice saturation is reached but water saturation not yet. This regime is the most frequent one and here the Wegener-Bergeron-Findeisen process comes into play. The ice crystals grow by vapour deposition while liquid water evaporates. In the regime below ice supersaturation both ice and liquid convert into vapour (Lamb and Verlinde, 2011; Loewe, 2017; Korolev, 2007).

Besides the common cloud classification of low, middle and high clouds, another classification is possible regarding clouds' thermodynamic phase. Liquid clouds are expected when temperatures are above 0 °C. When the temperature is below −38 °C the cloud only consists of ice. In the temperature range between 0 °C and −38 °C supercooled liquid and ice can coexist and these types of clouds are then called mixed-phase clouds.

In order to measure the total amount of liquid and ice in an atmospheric column, the variables liquid water path (LWP) and ice water path (IWP) are used. Both LWP and IWP are given in $\mathrm{kg\,m^{-2}}$. The liquid water content (LWC) is the measure of liquid at each height. Analogous is the ice water content (IWC) the measure of ice at each height. Both are given in $\mathrm{kg\,m^{-3}}$, the IWC is usually one order of magnitude smaller than the LWC. The relationships between LWP and LWC and between IWP and IWC are given by:

$$LWP = \int_0^\infty LWC(z)\,dz \tag{2.4}$$

$$IWP = \int_0^\infty IWC(z)\,dz \tag{2.5}$$

In the Arctic, summertime clouds mostly contain liquid (Intrieri et al., 2002a). Cloud cover is dominated by low clouds such as stratus and these clouds are generally in a temperature range above 0 °C. LWP is at it's maximum at values about $40 \times 10^{-3}\,\mathrm{kg\,m^{-2}}$ (Curry and Ebert, 1992). In wintertime clouds mainly contain ice. Ice water path is typically at values lower than $5 \times 10^{-3}\,\mathrm{kg\,m^{-2}}$ throughout the year.

2.1.3 Mixed-phase clouds in the Arctic

Arctic mixed-phase clouds appear at about 41% of the time on an annual mean and are most frequent during transition seasons as spring and fall (Shupe et al., 2006). In contrast to mid-latitudes, where mixed-phase clouds are mainly formed through convection or synoptic-scale weather systems, in the Arctic they can persist for several days even under weak synoptic-scale forcing (Morrison et al., 2012). Further on, due to the less polluted air in the Arctic, heterogeneous ice nucleation is less effective compared to the mid-latitudes (Mauritsen et al., 2011). Therefore mixed-phase clouds are found at temperatures as low as −34 °C and at heights up to 6.5 km (Intrieri et al., 2002b). Still they are found in all levels, even in the low boundary layer (Curry et al., 1996; Curry and Ebert, 1992).

In the temperature range between -38 and $0\,°C$ the Wegener-Bergeron-Findeisen process is of importance and ice crystals grow by vapour deposition while liquid water evaporates. After a while this would lead to total glaciation and causing mixed-phase clouds to be thermodynamically unstable. In fact, Arctic mixed-phase clouds show quasi-steady behaviour. The conceptual model in figure 2.2 gives an explanation of this self-maintenance. At cloud base supercooled droplets activate and during the adiabatic ascent towards cloud top the droplets grow further (Andronache, 2018). Maximum *LWC* is usually found at cloud top. Small ice crystals start to form here, but due to the Wegener-Bergeron-Findeisen process they grow more quickly than the droplets and precipitate down (indicated by ice crystals in figure 2.2). For quasi-steady behaviour this moisture sink needs to be compensated by vapour supply. Here radiative cooling (yellow arrows in figure 2.2) at cloud top as well as large scale moisture sources come into play (Morrison et al., 2012; Shupe et al., 2013). The supercooled water at cloud top releases longwave radiation upwards towards space (light blue layer in figure 2.2). This causes cooling near cloud top and thereby turbulence is generated inside the cloud (red arrows in figure 2.2). By this, updrafts provide new moisture at cloud top. If there is a coupling to a moist surface then this can act as a moisture source. If there is no coupling to the surface advection of warm, moist air in the lower height levels close to the surface can act as a moisture source. Both the coupled and decoupled case is indicated in figure 2.2 by a simplified version of the height profile of specific humidity (q_{tot}) and equivalent potential temperature (θ_E). Savre et al. (2015) finds that any kind of moist layer below has a major importance for providing moisture to the cloud layer. Entrainment from above is almost always present. Large-scale advection of warm, moist air above (red arrows in figure 2.2) might additionally cause humidity inversions (see height profile of specific humidity (q_{tot}) in figure 2.2) that might then contribute as a significant water vapour source as well (Nygård et al., 2014; Sedlar et al., 2012). Analysing cloud dissipation, Loewe (2017) shows that drying the atmospheric layers above is of greater importance than drying the atmospheric layer below. Dry atmospheric layers above are frequently observed together with temperature inversions (Nygård et al., 2014). Final mixed-phase cloud dissipation occurs when cloud droplet number concentration decreases. A component, which contributes to this, is the decrease in CCN and IN. The reduction of CCN and IN might be induced if dry, clean air is advected and changes aerosol composition and thermodynamic profile (Loewe, 2017), or by precipitation and washout.

2.1.4 The influence of clouds on the Arctic radiation budget

A radiation budget F_{tot} is defined as

$$F_{tot} = F_{SW\downarrow} + F_{SW\uparrow} + F_{LW\downarrow} + F_{LW\uparrow}. \tag{2.6}$$

Here $F_{SW\downarrow}$ is the incoming shortwave radiation flux, $F_{SW\uparrow}$ is the outgoing shortwave radiation flux, $F_{LW\downarrow}$ is the incoming longwave radiation flux, $F_{LW\uparrow}$ is the outgoing longwave radiation flux. Positive fluxes are defined towards the surface and all fluxes are given in $\mathrm{W\,m^{-2}}$. To determine radiation fluxes, either the surface or the top of the atmosphere is used as reference point. At the surface the Arctic radiation budget F_{tot} is mainly affected by the large seasonal variation of the shortwave radiation. F_{tot} is only positive during summertime (Serreze et al., 2007).

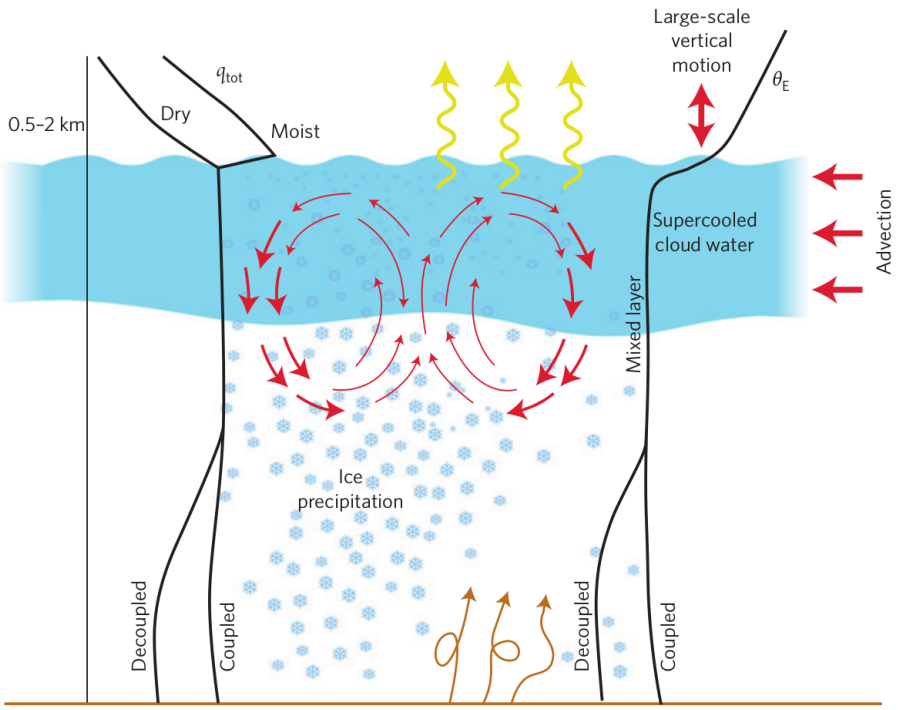

Figure 2.2: Conceptual model of an Arctic mixed phase cloud (Morrison et al., 2012)

Cloud forcing (CF) describes the impact of clouds on the radiation budget and in this way the effect of an average cloudy condition is compared to a hypothetical non cloudy condition. In the case of shortwave radiation, the cloud forcing (CF_{SW}) is given by:

$$CF_{SW} = \left(F_{SW\downarrow} + F_{SW\uparrow}\right)_{with\ cloud} - \left(F_{SW\downarrow} + F_{SW\uparrow}\right)_{without\ cloud} \tag{2.7}$$

$$\approx \frac{S}{4}(1-\alpha_c) - \frac{S}{4}(1-\alpha_g) \tag{2.8}$$

$$= -\frac{S}{4}(\alpha_c - \alpha_g) \tag{2.9}$$

$F_{SW\downarrow}$ and $F_{SW\uparrow}$ are described by the incoming solar flux S, the albedo of the cloud α_c and the albedo of the ground α_g. Considering the effects of cloud forcing at the surface, fluxes downwards are defined as positive and cause surface warming. Shortwave cloud forcing has a net cooling effect on the surface, as clouds scatter incoming sunlight back to the atmosphere. The annual average of short wave cloud forcing in the Arctic is at about $-10\,\mathrm{Wm}^{-2}$ (Intrieri et al., 2002a) with a large seasonal variation (see figure 2.3b). During wintertime there is no sunlight between October and March and shortwave cloud forcing is at zero. Towards summer an increasing solar elevation angle causes an increasing incoming solar flux S. Additionally, in summertime α_c is higher than in the rest of the year, since summer cloud occurrence is high and summer clouds often are thick. Thirdly, in summertime α_g is lower than in wintertime, since in summer there is more open water with a lower albedo than highly reflecting ice and snow surfaces. All in all, this leads to a maximum cooling ($-50\,\mathrm{Wm}^{-2}$) in the sense of shortwave cloud forcing during summer. In figure 2.3b it becomes visible, that CF_{SW} depends on cloud phase. Here the major influence on shortwave cooling is through liquid containing clouds. Spherical water droplets scatter shortwave radiation in a different way than non-spherical ice crystals. This is because many small liquid

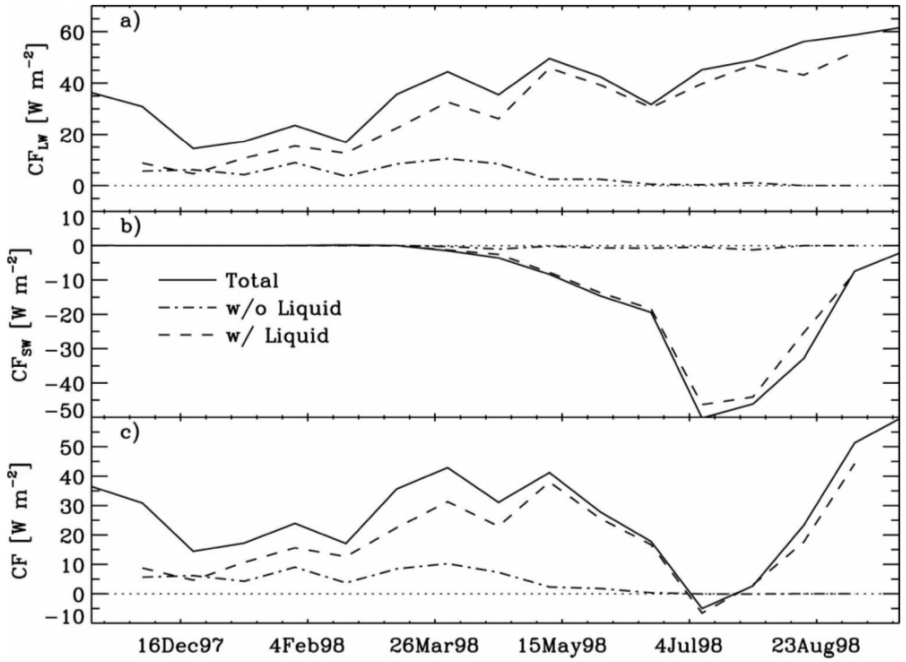

Figure 2.3: Annual cycles of a) CF_{LW}, b) CF_{SW}, and c) total CF for all clouds, those containing only liquid (dashed) and for those with only ice (dot-dashed). The curves partitioned by cloud type are weighted by cloud fraction. Data is from SHEBA (Surface Heat Budget of the Arctic Ocean), an Arctic field campaign (Uttal et al., 2002; Shupe and Intrieri, 2004).

droplets instead of relatively few large ice crystals lead to greater surface area per volume and by this higher optical depth. High optical depth means low transmittance through the cloud. In this way, the cooling effect of shortwave cloud forcing increases with increasing LWP.

Longwave cloud forcing is presented in figure 2.3a. It has a surface warming effect and the annual average in the Arctic is at about 38 Wm^{-2}. Values are a bit lower in winter than in summertime, but seasonal variation is small. Longwave cloud forcing is mainly determined by cloud temperature, height and emissivity. Mathematically, longwave cloud forcing (CF_{LW}) is given in the same way as shortwave forcing expressed in equation 2.7, but outgoing longwave flux is negligible. Further, the longwave flux is expressed by Stefan-Boltzmann's law, assuming the clouds to be gray bodies with emissivity $\varepsilon_c < 1$:

$$CF_{LW} = \left(F_{LW\downarrow}\right)_{with\ cloud} - \left(F_{LW\downarrow}\right)_{without\ cloud} \tag{2.10}$$

$$\approx \varepsilon_c \sigma T_c^4 - \varepsilon_a \sigma T_a^4 \tag{2.11}$$

T_c the temperature of the cloud, σ the Stefan-Boltzmann constant and T_a is the temperature of the atmosphere above the cloud. As cloud temperature contributes with the fourth power, it has a large impact on longwave cloud forcing. Clouds at temperatures warmer than $-15\,^{\circ}\mathrm{C}$ have the largest impact on longwave cloud forcing, while clouds at temperatures lower than $-30\,^{\circ}\mathrm{C}$ are almost indistinguishable from clear sky. In this way, 95% of radiately important clouds have cloud bases below 4.3 km (Shupe and Intrieri, 2004). In the Arctic low-level temperature inversions occur frequently. In this way considering temperature becomes even more important as low-level clouds often reside at temperatures greater than the underlying surface.

Longwave cloud forcing is dependent on cloud phase and microphysics. In figure 2.3a it becomes visible that liquid contributes more than ice does. The relationship between longwave cloud forcing and cloud microphysics comes through the emittance ε_c, which is expressed by the optical depth τ of a cloud (Petty, 2006):

$$\varepsilon_c = 1 - e^{-\tau} \tag{2.12}$$

$$\tau = Q_e \left(\frac{9\pi \cdot LWP^2 \cdot H \cdot N}{16\rho_l^2} \right)^{1/3} \tag{2.13}$$

Q_e is the extinction efficiency of the droplets, LWP the liquid water path, N the concentration of droplets, H the cloud thickness and ρ_l the cloud water density. ρ_l is proportional to the effective radius of the polydisperse cloud droplets, $\rho_l \propto r_{eff}^3$. Regarding ice the derivation is similar, using a shape factor and replacing variables by ice analogies. It becomes clear that high LWP and many droplets (N high) with small radii lead to high optical depth τ. Further, an increase in cloud optical depth leads to less transmittance and enhanced cloud forcing. Liquid water clouds have high particle concentrations and smaller particle sizes compared to ice clouds. In addition to that, LWP is usually of one magnitude greater than IWP in ice clouds. In the Arctic, ice clouds play only a significant role in wintertime, while liquid containing clouds are dominant in longwave cloud forcing throughout the rest of the year and lead to warming of the surface (see figure 2.3a). Annual mean longwave cloud forcing values are $52\,\mathrm{Wm}^{-2}$ for liquid-containing clouds and $16\,\mathrm{Wm}^{-2}$ for ice-only clouds. Longwave cloud forcing increases with LWP only until LWP becomes $30 \times 10^{-3}\,\mathrm{kg\,m}^{-2}$. Above this threshold the emissivity becomes $\varepsilon_c = 1$ and clouds emit as blackbodies. A further increase of LWP has no further impact on longwave radiation, only temperature plays an important role as it contributes with the fourth power. In the Arctic values on both sides of the threshold are common (Shupe and Intrieri, 2004).

The total net radiative effect of Arctic clouds is a warming of the surface (see figure 2.3c). This stands in contrast to the net cloud cooling effect as it is observed in the mid-latitudes. In the Arctic shortwave cloud forcing exceed longwave cloud forcing only a few months in summer (see figure 2.3c). Since a high amount of the incoming shortwave flux is reflected due to the often high Arctic surface albedo, the cooling effect of the shortwave cloud forcing is limited. In this way, longwave cloud forcing becomes more important compared to the mid-latitudes and the total net radiative effect of Arctic clouds is warming of the surface.

2.2 Arctic multilayer clouds: Definition and literature review

Multilayer clouds are frequently observed in the Arctic (Tsay and Jayaweera, 1984; Intrieri et al., 2002b; Verlinde et al., 2013). However, two different kinds of multilayer clouds are considered: Tsay and Jayaweera (1984); Intrieri et al. (2002b); Khvorostyanov et al. (2001); Liu et al. (2012) define multilayer clouds as two separate clouds with clear visible interstice in between. Verlinde et al. (2007, 2013) however describe multilayer clouds as layers inside a cloud with larger vertical extension. They detected these layers by a variable lidar signal inside a more or less continuous radar signal (see also section 4.2).

In chapter 4, where the microphysical interactions of multilayer clouds are studied, both definitions are taken into account. But in the end it is shown that only in case of the second definition microphysical interaction is possible. In chapter 6 the radiative interactions of multilayer clouds are studied and there only the first multilayer cloud definition is taken into account.

2.2.1 Occurrence of multilayer clouds

Globally, Christensen et al. (2013) analysed radar and lidar data collected by the satellite CloudSat (millimetre wavelength cloud profiling radar) and CALIPSO (Cloud–Aerosol Lidar and Infrared Pathfinder Satellite Observations). They found that the global average occurrence of multilayer clouds was 11%. For this they included data of 50 months between 2006-2011. However, they only considered oceans at night time and did not include the Arctic region. Comparing the subtropical region with the mid-latitudes, it became clear that further north the multilayer occurrence was higher. In Namibia double layer cloud amount did almost not overcome 20%, while in the North Pacific region double layer cloud amount reached values up to 30% during summer months.

For the Arctic, Intrieri et al. (2002b) evaluated multilayer cloud occurrence above pack ice during the one-year field campaign SHEBA in 1997-1998. They used ground-based lidar (returned power and depolarization ratio) and radar (reflectivity factor) to count well defined layers inside stratus clouds. Here they defined two cloud layers, if there was no cloud signal measured for at least 90 m in between. The occurrence of two cloud layers varied between 40% - 100% of monthly cloud amount. They found a seasonal trend, where between June and November the occurrence of double layer clouds was slightly higher than during the rest of the year.

Satellite detection of multilayer clouds in the Arctic was presented by Liu et al. (2012). Similar to Christensen et al. (2013), they used CloudSat and CALIPSO. Cloud detection by satellite is challenging in the Arctic, since there are only a poor thermal and visible contrast between clouds and the underlying surface of snow and ice. Additionally, only small radiative fluxes from the cold polar atmosphere and multiple temperature inversions make it even more challenging (Frey et al., 2008; Liu et al., 2004, 2009; Lubin and Morrow, 1998). The radar on CloudSat has a resolution of 2.5 km x 1.5 km. It is able to penetrate almost all non-precipitating clouds. The main errors discussed in Liu et al. (2012) were identifying cloud base in presence of precipitation and a reduced sensitivity to optical thin cirrus. The lidar on CALIPSO is more sensitive to optically thin clouds (Winker et al., 2003). In general, since surface contamination could only be neglected above a height of 960 m, low level clouds were underestimated. The data was collected between

60° N and 82.5° N and July 2006 and March 2011. The minimum considered cloud thickness was 960 m and at maximum 5 layers could be detected. The results are shown in figure 2.4. Multilayer clouds occurred between 24-28%. The seasonal cycle showed a minimum in winter, an increase in spring and summer and a maximum in autumn. Due to the high minimum considered cloud thickness (960 m) the multilayer cloud amount was most likely underestimated.

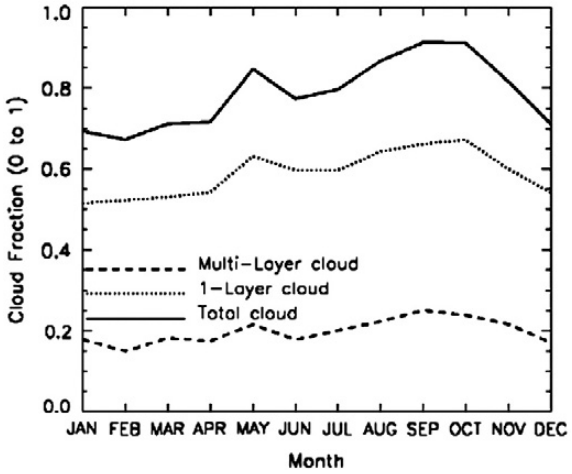

Figure 2.4: Monthly mean total cloud, single-layer cloud, and multi-layer cloud fraction. The data was collected in the Arctic between July 2006 and March 2011 (Liu et al., 2012).

2.2.2 Measurements and modelling of Arctic multilayer clouds

Both Intrieri et al. (2002b) and Liu et al. (2012) used the multilayer definition of having clear interstice (respectively 90 m and 960 m) in between two cloud layers. Such a kind of multilayer cloud is also analysed by Khvorostyanov et al. (2001) and this is presented here as an example to this kind of multilayer cloud. Khvorostyanov et al. (2001) observed a multilayer cloud on the 8 July 1998 during the SHEBA experiment in the Beaufort/Chukchi Sea. This two-layer cloud system consisted between 11:00 UTC and 13:30 UTC of a lower altostratus and an upper cirrus cloud (see figure 2.5). After 13:30 UTC the cirrus merged with the altostratus. Only with the help of a model Khvorostyanov et al. (2001) could explain the merge of the observed upper radar signal (upper cirrus cloud) with the underlying radar signal (lower altostratus cloud). They used a model that treated water and ice microphysics explicitly and this reproduced a crystalline upper cloud and a lower mixed-phase cloud. Then, in the simulations, inside the upper cloud ice crystals grew and these precipitated down.Khvorostyanov et al. (2001) used these falling ice crystals to explain the observed merge of the two clouds in the radar image.

Since other authors refer to multilayer clouds as more or less continuous layers within e.g. radar reflectivity with distinct liquid layers inside, I also give an example to this kind of multilayer cloud. During M-PACE (Mixed-Phase Arctic Cloud Experiment) Verlinde et al. (2007) observed such a multilayer mixed-phase Arctic cloud system in Alaska on 6 October 2004. Cold air originated from the sea ice, moved over open water and caused boundary layer clouds. In addition to that, a small low pressure system at mid-levels induced moistening and lead to deeper, multilayer clouds. The total cloud system reached up until 4.5 km. To analyze the cloud structure, Verlinde et al. (2007) used the lidar backscattering coefficient, the lidar depolarization ratio (see

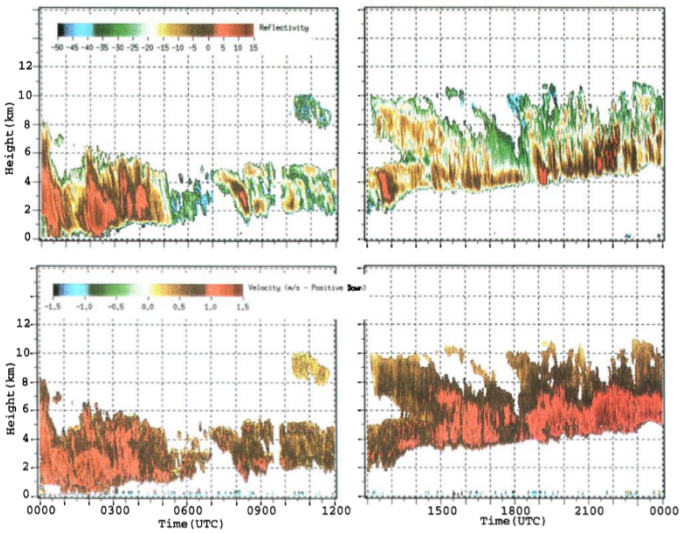

Figure 2.5: Observations: on top radar reflectivity in dBz and at bottom doppler fall velocity retrieved on the 8 July 1998 during SHEBA. The velocity is in ms^{-1} and positive is downward (Khvorostyanov et al., 2001).

figure 2.6B) and a cloud millimeter-wavelength radar (see figure 2.6A). Ice precipitation caused too strong backscatter at radar wavelengths, which made the cloud structure obscured in the reflectivity signal (see figure 2.6A). However, high lidar backscattering coefficient and low lidar depolarisation ratio (see figure 2.6B) revealed up to six liquid cloud layers. Combining both radar and lidar resulted in a hydrometeor-type map (see figure 2.6C). Here Verlinde et al. (2007) found the liquid layers to vary between 50 to 300 m in depth. In between the layers they interpreted the signals as precipitating ice of very large particles and very low concentrations.

2.2.3 Formation of Arctic multilayer clouds

The formation of multilayer clouds is not fully understood but two theories have received the most attention. These theories are now presented. Herman and Goody (1976) did a modelling study and considered one Arctic cloud containing only liquid. They concluded with that longwave radiation from cloud top to space lead to cloud-top cooling and by this to destabilisation inside the cloud. At the same time cloud droplets absorbed solar radiation. At a certain height level this became greater than the thermal cooling, and the droplets evaporated. This caused a single cloud developing into two separate clouds. The second idea about how multilayer clouds are formed, is presented by Jayaweera and Ohtake (1973) and Tsay and Jayaweera (1984). Tsay and Jayaweera (1984) analysed data gathered by airplane during the Arctic Stratus Cloud Experiment over the Beaufort Sea in June 1980. Their analyses indicated that advection of warm humid air in combination with ascending motion caused the upper cloud. The lower cloud was formed by mixing the warm air with air cooled by the pack ice. In this way the two clouds forming separately from each other.

2.2.4 The effect of multiple cloud layers on radiation

When multilayer clouds exist, they can interact microphysically, as mentioned in section 2.2.2 (and explained more in detail in chapter 3), and radiatively (discussed in chapter 6). The following

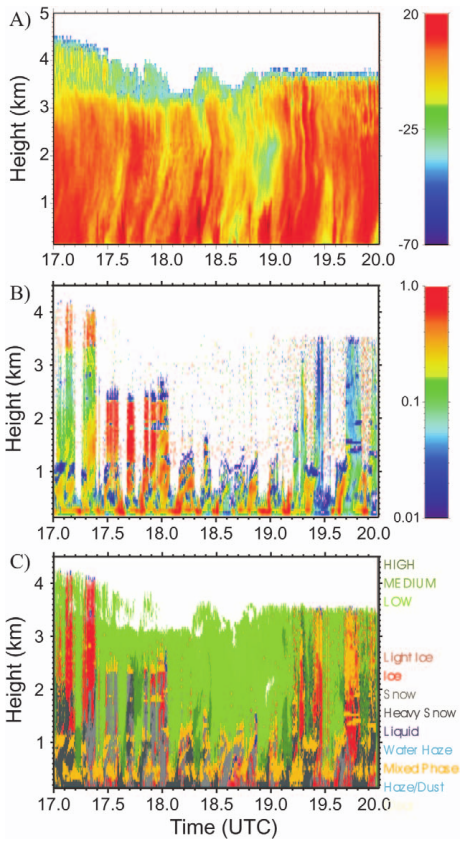

Figure 2.6: A: Radar reflectivity of the millimeter cloud radar, B: Lidar depolarization ratio and C: radar/lidar cloud phase map of the 6 October 2004 (Verlinde et al., 2007).

theoretical consideration of radiative interaction is based on Christensen et al. (2013) and shown in figure 2.7. Considering only longwave radiation (see also section 2.1.4), a single layer cloud causes warming of the Arctic surface compared to a non cloudy condition. At cloud top the cloud radiates out to space with its own temperature, according to Stefan-Boltzmann law. Examining fluxes at a level just above this cloud (at 3.5 km height in figure 2.7a)), the balance is expressed by incoming atmospheric radiation ($a1$) minus outgoing radiation from the cloud (sc =stratocumulus):

$$F_{single\ cloud} = \varepsilon_{a1}\sigma T_{a1}^4 - \varepsilon_{sc}\sigma T_{sc}^4 \tag{2.14}$$

ε_{a1} is the emissivity of the atmosphere above the cloud and T_{a1} its temperature. As the cloud has a higher temperature than the atmosphere above, this leads to cloud top cooling. If there is a cloud even higher up in the atmosphere, then this would affect the balance of the atmospheric layer in between. This is illustrated in figure 2.7b) and given by:

$$F_{between\ two\ clouds} = \varepsilon_c(1-\varepsilon_{a2})\sigma T_c^4 + \varepsilon_{a2}\sigma T_{a2}^4 - \varepsilon_{sc}\sigma T_{sc}^4 \tag{2.15}$$

ε_c is the emissivity of the upper cirrus cloud (c) and T_c is the temperature of the upper cirrus cloud. There is still the outgoing flux from the lower cloud layer (sc) and there is still the incoming flux from the atmospheric layer. As the atmospheric layer not necessarily has the same temperature as in the single layer case (figure 2.7a)) it is now called $a2$. Additionally there is the incoming

radiation from the upper cloud ($\varepsilon_c \sigma T_c^4$), but here it has to be taken into account that this is reduced by the emissivity of the atmosphere $(1-\varepsilon_{a2})$.

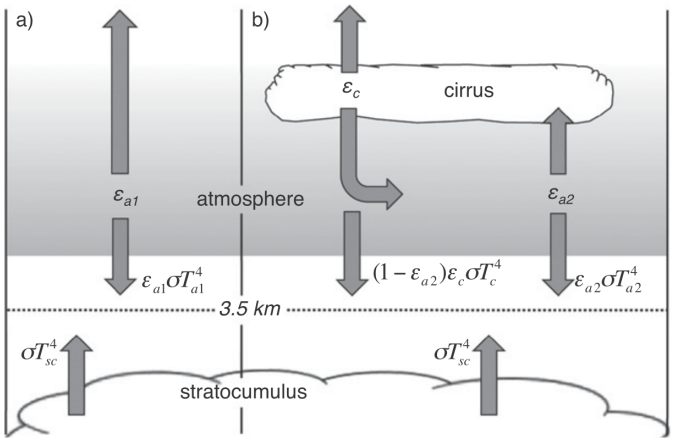

Figure 2.7: Graybody model of the atmosphere used to estimate the longwave radiative effect of a multilayer cloud in absence of solar radiation (Christensen et al., 2013). T_{sc} is the temperature at cloud top of the lower cloud. T_c is the temperature of the upper cloud. ε_{a1} is the emissivity of the atmosphere without upper cloud, ε_{a2} is the atmosphere's emissivity with upper cloud. Straight arrows represent emission and transmission and curved arrows denote absorption of longwave radiation.

To examine the effect the upper cloud has on the lower cloud, we consider the longwave cloud forcing at the level just above the upper cloud (at 3.5 km height in figure 2.7b)). We get:

$$CF_{LW,3.5km} = F_{between\ two\ clouds} - F_{single\ cloud} \tag{2.16}$$

$$CF_{LW,3.5km} = \underbrace{\varepsilon_c(1-\varepsilon_{a2})\sigma T_c^4}_{internal} + \underbrace{\sigma(\varepsilon_{a2}T_{a2}^4 - \varepsilon_{a1}T_{a1}^4)}_{external} \tag{2.17}$$

In comparison to equation 2.11 in equation 2.17 the change of the atmospheric layer $a2$ is included. The first part in equation 2.17 represents internal effects of the upper cloud that lead to an increase of incoming longwave radiation on the lower cloud. Regarding these internal effects, especially cloud temperature and optical depth are important. The second term represents the external adjustment of the atmosphere's temperature and moisture due to the upper cloud. Christensen et al. (2013) found, that since the upper cloud's temperature and cloud base are connected, a decrease in cloud base leads to an increased radiative effect. Further they found that if the optical depth of the upper cloud is more than 0.1, then the internal effects are greater than the external ones. Regarding external effects, they found that reduced emissivity of the layer in between, due to moistening, leads to reduced sensitivity of the lower cloud to the upper cloud. In this way, cloud top cooling of the lower cloud was reduced. All in all an upper cloud enhances the downwelling longwave radiation.

The incoming shortwave radiation at the top of the lower cloud is reduced by $\frac{S}{4}(1-\alpha_c)$ compared to a single layer cloud case. α_c is thereby the albedo of the upper cloud and S the incoming solar flux (see also equation 2.8). As it is shown in chapter 6, the effect of the modified incoming shortwave radiation on the lower cloud is negligible small.

2.3 Outline of the thesis

Many aspects about multilayer clouds have already been examined in previous studies, but still some questions regarding cloud interaction remain open. In the right part of figure 2.8 the important interactions between multilayer clouds are visualized. For comparison, a non cloudy situation and a single layer mixed-phase cloud situation is shown in the left part of figure 2.8. The figure represents Arctic conditions, where the surface is usually covered by snow and ice. Also special for Arctic conditions is that the non cloudy conditions cause cooling on the ground and the cloud conditions cause warming at the ground. In this environment a multilayer cloud might be formed through advection of warmer air masses at different heights (red big arrow in figure 2.8). If so, then it is reasonable that the upper cloud can be found in almost all heights in the Arctic atmosphere. But since the maximum height at which it still can influence the lower cloud, is still an open question, a height of 1-6 km is suggested in figure 2.8. If the upper cloud (right part of figure 2.8) is found in height levels higher than the single layer cloud (left part of figure 2.8), then the temperature of the upper cloud is lower than in the single layer cloud case. Consequently the outgoing longwave radiation at cloud top of the upper cloud is reduced compared to the single layer cloud top cooling (small orange arrows figure 2.8). The lower cloud layer is usually found in the Arctic boundary layer, which is usually in height levels between 0.5-2 km.
The upper and lower cloud can potentially interact both radiatively and microphysically. The effects these interactions could have on the lower cloud are marked in figure 2.8 using grey labels. These effects are discussed further in this work, but the main hypotheses are shortly summarized in the following. The upper cloud radiates in the longwave downwards (red arrow in figure 2.8). This causes warming in the intermediate layer. Thereby the cloud top cooling of the lower cloud decreases compared to the single layer case (small orange arrows figure 2.8). This decreases in-cloud mixing (red curved arrows in figure 2.8) and causes the lower cloud to be less strong than a comparable single layer cloud. Cloud interaction by shortwave radiation is of minor importance but indicated through light yellow arrows in figure 2.8. Microphysical cloud interaction is indicated by ice crystals precipitation from the upper cloud to the lower cloud (small white stars in figure 2.8).
In the following chapter 3 the question how far a falling ice crystal could survive is answered. How often the falling ice crystal then can reach the lower cloud and thereby cause microphysical interaction is evaluated in chapter 4. For this the frequency of multilayer clouds with respect to microphysical interaction is calculated using ground-based observations of radiosoundings and radar in Ny-Ålesund. In chapter 5 a model setup for the cloud resolving model COSMO is explained. In chapter 6 this model setup is used to evaluate radiative interaction. A case study is simulated and compared to measurements in order to demonstrate the impact the upper cloud has on the lower cloud.

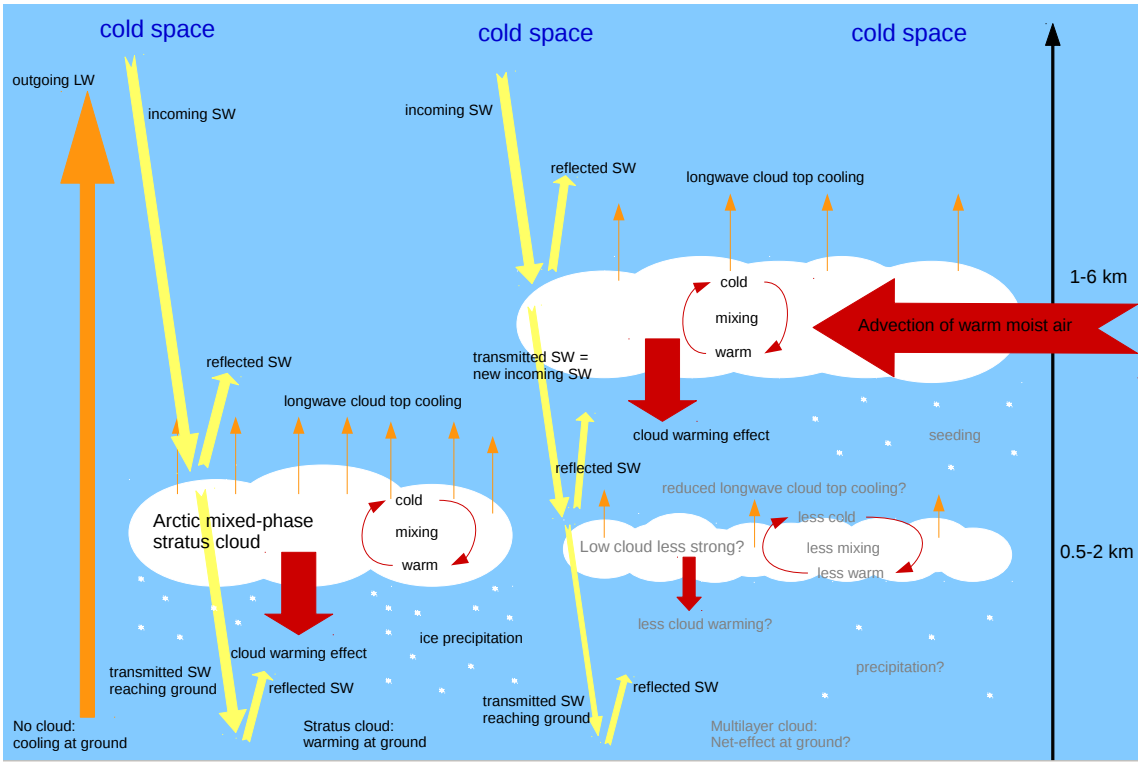

Figure 2.8: Overview of cloud interaction by Arctic multilayer clouds. The effect on the ground (cooling/warming) refers to the annual net effect, but it is also valid for all months except summer (see also section 2.1.4). *SW* means shortwave radiation and *LW* means longwave radiation. Cloud interactions with grey labels are discussed further in this work. Effects on the ground, also in grey labels, are questions for further research.

3 Microphysical interaction of two different cloud layers

Microphysical interaction by multilayer clouds could happen in the way that ice crystals could evolve in the upper cloud and, when reaching a significant size, they precipitate. In the non-cloudy intersection (subsaturated layer) between the two clouds the ice crystals sublimate (ice to vapour), which is generally a slow process. Some ice crystals could survive and then seed the lower cloud. Thereby the lower cloud is fed by these ice crystals. This mechanism is often referred to as the seeder-feeder mechanism and its different aspects are evaluated in the following.

3.1 Sublimation calculation

In order to understand the change of size of a falling ice crystal due to sublimation, the equation of droplet growth due to vapour condensation (see equation 2.1) is used, but modified for an ice crystal (Lamb and Verlinde, 2011). A subsaturated environment is considered in order to calculate the reduction of mass and thereby the reduction of radius with time of the falling ice crystal. I have

$$\frac{dm}{dt} = 4\pi C \rho_i G_i s_i \tag{3.1}$$

$$G_i = \left[\frac{\rho_i R T}{M_w D_v e_i} + \frac{\rho_i l_{iv}}{M_w k_T T} \left(\frac{l_s}{RT} - 1 \right) \right]^{-1} \tag{3.2}$$

and here m ist the mass of one ice particle and C its capacitance. The capacitance replaces the radius r of a liquid sphere and takes the shape of the ice crystal into account. A very simplified way of doing this is to use $C = \pi/2 \cdot r$ for a hexagonal plate (Seifert and Beheng, 2006; Harrington et al., 1995). ρ_i is the density of ice, G_i the growth parameter and s_i the supersaturation regarding ice. s_i is given by

$$s_i = \frac{e_i}{e_{sat,i}(T)} - 1 \tag{3.3}$$

and relates the actual ice saturation e_i to ice equilibrium saturation at a given temperature $e_{sat,i}(T)$. In the case of subsaturation, the supersaturation is less then 0. Further variables in equation 3.2 are the temperature T, the universal gas constant R, the molecular mass of water M_w and the diffusion coefficient D_v. D_v is in $\mathrm{m}^2\,\mathrm{s}^{-1}$ and I calculate it using

$$D_v = 0.211 \left(\frac{T}{T_0} \right)^{1.94} \frac{p_0}{p} \cdot 1 \times 10^{-4} \tag{3.4}$$

with $T_0 = 273.15\,\mathrm{K}$ and $p_0 = 1013.25\,\mathrm{Pa}$ (Hall and Pruppacher, 1976). Further, I have in equation 3.2 the heat transport k_T and the latent heat of sublimation l_{iv}. l_{iv} is in $\mathrm{J\,mol^{-1}}$, depends on temperature and calculated based on Murphy and Koop (2005):

$$l_{iv} = 46782.5 + 35.8925 \cdot T - 0.07414 \cdot T^2 + 541.5 \exp\left(-\left(\frac{T}{123.75}\right)^2\right) \tag{3.5}$$

By using equation 3.1 I obtain the change of mass (dm) with time (dt). In addition to that, assuming the radius-volume relation of a sphere by using $V = m/\rho_i$, a new radius is obtained at each timestep by $r = \sqrt[3]{\frac{3V}{4\pi}}$.

In the next chapter 4 the question is if an ice crystal could reach the lower cloud. In order to answer that, if only the distance to the lower cloud is known, I have to combine the mass, reduced due to sublimation, at each time with a fall speed in order to yield a fall distance. For this I use the fall speed $v(m)$ parametrisation of Seifert and Beheng (2006)

$$v(m) \cong \alpha \cdot m^{\beta} \left(\frac{\rho_{air,0}}{\rho_{air}}\right)^{\gamma}, \tag{3.6}$$

where $\alpha = 0.217\,\mathrm{m\,kg^{-\beta}}$, $\beta = 0.363$, $\gamma = 1/2$ are empiric constants for cloud ice. $\rho_{air,0}$ is $1.225\,\mathrm{kg\,m^{-3}}$. The air density ρ_{air} is given by $\rho_{air} = p/(R_s \cdot T)$, where p is the actual pressure and R_s the specific gas constant of air.

The calculation is done with the program Matlab. Thereby the forward Euler method and a timestep of 0.01 s is used. In figure 3.1 the resulting fall distance until the ice crystal is fully sublimated is shown in dependence of temperature and relative humidity with respect to ice. Dark blue areas means that the ice crystal does survive until it reaches the ground. Three different ice crystals with initial radii of r =50 μm (figure 3.1a)), 100 μm (figure 3.1b)) and 150 μm (figure 3.1c)) are used. For the same atmospheric conditions (temperature $T = -25\,^{\circ}\mathrm{C}$ and relative humidity with respect to ice $RH_i = 75\%$) an ice crystal of the size r =50 μm reaches 100 m, an ice crystal of the size r =100 μm reaches 400 m and an ice crystal of the size r =150 μm reaches 1500 m.

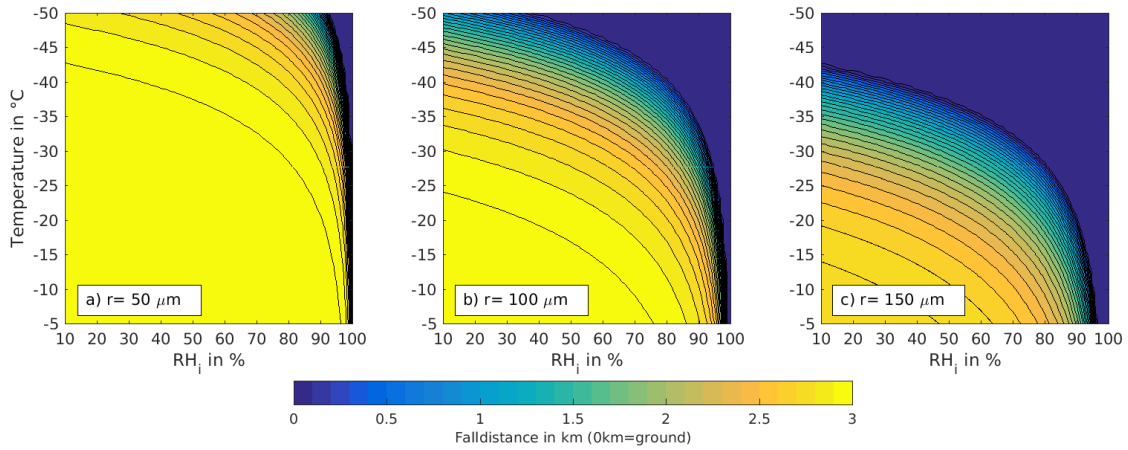

Figure 3.1: Falldistance until an ice crystal is fully sublimated, depending on relative humidity with respect to ice RH_i and temperature T_C. Initial height is 3 km and pressure $p = 750\,\mathrm{hPa}$. The initial radii are a) r =50 μm, b) r =100 μm and c) r =150 μm.

3.2 Ice crystal sizes

The potential survival of an ice crystal from the upper to the lower cloud depends to a large extend on the initial ice crystal size. Ice crystals and their growth processes are briefly described in section 2.1.2. Information on actual ice crystal sizes in the lower part of an upper cloud in a multilayer cloud system is rare. Nevertheless, Lawson et al. (2001) gave some useful informations. On 4 May 1998 during SHEBA, a mixed-layer boundary layer cloud was measured. At cloud top both small ice crystals ($r < 15\,\mu$m) as well as ice crystals up to $r = 100\,\mu$m occurred. Lawson et al. (2001) related this size inhomogeneity to possible seeding from above. They also studied a deep mixed-phase cloud extending from 2 km to 6 km. Temperatures here were between $-23\,^{\circ}$C to $2\,^{\circ}$C. On top supercooled water dominated, but further down, both at temperatures of $-10\,^{\circ}$C and $-5\,^{\circ}$C ice crystals became more frequent. At temperatures of $-10\,^{\circ}$C small ($r < 25\,\mu$m) spherical ice crystals dominated. In addition, larger ice crystals up to $r = 150\,\mu$m with mostly irregular shapes occurred. At warmer temperatures ($-5\,^{\circ}$C) secondary ice processes took place and led to large numbers, mainly spherical ice crystals.
Besides ice crystal size influencing the survival of an falling ice crystal, also the ice crystal shape matters with respect to the calculation of the fall speed. Information on different ice crystals shapes was gained by measured in Arctic low level mixed-phase clouds and the result is shown in figure 3.2. The majority are rimed crystals (green in figure 3.2), followed by stellars (blue in figure 3.2) and plates (rose in figure 3.2).

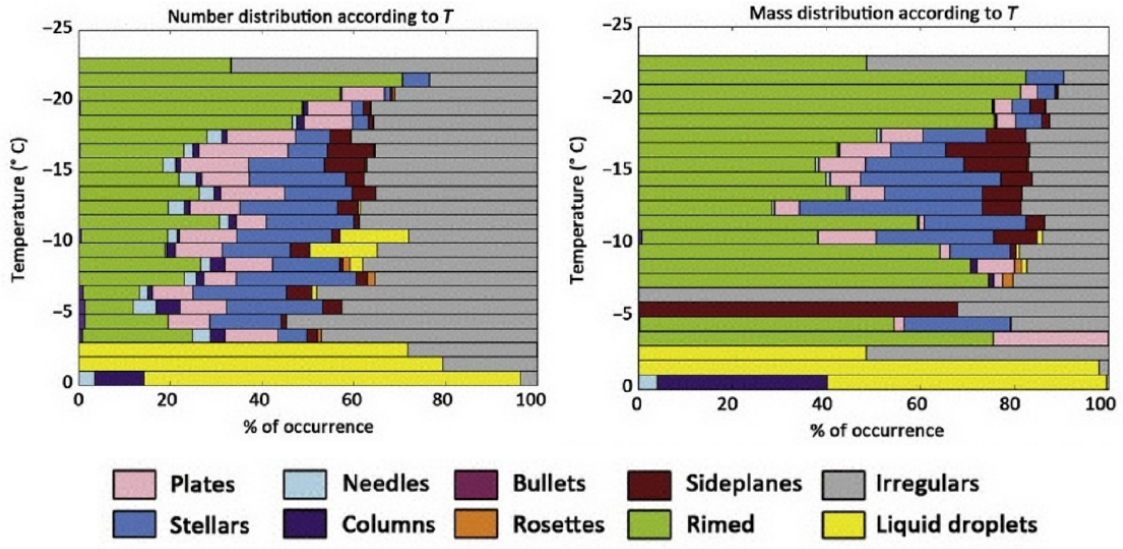

Figure 3.2: Ice particle shape distribution in dependence of temperature. Number distribution is on the left, mass distribution is on the right. The data was gathered in low lewel mixed-phase clouds during different Arctic field campaigns (Andronache, 2018; Mioche et al., 2017).

3.3 Specifications for the classification

In the following chapter 4 ice crystal sizes of $r = 50\,\mu$m, $100\,\mu$m and $150\,\mu$m are considered. This is in good agreement with the bigger crystals observed by Lawson et al. (2001). The main focus is on the size of $r = 100\,\mu$m. In addition to the ice crystal growth processes presented in

section 2.1.2, the ice crystal is also modified by ice splintering and melting processes and this causes shape irregularities and size modifications. Additionally riming (ice crystal collides with supercooled droplet) plays an important role (see figure 3.2) and leads to an increase in mass and fall speed, but almost not in size (Andronache, 2018). Therefore it is difficult to not only specify a correct ice crystal size but also a correct fall speed. I use the fall speed of Seifert and Beheng (2006) modified for an ice crystal (equation 3.6). This fall speed is only slightly reduced compared to the one specified for a sphere (Seifert and Beheng, 2006). Further, to keep my calculation realistic, I use measured atmospheric conditions of height, pressure, temperature and relative humidity with respect to ice for each specific subsaturated layer. The measured variables are then averaged over the total subsaturated layer. A limitation of the calculation is that a further moistening of the subsaturated layer due to the sublimated ice crystal is not considered. Also only a single ice crystal, and not a polydisperse distribution is considered. Eventual modifications due to a higher ice crystal number are not taken into account.

4 Classification of Arctic multilayer clouds

In order to understand how realistic it is that an ice crystal survives the subsaturated layer and reaches a lower cloud layer (seeding) the calculation from the previous chapter 3 is applied to real case meteorological conditions. Meteorological conditions in Ny-Ålesund are taken from radiosounding measurements. Thereafter the occurrence of seeding and non-seeding cases is linked to cloud occurrence derived by cloud radar measurements. In the end a classification about seeding and non-seeding cloud occurrence is obtained, which is used to evaluate if and how often microphysical interaction between two cloud layers is possible.

4.1 Climate in Ny-Ålesund

Ny-Ålesund at the northwestern part of Svalbard is located at 78°55′24″ N and 11°55′15″ E (see figure 4.1). Compared to other places at the same latitude, Ny-Ålesund shows high tropospheric temperatures. The annual mean temperature is −5.2 °C (Førland et al., 2011). The climate in Ny-Ålesund is strongly influenced by heating from the warm and all-year-ice-free Atlantic Ocean. The Atlantic Ocean is to the west of Ny-Ålesund, while a bigger glacier system is located to the east. Wind directions are generally southeast-nothwest and nothwest-southeast, as this is the orientation of the fjord-valley system. Arctic warming is visible in the annual mean temperature with a increase of +1.3 °C ± 0.7 °C per decade in the period 1994 to 2013 and is strongest in winter (Maturilli and Kayser, 2017; Maturilli et al., 2015).

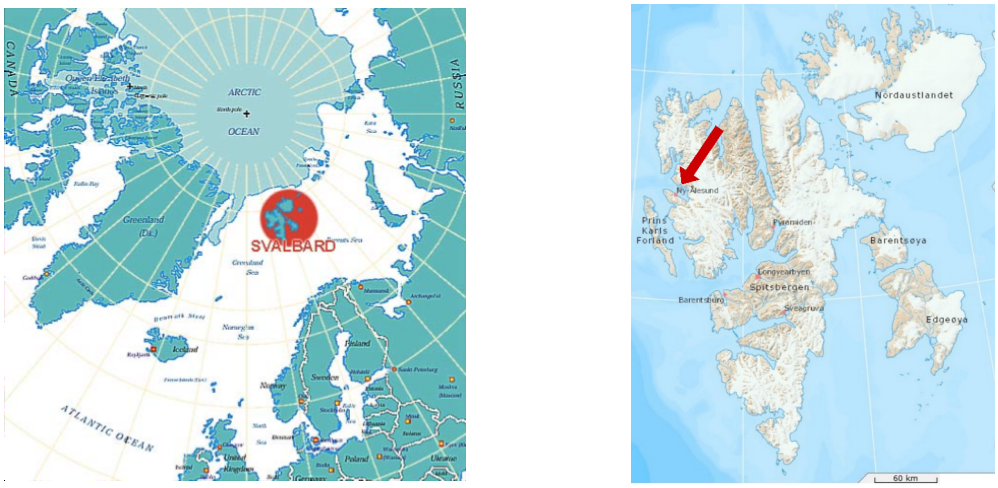

Figure 4.1: Left: Red circle indicates the location of Svalbard in the world (Noahhowell, 2018). Right: Map over Svalbard. Ny-Ålesund is in the northwest of Svalbard. The glacier system to the east of Ny-Ålesund is indicated in white (Norwegian Polar Institute, 2018).

4.2 Datasets used for the cloud classification

Daily radiosoundings were launched since October 1991 onwards. I use the profiles of time, height, pressure, temperature, relative humidity and wind for the one-year period 10 June 2016 to 9 June 2017. In order to additionally get a more reliable answer regarding a seasonal trend, I also do a test with the data between 1 January 1993 - 9 June 2017. Few days with multiple radiosoundings occur, but usually the soundings are done once per day at around 12 UTC. For the time period 1 of January 1993 - 31 of December 2014 the radisounding data was provided by Maturilli and Kayser (2016). The vertical resolution was interpolated to 50 m between 50 m and 10 km height and 100 m between 10 km and 30 km height. Between 21 of May 2006 - 11 of April 2017 the radiosounding data was certified through GRUAN (Gruan, 2017) and had a vertical resolution of 1 s^{-1}. This equals approximately 5 m between 15 m and 30 km height. Since 12 of April 2017 onwards the radiosounding data was available through Maturilli (2017) with a vertical resolution of 1 s^{-1}.

In addition, data from ground-based radar is used and in section 4.5.2 the use of ground-based lidar is discussed. The measurement principle of both a radar (radio detection and ranging) and a lidar (light detection and ranging) is to send out out a signal of a given wavelength. Particles in the atmosphere scatter this signal and then the radar and lidar receives a signal back. Due to the different wavelength of radar and lidar the received information is different. A lidar is usually more sensitive to small particles such as aerosol and the signal is often attenuated in the lower part of a cloud. A radar usually reaches through the total cloud and is more sensitive to bigger particles such as rain droplets. A 94-GHz Doppler radar has been measuring in Ny-Ålesund since 10 June 2016. The cloud radar is part of the (AC)³ project (Arctic Amplification: Climate Relevant Atmospheric and Surface Processes and Feedback Mechanisms), and belongs to the University of Cologne (see acknowledgements in section A.12). The Radar has a potential maximum vertical resolution of 6 m (the data used here has a vertical resolution of 20 m), reaches up to 10 km height and measures continuously with a temporal resolution of 30 s. A detailed description is found in Küchler et al. (2017).

The radar receives a signal (radar reflectivity). This is given by the radar equation and depends on the radar antenna, the distance to the reflecting particle, atmospheric attenuation and particle specifications. Considering only particle specifications and assuming only spherical particles (Rayleigh scattering), the received signal η can be expressed by

$$\eta = \int_0^\infty \sigma(\pi, D) n(D) dD \tag{4.1}$$

$$= \frac{\pi^5}{\lambda^4} |K|^2 \int D^6 n(D) dD \tag{4.2}$$

$$= \frac{\pi^5}{\lambda^4} |K|^2 Z. \tag{4.3}$$

λ is the radar specific wavelength, $n(D)$ the particle number distribution, $\sigma(\pi, D)$ the scattering cross section, $|K|^2$ the dielectric factor and Z the radar reflectivity factor. Since the radar reflectivity η depends on the radar specific wavelength λ, η is not a useful tool for radar data comparison. Instead the radar reflectivity factor Z is used. Z expresses the ratio between sent and received signal and is given in $\mathrm{mm}^6\ \mathrm{m}^{-3}$. The scattering cross section $\sigma(\pi, D)$ (in equation 4.1) describes how a single particle scatters the energy backwards in π direction. Further the scattering cross section is dependent on particle size D and the dielectric factor $|K|^2$. The dielectric factor depends on particle phase, material, wavelength and temperature. For ice the dielectric factor is much lower than for water. In summary, the radar reflectivity factor Z becomes proportional to the 6^{th} power of particle size

$$Z = \int D^6 n(D) dD \tag{4.4}$$

and the largest particles dominate the signal. In mixed-phase clouds this means that large ice particles rather than smaller liquid droplets dominate the signal and the detection of liquid layers becomes difficult.

The radar is able to measure a change in frequency of the received compared to the sent signal. This frequency shift is due to the doppler effect as the particle moves in radial direction towards the radar. Since the radar is looking upwards, the doppler velocity equals the vertical velocity and positive velocities means upward particle motion. The vertical velocity is both due to turbulence as well as due to particle sedimentation. The signal has not been corrected for rain and melting-layer attenuation. Therefore the highest downward values occur during summer in the lowest part when rain falls below the melting layer. The spectral width shows the variation in vertical velocity. High spectral width means various fall velocities and this can be interpreted as a mix of particle sizes.

As the radar reflectivity factor is the zeroth moment, the doppler velocity is given by the first moment and the spectral width is given by the second moment. In this way these variables can easily be derived and in figure 4.2 an example of 3 November 2016 in Ny-Ålesund is shown. The data was provided in a way that the variables have been corrected for gaseous and liquid attenuation. The calibration was done so that a cloud at 273 K containing $1 \times 10^6\ \mathrm{m}^{-3}$ droplets of $D = 100\ \mu\mathrm{m}$ has a reflectivity factor of 0 dBZ at all frequencies.

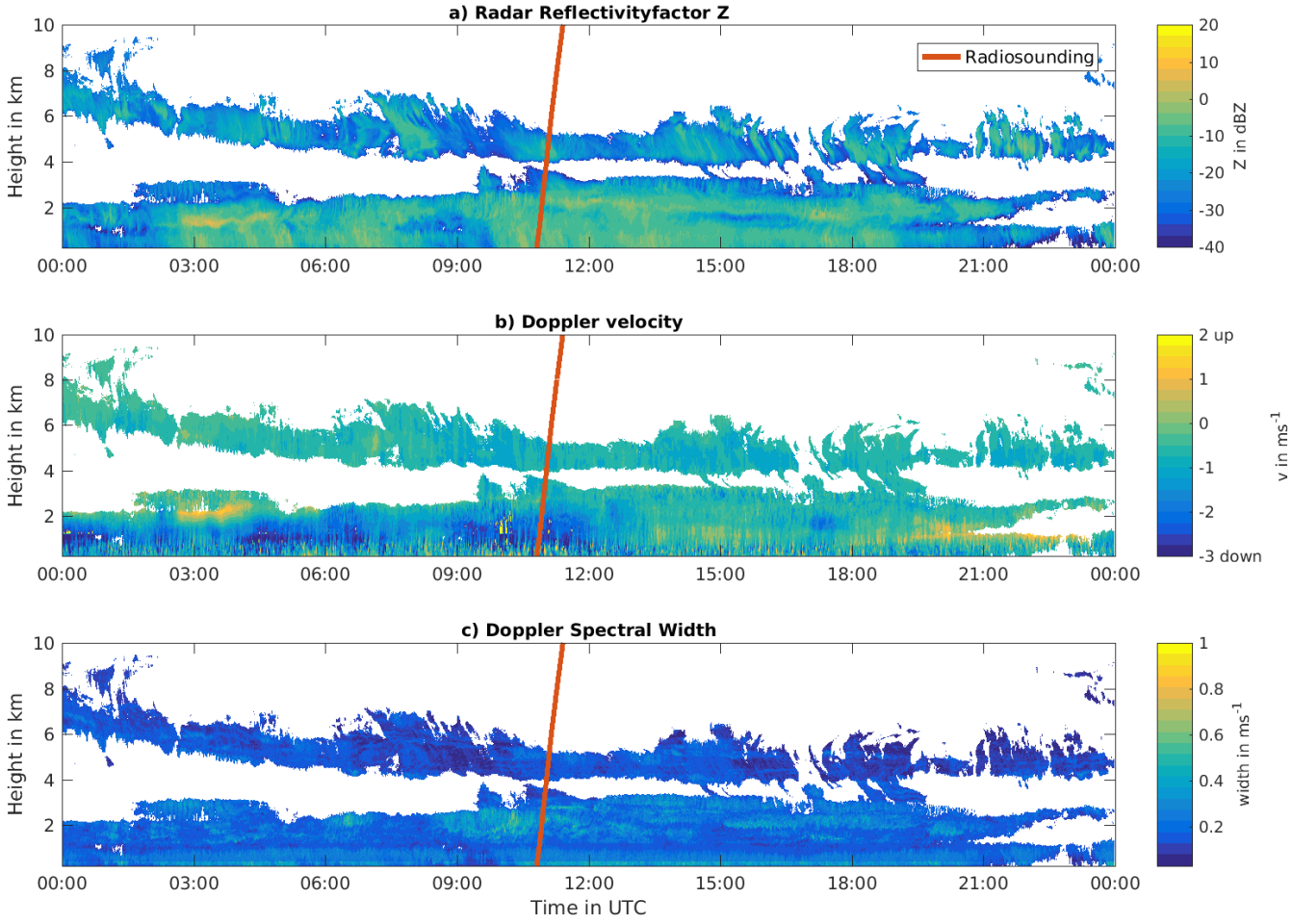

Figure 4.2: 3 November 2016 in Ny-Ålesund: a) Radar reflectivity factor, b) doppler velocity and c) doppler spectral width. The red line indicates the radiosounding used on that day. Data source: see acknowledgements in section A.12.

4.3 Detection algorithm for radiosonde profiles and analytical calculation of ice crystal sublimation

In order to answer the question if microphysical cloud interaction is possible, the frequency of potential survival of a sedimenting ice crystal between two cloud layers is calculated for real case scenarios taken from Ny-Ålesund. First the relative humidity measured by the radiosoundings is analysed to define subsaturation ($RH_i < 100\%$) and supersaturation ($RH_i > 100\%$) layers. Secondly the calculation of section 3 is applied to the derived subsaturated layers. Hereby the average conditions of temperature, pressure and moisture of the individual subsaturated layers, measured by the radiosounding, is included in the calculation. Thirdly seeding cases are defined as those where the ice crystal reaches the supersaturated layer below, and non-seeding cases as those where the ice crystal sublimates fully before reaching the supersaturated layer below. Furthermore, this detection algorithm is then in section 4.4 extended by the radar measurements.

4.3.1 Methods

During the time period of one year between 10 June 2016 - 9 June 2017 radiosounding data is analysed regarding subsaturated layers. The data is evaluated between 0 km and 10 km height. For each day one radiosounding is chosen, usually at 12 UTC. On days with more than one radiosounding, the one at 12 UTC is chosen. On 19 May 2017 no radiosounding at 12 UTC occurred, and therefore the one at 16 UTC is chosen instead. The radiosoundings of 1 May 2017 and of 23 May 2017 contain errors and are therefore not considered further. Days, where the radar data is missing, are also not considered. For total 278 days out of 365 days a suitable radiosounding and radar data is available.

The radiosounding's relative humidity with respect to water is used in combination with temperature and the Magnus' formula for ice saturation to calculate the relative humidity with respect to ice. In the left part of figure 4.3 the relative humidity is shown for 3 November 2016 in Ny-Ålesund. In the right part of figure 4.3 the resulting cloud is visualised by the radar reflectivity factor (further details in section 4.4.1). As threshold for sub- and supersaturation 100% relative humidity with respect to ice is used (see red horizontal lines in figure 4.3). Subsaturated layers reaching down to the ground or reaching higher than 10 km are not considered further, as these layers do not contribute to multiple cloud layers. If the temperature at certain levels is above 0 °C, then relative humidity with respect to water is chosen for limiting the subsaturated layer (16 July 2016, see figure A.1). This occurs at low levels in summer, but is by far less often than having higher relative humidity with respect to ice. Subsaturated layers between two supersaturated layers with respect to water are not considered, as they are not relevant for ice crystal seeding (1.3 km to 0.6 km at 16 July 2016, see figure A.1). Layers of supersaturation thinner than 100 m are not considered (at 3.3 km and at 9.6 km height at 16 July 2016, see figure A.1). Regarding subsaturation originally no minimum thickness threshold was set. However, a small minimum thickness threshold (data screening) turns out to be useful for the subsaturation detection. Due to different vertical resolution of radiosounding and radar, either, if radar is available, at least two radar points (20.0 m distance) and at least three radiosounding grid points are set as mimimum thickness threshold. Since the vertical resolution of the radiosounding varies, this data screening

is usually less than 20.0 m, but the maximum of 21.7 m occurs at 27 July 2016 (see figure A.2). An example of data screening based on the radar data is at 9.1 km height at the 13 August 2016 (see figure A.3).

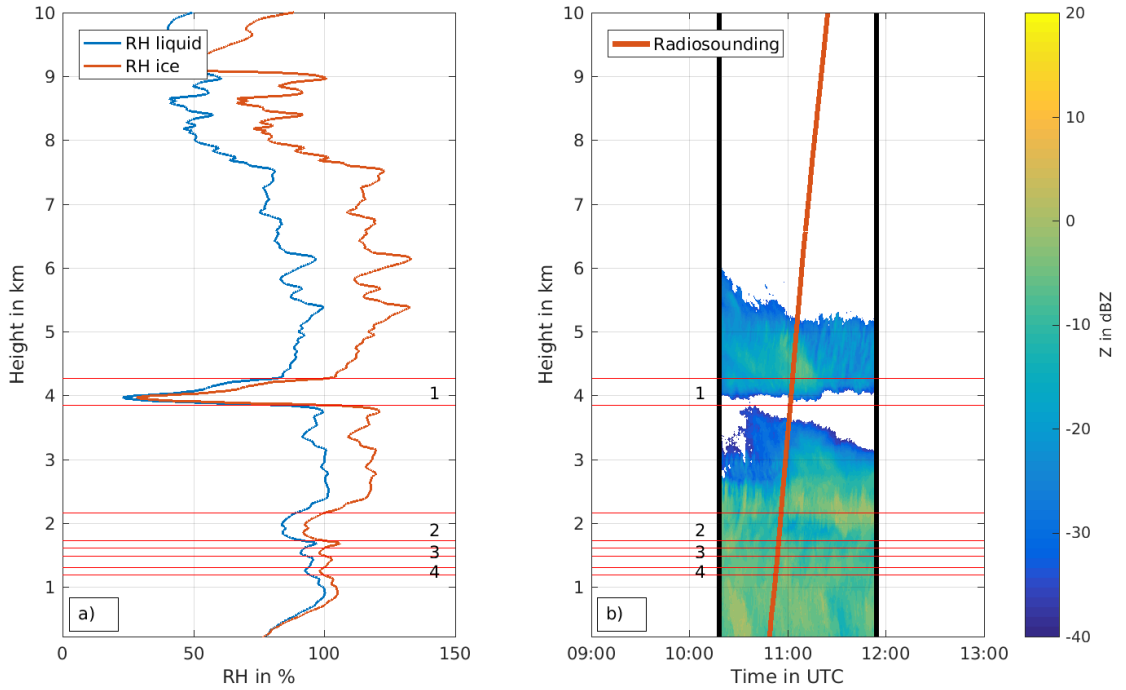

Figure 4.3: 3 November 2016: a) Radiosounding between 10:48 -11:24 UTC (0 km and 10 km height) in Ny-Ålesund (Data: Gruan (2017)). Relative humidity with respect to water in blue and relative humidity with respect to ice in red. b) Radar reflectivity factor Z at 3 November 2016 in Ny-Ålesund (Data source: see acknowledgements in section A.12). The red vertical line visualises the radiosounding. The black vertical lines visualise the time period considered for the radar data. The red horizontal lines and the numbers 1, 2, 3 and 4 visualise the subsaturated layers.

In the next step the potential survival of an falling ice crystal in the subsaturated layers is calculated. The general assumptions are explained in section 3.1. For the begin of falling the height, where supersaturation turns into subsaturation, is chosen. For the end of falling the height, where the same subsaturation again turns into supersaturation lower down, is chosen. For the subsaturated layers the mean temperature, pressure and relative humidity with respect to ice are calculated and included in the sublimation calculation. For the 3 November 2016 this results in four subsaturated layers (red horizontal lines in figure 4.3). The first layer is at 4.26 km top height (see layer number 1 in figure 4.3), the second layer at 2.15 km top height (see layer number 2 in figure 4.3), the third layer at 1.60 km top height (see layer number 3 in figure 4.3) and the fourth layer at 1.30 km top height (see layer number 4 in figure 4.3). The sublimation calculation for the subsaturated layers at 4.26 km (layer 1 in figure 4.3) and at 2.15 km (layer 2 in figure 4.3) are shown in figure 4.4 and 4.5. In the subsaturated layer at 4.26 km only the $r = 150\,\mu$m ice crystal reaches the supersaturated layer below (see purple line in figure 4.4). In the subsaturated layer at 2.15 km both the $r = 100\,\mu$m and $150\,\mu$m ice crystals reach the supersaturated layer below. In the subsaturated layers at 1.60 km and 1.30 km all three ice crystals reach the supersaturated layer below (see figure A.4 and A.5).

In the following a **seeding case** means an ice crystal reaching the supersaturated layer below. A **non-seeding case** means that the given ice crystal does not reach the lower next supersaturated layer because it sublimates. Thereby the three ice crystal sizes $r = 50\,\mu$m, $100\,\mu$m and $150\,\mu$m are considered.

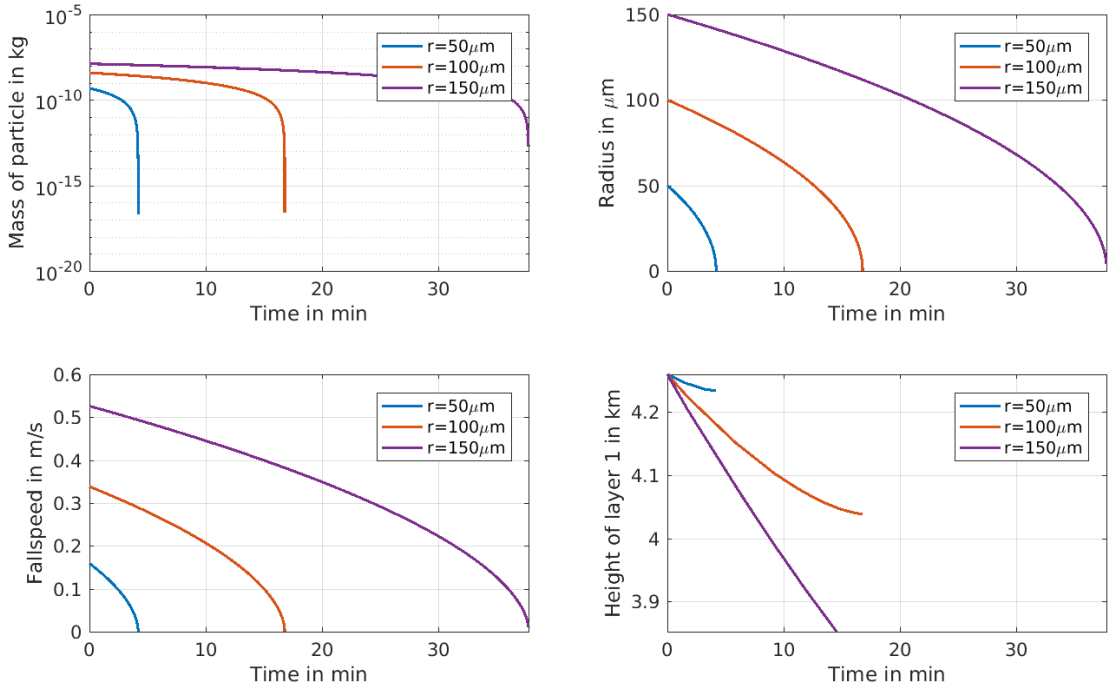

Figure 4.4: Sublimation calculation for the subsaturated layer between 4.26 km and 3.85 km height (layer 1 in figure 4.3) at 3 November 2016. Average values were pressure $p = 605.85$ hPa, temperature $T = -21.17\,°$C and relative humidity with respect to ice $RH_i = 62.17\,\%$. Initial sizes are $r = 50\,\mu$m, $100\,\mu$m and $150\,\mu$m. The height plot shows only the height level of the subsaturated layer between 4.26 km to 3.85 km. Only the $r = 150\,\mu$m ice crystal reaches the supersaturated layer below.

4.3.2 Results

The first part of the detection algorithm is to detect the subsaturated layers ($RH_i < 100\%$) in the radiosounding profiles. The second part of the detection algorithm is to calculate if seeding into the supersaturated layer below could happen (seeding cases) or not (non-seeding cases). In order to understand how often microphysical cloud interaction is possible now derive the frequency of seeding and non-seeding cases is derived. Applying the detection algorithm to the time period 10 June 2016 - 9 June 2017 results in five categories as shown in figure 4.6. Seeding and non-seeding refers to an ice crystal of the size $r = 100\,\mu$m. Seeding means that the ice crystal survives until the next supersaturated layer, non-seeding means that the ice crystal sublimates fully before reaching the next supersaturated layer. 100% equals 269 days, whereby days refers only to the time of the radiosounding ($\sim$ 1 hour at 12 UTC). In figure 4.6 (and all following figures) the displayed percentages are rounded to whole numbers. 6% do not have a single supersaturated layer (blue in figure 4.6). These days are assumed to be clear sky days. Days with only one single supersaturated layer occur in 18% (green in figure 4.6). These days are assumed to be single cloud layer days. In 23% (yellow in figure 4.6) + 40% (orange in figure 4.6) + 12% (red in figure 4.6) of the cases

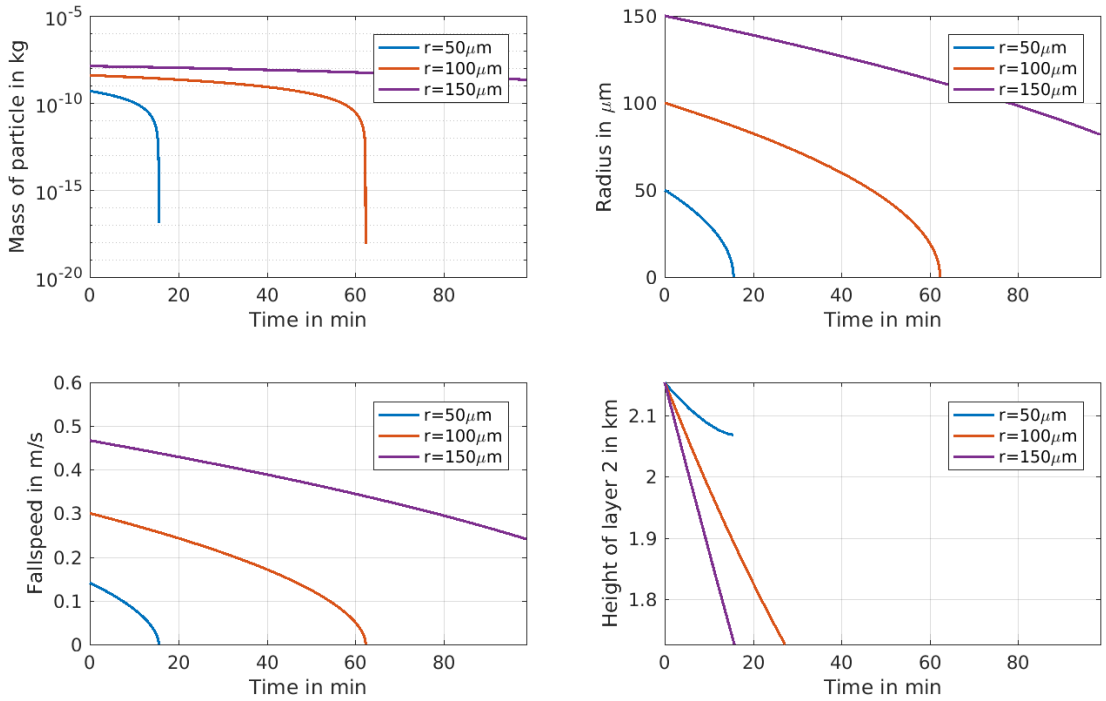

Figure 4.5: Sublimation calculation for the subsaturated layer between 2.15 km and 1.73 km height (layer 2 in figure 4.3) at 3 November 2016. Average values were pressure $p = 803.5$ hPa, temperature $T = -9.86\,°C$ and relative humidity with respect to ice $RH_i = 94.46\,\%$. Initial sizes are $r = 50\,\mu$m, $100\,\mu$m and $150\,\mu$m. The height plot shows only the height level of the subsaturated layer between 2.15 km and 1.73 km height. Both the $r = 100\,\mu$m and $150\,\mu$m ice crystals reach the lower supersaturated layer.

more than one subsaturated layer (e.g. see figure 4.3) occur. These days are assumed to be potential multilayer cloud days. Here a further separation into different categories is done. 'Only seeding' (yellow in figure 4.6) means that all subsaturated layers on that day are seeding cases. 'Both seeding and non-seeding' (orange in figure 4.6) means during that day some subsaturated layers are seeding cases and others are non-seeding cases. 'Only non-seeding' (red in figure 4.6) means that during that day all subsaturated layers are non-seeding cases. The 3 November 2016 belongs to the category 'both seeding and non-seeding' (orange in figure 4.6 and see also figures 4.4, 4.5, A.4 and A.5).

Since the ice crystal size is a large uncertainty in the calculation (see also figure 3.1), the detection algorithm is additionally applied to an ice crystal of the sizes $r = 50\,\mu$m and $150\,\mu$m. These plots are shown in figure A.6 and A.7. A smaller ice crystal leads to less seeding cases and a bigger ice crystal leads to more seeding cases. The impact the different ice crystal sizes have on the distribution of the different categories is noticeable. In the category 'only seeding' there is approximately a doubling in percentage from each ice crystal size to the next (10%, 23% and 37% for $r = 50\,\mu$m, $100\,\mu$m and $150\,\mu$m). In the category 'both seeding and non-seeding' the impact of the variation in ice crystal size is less strong (44%, 40% and 41% for $r = 50\,\mu$m, $100\,\mu$m and $150\,\mu$m). In the category 'only non-seeding' the impact of the variation in ice crystal size is highly noticeable again (22%, 12% and 8% for $r = 50\,\mu$m, $100\,\mu$m and $150\,\mu$m). In the following the main focus is on the size $r = 100\,\mu$m, but I also keep the large impact of ice crystal size in mind.

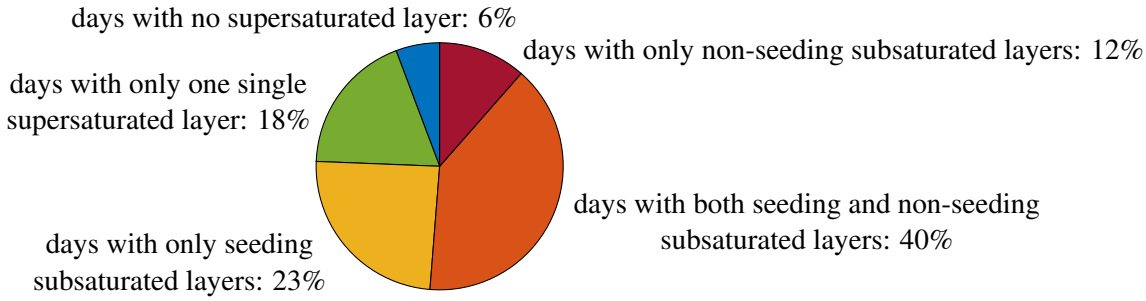

Figure 4.6: Relative distribution of days of different cloud occurrences between 10 June 2016 - 9 June 2017. 100% equals 278 days. Seeding and non-seeding is calculated using an ice crystal of the size $r = 100\,\mu$m.

The temporal evolution throughout the year for an ice crystal of the size $r = 100\,\mu$m is shown in figure 4.7. A seasonal trend in between months is not visible. Similar plots for $r = 50\,\mu$m and $150\,\mu$m are shown in figure A.8 and A.9, but also there no seasonal trend in between months occurs.

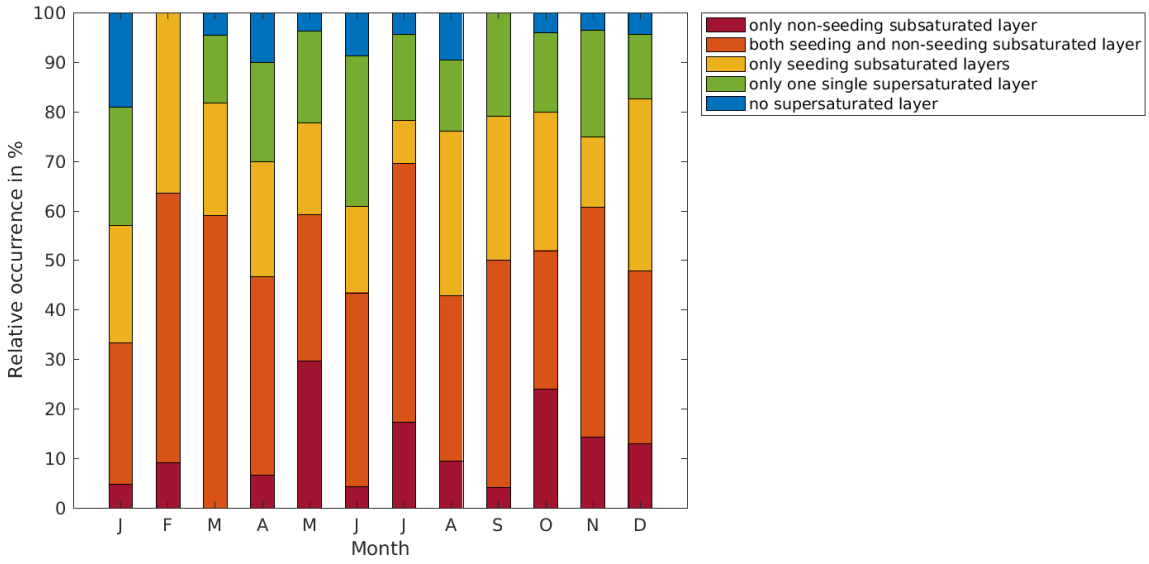

Figure 4.7: Temporal distribution of days between 10 June 2016 - 9 June 2017. Seeding and non-seeding is calculated using an ice crystal of the size $r = 100\,\mu$m.

Here the question arises if the lack of seasonal trend is due to the fact that only the time period of one year is considered. Radiosoundings are available since 1 January 1993 and therefore the detection algorithm is applied to the 24.5 year time period 1 January 1993 - 9 June 2017. Between 2006-2014 some radiosoundings are available with two different kinds of resolution. Here the dataset with the best resolution is chosen. In total 8032 days are evaluated. Since no radar is available, the data screening with respect to subsaturation does only use the minimum thickness threshold of minimum three radiosounding grid points. The resulting temporal evolution is shown in figure 4.8. A seasonal trend is visible regarding the occurrence of 'no supersaturated layers' (blue in figure 4.8), 'only seeding subsaturated layers' (yellow in figure 4.8) and 'both seeding and non-seeding subsaturated layers' (orange in figure 4.8). 'Only non-seeding subsaturated layers'

(red in figure 4.8) and 'only one single subsaturated layer' (green in figure 4.8) does not show any seasonal trend. The occurrences of 'only seeding subsaturated layers' (yellow in figure 4.8) and 'both seeding and non-seeding subsaturated layers' (orange in figure 4.8) are higher in autumn, winter and spring (September-April). A maximum occurs in October. The occurrence of 'no supersaturated layer' (blue in figure 4.8) shows high occurrence between April and August.

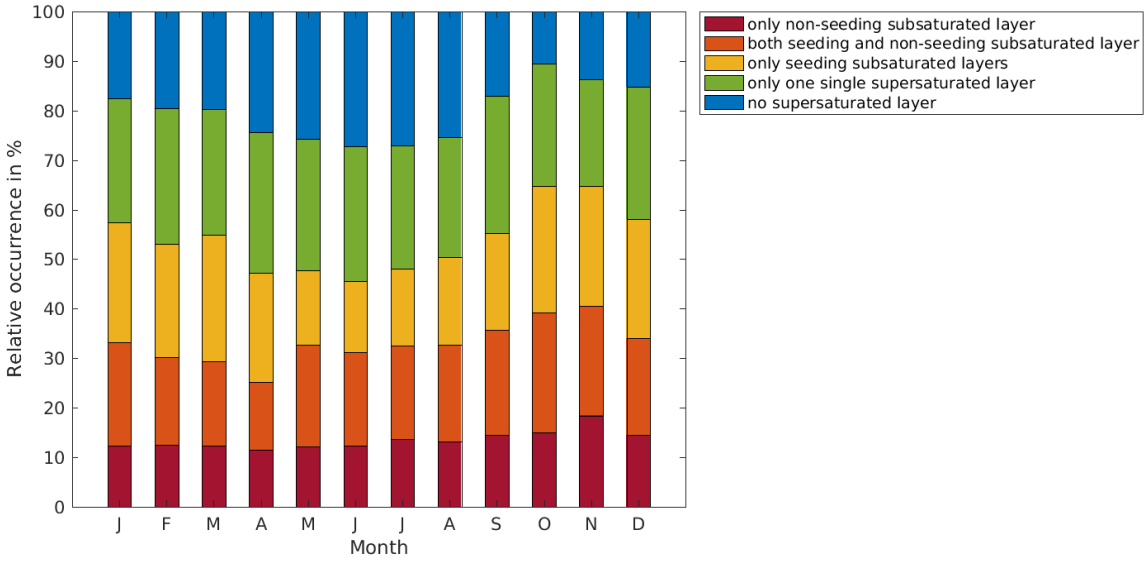

Figure 4.8: Temporal distribution of days between 1 January 1993 - 9 June 2017. Seeding and non-seeding is calculated using an ice crystal of the size $r = 100\,\mu$m.

4.3.3 Discussion

The detection algorithm so far does consider super- and subsaturation of relative humidity with respect to ice. The different assumptions I do are discussed in section 4.5. However, the detection algorithm results in different categories regarding the survival of an ice crystal through subsaturated layers. In the one-year dataset the percentage of seeding 60% (23%+40% in figure 4.6) is slightly higher than the non-seeding percentage 52% (12%+40% in figure 4.6). The ice crystal size used in the calculation has a large impact on the result. In the case of a smaller ice crystal ($r = 50\,\mu$m) the percentage of seeding (54%) is smaller than the percentage of non-seeding (66%) (see figure A.6). However, at this point of this work I preliminarily conclude that seeding is frequently possible.

In the one-year temporal distribution (figure 4.7) there is no seasonal trend between months. The 24.5-year temporal distribution (figure 4.8) shows a weak seasonal trend. The temporal distribution of the categories 'only one single supersaturated layer' (green in figure 4.8), 'only seeding subsaturated layers' (yellow in figure 4.8) and 'both seeding and no-seeding subsaturated layers' (orange in figure 4.8) shows a maximum between autumn and spring (September-April). Treffeisen et al. (2007) derived a monthly mean frequency of occurrence of ice-supersaturated layers, in dependence of height, above Ny-Ålesund. They found a low frequency of occurrence of supersaturation during summer months. In autumn to spring the frequency of occurrence was higher. Their and my 24.5-year temporal distribution results are in good agreement. Here I take it a bit fur-

ther and claim that besides supersaturation also seeding (yellow and red in figure 4.8) as potential microphysical interaction is slightly enhanced during autumn to spring.

It is tempting to combine the derived categories 'only seeding subsaturated layers' (yellow in figure 4.6), 'both seeding and no-seeding subsaturated layers' (orange in figure 4.6) and 'only non-seeding subsaturated layers' (red in figure 4.6) to a classification of multilayer cloud occurrence. Thereby the supersaturated layers above and below the subsaturation would represent the cloud layers. Indeed, besides supersaturation, additionally enough CCN and IN are needed for cloud formation (see section 2.1.2). As a consequence supersaturation does not always imply cloud appearance. Therefore, in the next section 4.4, I name the derived categories 'only seeding subsaturated layers', 'both seeding and no-seeding subsaturated layers' and 'only non-seeding subsaturated layers' as potential multilayer clouds. These potential multilayer clouds are related to cloud observations derived by radar. By that the microphysical cloud interaction is examined in the way that it is related to the actual cloud appearance.

4.4 Adding radar data to the detection algorithm

4.4.1 Methods

I use the Doppler radar data from Ny-Ålesund (see section 4.2) for the one-year time period (10 June 2016 - 9 June 2017). For the rest of the 24.5-year period no radar data is available. For analysing the continuous radar data just at the time of the radiosounding, the start time is chosen 30 minutes before the radiosounding launch and the end time is 30 minutes after the radiosounding reached 10 km height. For the 3 of November 2016 the evaluated time period of the radar data is visualised as black lines in figure 4.3. The heights of the sub- and supersaturated layers, derived by the radiosounding as explained above, are again indicated as red horizontal lines. At some days the radar data does not exist at the time of the radiosounding (e.g. 3 May 2017) such that these days are not considered further. At some days the measured radar signal exists, but seem to have been recorded incorrectly (e.g. 10 October 2017 see figure A.10, and 13 February 2017). The data does not show any change with time for a shorter period, but the information on cloud height is still useful. Therefore, and since sorting out these days would only be done manually, this data is considered further.

The aim of adding radar data to the detection algorithm is to cross-check the potential multilayer clouds with actual cloud occurrence. For each subsaturated layer the 5 lower most height levels ($\sim$ 100 m) are considered. If the layer is thinner than 5 height levels, only the available height levels are included. Due to the data screening always a minimum of 2 height levels is needed ($\sim$ 40 m), else the subsaturated layer is not counted. A measured radar reflectivity factor above the detection limit means that something (e.g. a cloud droplet or an ice crystal) reflected the radar signal back. In that way the selected data is evaluated regarding if more than 50% of the datapoints contain radar reflectivity factor data (coloured in figure 4.3). If so it is sorted as cloud. No radar reflectivity factor data means there is nothing in the air (e.g. no cloud droplet nor ice crystal) that could reflect the radar signal back. In this way, if less than 50% of the datapoints contain radar reflectivity factor data (white in figure 4.3), it is sorted as no cloud. For the evaluation of the supersaturated layer above the subsaturated layer a similar evaluation is done. The lowermost 100 m

of the supersaturated layer are considered. Again, if more than 50% contained radar reflectivity factor data, it is considered as cloud. If less than 50% contained radar reflectivity factor data, it is considered as no cloud. For the supersaturated layer below, it is searched for, starting from top, any layer of 5 height levels ($\sim$ 100 m) containing more than 50% radar reflectivity factor data. Approaching the lower boundary of the supersaturated layer, the evaluated layer height is decreased until only one height level. If no layer contains more than 50% radar reflectivity factor data, it is considered as no cloud.
In the example of the 3 November 2016 (see figure 4.3) the subsaturated layer at 4.26 km (layer 1 in figure 4.3) is sorted as no cloud, since the lower 100 m shows less than 50% of radar reflectivity factor data. The supersaturated layer between 4.26 km and 7.5 km is sorted as cloud, since the lowermost 100 m are dominated by pixels with measured radar reflectivity factor. The supersaturated layer below, between 2.15 km and 3.9 km, is sorted as cloud, since a majority of radar reflectivity factor data is found at about 3.5 m. In the example of the 13 August 2016 (see figure A.3) the subsaturated layer between 1.15 km and 2.45 km (layer 5 in figure A.3) is sorted as no cloud since the lowermost 100 m do show less than 50% radar reflectivity factor data. The supersaturated layer below, between 1.0 km and 1.15 km, is considered as cloud since a majority of 100 m or less height levels contain radar reflectivity factor data. A few cases occur, where a supersaturated layer is counted as no cloud when being considered above a subsaturated layer and the same supersaturated layer is counted as cloud when being considered below a subsaturated layer. An example of this is the 27 October 2016, see figure A.11 and its description in the label. For the potential multilayer cases (one subsaturated and two supersaturated layers) I get seeding or non-seeding information from the radiosounding. In the way of analysing the radar data in each single super- and subsaturated layers I get information about the cloud appearance in each of these layers.

4.4.2 Results

The detection algorithm using the radiosoundings results in different categories (see figure 4.6). Potential multilayer cloud cases occur to the very high percentage 75% (23%+40%+12%, see figure 4.6). Adding radar data to the detection algorithm leads to additional eight subcategories of the potential multilayer cloud cases. These subcategories are:

1. no cloud below, no cloud in between, no cloud above
2. cloud below, no cloud in between, cloud above
3. cloud below, cloud in between, cloud above
4. cloud below, cloud in between, no cloud above
5. no cloud below, no cloud in between, cloud above
6. cloud below, no cloud in between, no cloud above
7. no cloud below, cloud in between, cloud above
8. no cloud below, cloud in between, no cloud above

In the following I only refer to the numbers of these subcategories. In between refers to the subsaturated layer. Below and above refers to the supersaturated layers just next to the subsaturated

layer. The sum of all subcategories equals the sum of all subsaturated layers (and not the sum of all days, since some days have more than one subsaturated layer). The distribution of these different subcategories is divided into non-seeding and seeding cases and presented in figure 4.9 and figure 4.10. For the sizes $r = 50\,\mu$m and $r = 150\,\mu$m the plots are shown in the figures A.12, A.13, A.14 and A.15.

Multilayer clouds are only expected in some of the gained subcategories. The subcategory 2. (cloud below, no cloud in between, cloud above) is very likely to be a multilayer cloud. This subcategory is coloured pink (see figure 4.9). The subcategory 3. (cloud below, cloud in between, cloud above) does not appear as a multilayer cloud if only using radar. Though, the layering indicated by the radiosounding could potentially be verified by other instruments (lidar). In this way this category is coloured light green (see figure 4.9 and 4.10). The subcategory 1. (no cloud below, no cloud in between, no cloud above) is very unlikely to be a multilayer cloud. Therefore this subcategory is coloured grey. Also all other categories unlikely to be multilayer clouds are coloured grey (see figure 4.9 and 4.10).

For the non-seeding cases (r=100 μm, see figure 4.9) the subcategory 7. and the subcategory 8. do not occur (0%). Further in the non-seeding cases the subcategory 1. is strongly represented (32% grey in figure 4.9). The subcategory 2. is represented in 14% of the cases (pink in figure 4.9) and the subcategory 3. is represented in 7% of the cases (light green in figure 4.9). For the seeding cases (r=100 μm, see figure 4.10) the subcategory 2. and the subcategory 8. do not occur (0%). Further, in the seeding cases the subcategory 1. is strongly represented (44% grey in figure 4.10). The subcategory 3. is represented in 37% of the cases (light green in figure 4.10).

It is noticeable that in both the non-seeding (figure 4.9) and seeding cases (figure 4.10) the subcategory 1. (no cloud below, no cloud in between, no cloud above) occurs frequently (32% and 44%). This indicates that the potential cloud detection by only using the radisounding and thereby only supersaturation as cloud criteria leads to a large amount of erroneous detection. Regarding the question if microphysical interaction between two multilayer clouds is possible, it is of great interest that the subcategory 2. (cloud below, no cloud in between and cloud above) does not occur in the seeding case (figure 4.10). In other words, it is found that two separate cloud layers with clear visible interstice in between (seen by radar) do not interact by seeding.

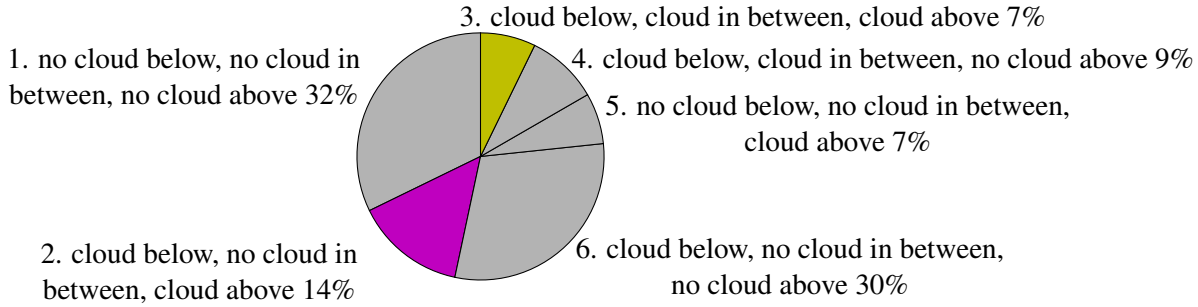

Figure 4.9: Non-seeding: Subcategories of all non-seeding subsaturated layers. In between refers to the subsaturated layer. Below and above refers to the supersaturated layers just next to the subsaturated layer. 100% equals all non-seeding subsaturated layers. Non-seeding is calculated using an ice crystal of the size $r = 100\,\mu$m.

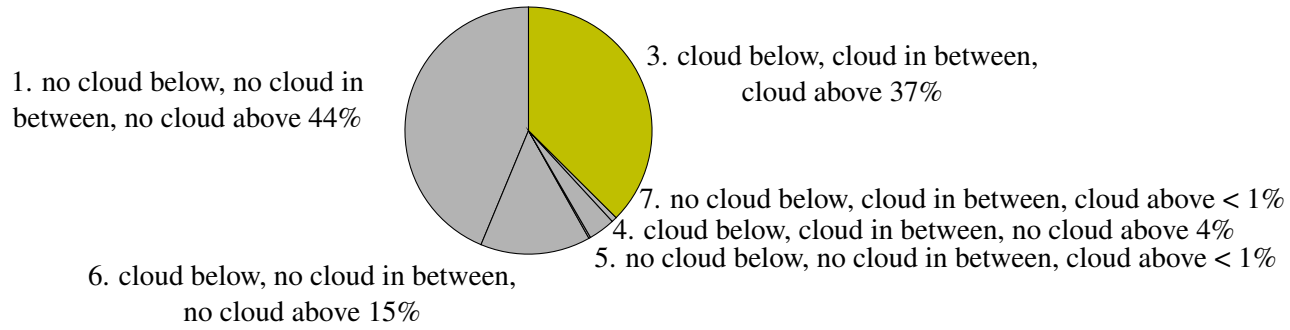

Figure 4.10: Seeding: Subcategories of all seeding subsaturated layers. In between refers to the subsaturated layer. Below and above refers to the supersaturated layers just next to the subsaturated layer. 100% equals all seeding subsaturated layers. Seeding is calculated using an ice crystal of the size $r = 100\,\mu$m.

A smaller ice crystal size (see figure A.12) shows in the non-seeding case a slight reduction of the subcategory 2. (9% pink in figure A.12) and increase in the subcategory 3. (20% light green in figure A.12). A greater ice crystal size shows in the non-seeding case the opposite behaviour, a increase in subcategory 2. (17% pink in figure A.14) and a decrease in subcategory 3. (3% light green in figure A.14). For the seeding category no big changes occur for different ice crystal sizes (see figure A.13, 4.9 and A.15). Interestingly, for the ice crystal size $r = 150\,\mu$m in the seeding case the subcategory 2. (cloud below, no cloud in between, cloud above, 1% pink in figure A.15) exists. This means that if I would have an ice crystal of $r = 150\,\mu$m, then this ice crystal could survive a subsaturated layer, in which there is no measured radar cloud signal. This was not the case for the ice crystal size $r = 100\,\mu$m. The change in ice crystal size does not lead to a redistribution between the subcategories, but leads to a redistribution between the seeding and non-seeding category. This is because a e.g. smaller ice crystal would less often survive the subsaturated layer and then count as non-seeding case instead of seeding case. In section 4.3.2 I found already that this redistribution between the seeding and non-seeding category is large. I now find that this large redistribution has only little impact on redistribution among the different subcategories. In other words, even if changing the total number of considered seeding subsaturated layers, the distribution among the different subcategories remains fairly constant.

Including only the selected subcategories 2. (pink) and 3. (light green) is the last step of the classification and leads to an upgraded distribution of cloud layering. This is presented in figure 4.11. The category 'no cloud by radiosounding' (6%, dark blue in figure 4.11) means that there is no supersaturated layer in the radiosounding. The category 'single layer clouds by radiosounding' (18%, green in figure 4.11) means, that only a single supersaturated layer was detected by the radiosounding. Neither of these two categories were analysed further by radar. The category 'multilayer cloud by radiosounding, but no cloud by radar' (14% light blue in figure 4.11) means, that a combination of supersaturation, subsaturation, supersaturation is detected by the radiosounding, but when applying the radar algorithm it results in the subcategory no cloud below, no cloud in between, no cloud above. In other words, even if there are super- and subsaturated layers, there is no cloud in the radar image. The category 'multilayer cloud by radiosounding, but single layer cloud by radar' (24% turquoise in figure 4.11) is used for the cases, where the radiosounding detects a potential multilayer case, but the radar shows a category, that does not confirm the mul-

tilayer assumption (indicated by grey in figure 4.9 and figure 4.10). In other words, even if there are super- and subsaturated layers, there is not a multilayer cloud but a single layer cloud in the radar image. The categories 'only seeding multilayer clouds' (25%, yellow in figure 4.11), 'both seeding and non-seeding multilayer clouds' (6%, orange in figure 4.11) and 'only non-seeding multilayer clouds' (6%, red in figure 4.11) are all multilayer cases confirmed by both radiosounding and radar. Only seeding means, that during that day all subsaturated layers are moist enough for potential survival of an ice crystal. Further, these clouds appear as single layer clouds in the radar. Only non-seeding means that during that day all subsaturated layers are too dry for potential survival of an ice crystal. Both seeding and non-seeding means that during that day some subsaturated layers are moist enough for potential survival of an ice crystal and some other subsaturated layers are too dry for potential survival of an ice crystal. Seeding occurs more often (31% = 25% yellow + 6% orange) than non-seeding (12% = 6% red + 6% orange). In total there are 37% multilayer cloud cases.

Again, for the sizes $r = 50\,\mu$m and $r = 150\,\mu$m the plots are shown in the figures A.16, A.17, A.18 and A.19. Multilayer cloud occurrence (sum of red, orange and yellow in each figure A.16, 4.11 and A.18) is in all cases 37%. This is due to the fact that changing the ice crystal size only causes a redistribution among the three categories 'only seeding', 'only non-seeding' and 'both seeding and non-seeding'. A bigger ice crystal leads to more 'only seeding' cases (yellow in figure A.18) and a smaller ice crystal leads to less 'only seeding' cases (yellow in figure A.16). The increase from $r = 100\,\mu$m to $r = 150\,\mu$m gives a small increase in the category 'only seeding' from 25% to 29%. In contrast, a decrease in size of the same magnitude (from $r = 100\,\mu$m to $r = 50\,\mu$m) leads to a larger reduction in occurrence (25% to 13%). A similar change does also the category 'both seeding and non-seeding' show (4% for $r = 150\,\mu$m, 6% for $r = 100\,\mu$m, 11% for $r = 50\,\mu$m). This might be explained by an uneven subsaturated layer thickness distribution, but I do not check this. However, this means that varying the ice crystal size between $r = 50\,\mu$m and $100\,\mu$m has major importance for the classification than varying the ice crystal size between $r = 100\,\mu$m and $150\,\mu$m.

The temporal distribution is presented in figure 4.12. Multilayer clouds show highest values in July- November and February - March (red, orange, yellow in figure 4.12). They occur less often in April - June and December - January. There is no clear seasonal trend among the three multilayer cloud categories ('only seeding', 'only non-seeding', 'both seeding and non-seeding' in figure 4.12). This does also not change if varying the ice crystal size (see figure A.17 and A.19). Cloud coverage in general does also not show any seasonal trend (red, orange, yellow, turquoise and green in figure 4.12). As already seen in section 4.3.2, the one-year temporal distribution does only give limited information in contrast to the 24.5-year temporal distribution. Applying the detection algorithm to a longer time period is not possible since the radar is operated in Ny-Ålesund only since 10 June 2016. In this way, the one-year temporal distribution of multilayer cloud occurrence should be treated carefully.

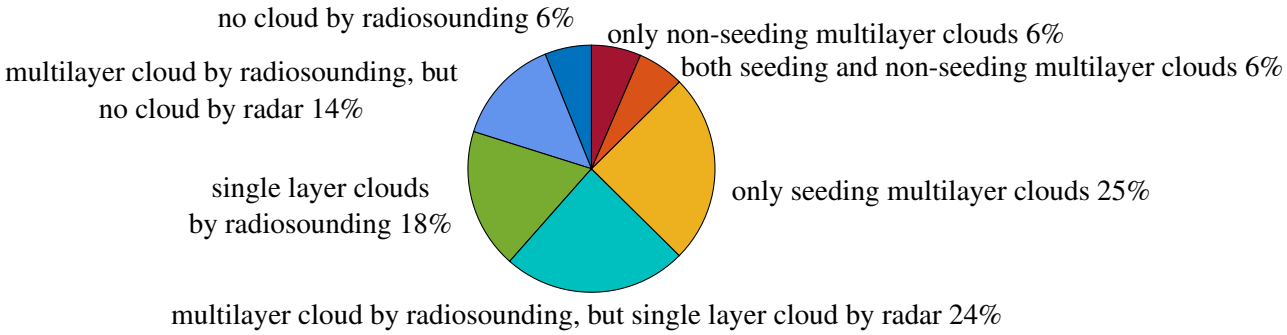

Figure 4.11: Cloud occurrence derived from using both radiosounding and radar for detection. 100% equals 278 days between 10 June 2016 - 9 June 2017. Seeding and non-seeding is calculated using an ice crystal of the size $r = 100\,\mu$m.

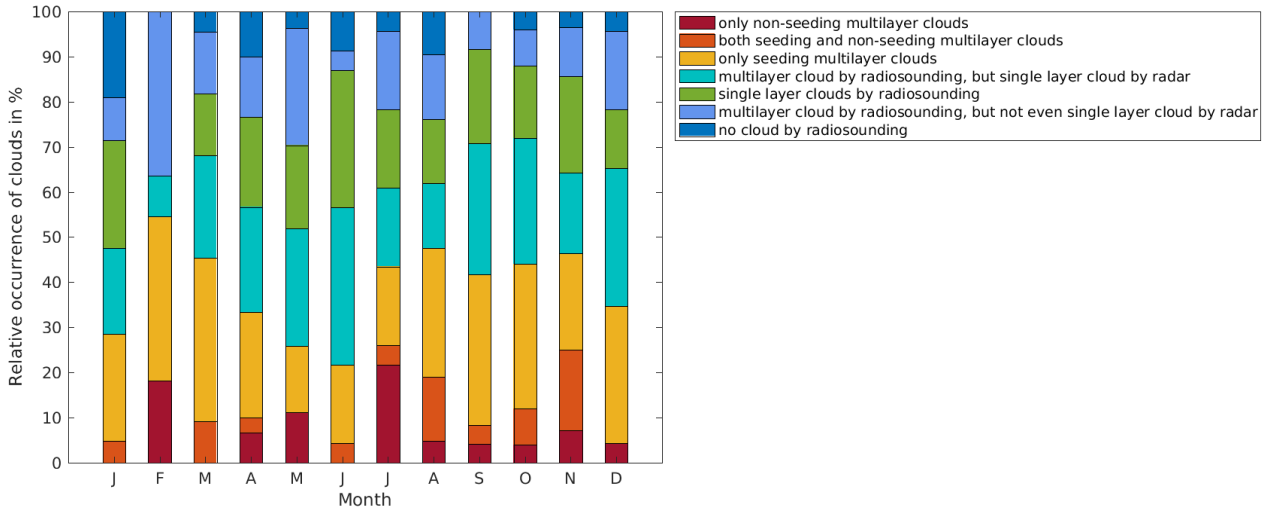

Figure 4.12: Temporal distribution of cloud occurrence using both radiosounding and radar. Seeding and non-seeding is calculated using an ice crystal of the size $r = 100\,\mu$m.

4.5 Limitations, assumptions and evaluation of the classification

4.5.1 Limitations and assumptions

Ny-Ålesund has the great advantage that since radiosounding and radar are at the same place a comparison is possible. In the following section I want to discuss why the results of radiosoundings and radar can differ, which assumptions were used for the classification algorithm and how it was verified. The goal is to give a final answer to the question if microphysical interaction is possible and how often it occurs in multilayer clouds. For a short overview the following uncertainties are discussed further: Uncertainties in the radiosounding measurements, threshold for super- and subsaturation, minimum thickness limits for the considered super- and subsaturated layers, variations in radiosounding and radar measurement locations, the averaging in the radar measurements, the possibility of multilayer clouds divided by more than one subsaturated layer, the chosen ice crystal size, and last but not least the correct interpretation of the radar signal.

Maximum cloud height is limited by the tropopause height. Determining this for each individual day would be too elaborate and for comparison a constant height is more suitable. Treffeisen et al. (2007) analysed all heights until 11 km. At the radar images no cloud occurs above 10 km. In this way the maximum considered height is set to 10 km.

Due to various types of sensors the raw data of the radiosoundings has inhomogeneities. Before 2002 the sensors did not have an integrated heating system to prevent sensor icing. If the sensors acquired ice coating they would continue measuring ice saturation even in subsaturated environment. After 2002 a heated sensor system reduced this error. Secondly, before 2006 the humidity sensors had a prolonged response time at lower temperatures. As a third error, since the sensors were not shielded from solar radiation, a daytime radiation dry bias occurred. To account for these errors, an algorithm for homogenization has been applied to all datasets (Maturilli and Kayser, 2017; Treffeisen et al., 2007; Miloshevich et al., 2001, 2004). From 2006 on the GRUAN dataset used a new sensor and the homogenization algorithm became less important. Additionally a ground calibration inside a humidity chamber of 100 % relative humidity prior to each launch resulted in even more improvement. Since April 2017 the dataset was conducted with an newer type of sensor. Also here a correction algorithm has been applied, comparable to that of GRUAN. All in all the measurements of relative humidity become less reliable at temperatures lower than $-40\,^{\circ}\mathrm{C}$. In this way the applied corrections mostly affect high levels and cold temperatures.

Since the radiosounding measurements contain errors, especially at low temperatures, a threshold for dividing between super- and subsaturated layers was discussed by Treffeisen et al. (2007). For using other thresholds than $RH_i = 100\%$ they found the frequency of supersaturated layers to change, but not the temporal evolution. In the same way I choose $RH_i = 100\%$, as the most dominant errors already were corrected (Maturilli and Kayser, 2017; Treffeisen et al., 2007; Miloshevich et al., 2001, 2004) and for the remaining uncertainties I assume that they are homogeneously distributed. The comparison of radiosounding and radar shows that the $RH_i = 100\%$ thresholds works for many cases (16 July 2016 at 1.7 km in figure A.1, 27 July 2016 at 1.1 km in figure A.2, 13 August 2016 at 2.9 km in figure A.3). But in other situations the threshold is not that good. At the 17 August 2016 (see figure A.20) cloud top at 1.7 km is too low compared to the radar image.

This potential error has then an effect on the combined classification. Inside the subsaturated layer the radar signal of only the lowest height levels is evaluated. In the case of the 17 August 2016 the subsaturated layer between 1.7 km and 3.5 km is therefore classified as cloud containing.
The classification does not consider subsaturation between two supersaturation regarding water layers (16 July 2016 between 0.5 km and 1.5 km height in figure A.1). This was done, since in this work the main interest is potential ice crystal seeding. Though, if applying the classification to detect non-seeding multilayer clouds in warmer environment than the Arctic, this should be modified.
Deciding a suitable minimum thickness limit for the super- and subsaturated layers turned out to be challenging. For the supersaturated layers I use a minimum of 100 m. In general a too big minimum thickness threshold means leaving out cloud layers that are of interest. The supersaturated layer at 16 July 2016 between 4.5 km and 4.8 km height is only 300 m thick (see figure A.1a)). Still it is of importance as a visible cloud signal in the radar image (see figure A.1b)). There is a similar case on the 30 June 2016 with 250 m (see figure A.21). Using a too small minimum thickness limit means including too many not relevant layers. A too thin supersaturated layer would most likely not result in a cloud signal by the radar (in 3.3 km on 16 July 2016 in figure A.1). Further, since the classification only considers layers next to a subsaturated layer, the case where an ice crystal could fall through these thin (not relevant) supersaturated layers and thereby reach additional layers on its way down is not considered. Therefore, including too thin supersaturated layers, as in the case of 3.3 km height on 16 July 2016, would distort the multilayer result and should be avoided. Treffeisen et al. (2007) used a minimum threshold of 200 m for the supersaturated layers. This threshold was mainly chosen due to the resolution of the radiosoundings. For the Antarctic, Nygård et al. (2013) found humidity inversions to be less than 200 m deep. Summarizing, some kind of threshold for the supersaturated layers has to be chosen. To ensure not to miss out too many cloud layers, the threshold of 100 m is chosen.
As a minimum distance between two clouds Intrieri et al. (2002b) used 90 m. Intrieri et al. (2002b) defined multilayer clouds as two separate clouds with clear visible interstice in between (see section 2.2.1). Verlinde et al. (2007) defined multilayer clouds as a variable lidar signal inside a more or less continuous radar signal. They found the layers to vary between 50 m to 300 m in depth (see section 2.2.2). In order to test both kinds of multilayer clouds for the possibility of seeding, the original idea was to include all subsaturated layers regardless how thin. The thinner the subsaturated layer is, the more ice crystals would survive if falling through. In this way even the thinnest subsaturated layers have to be accounted for. Though, considering all layers would also increase the number of non relevant layers, e.g. when there is no measured cloud above and below. Both the 27 July 2016 above 9.0 km (see figure A.2) and the 13 August 2016 above 8.8 km (see figure A.3) illustrate this. This consideration leads to a data screening, where single radar points or, due to a finer resolution, double radiosounding points of subsaturation are excluded. As a result the minimum considered height for subsaturated layers becomes 21.7 m. It appears to me that a minimum thickness threshold between 20-25 m is acceptable. Therefore I suggest to modify the classification to a more uniform minimum thickness threshold (considering height instead of radiosounding/radar measurement points) of this magnitude.
For the combination of radiosounding and radar data, I have to keep in mind that wind is always present and during approximately 1 h of ascend the radiosounding has drifted away to some extend.

Secondly the radiosounding did only measure once at each height and the radar measurements have to be averaged. The choice of averaging is done with regard to potential ice crystal precipitation. In the supersaturated layer above only the lowest part is of interest, since from here the ice crystal might originate. For the subsaturated layer in the mid I also only evaluate the lowest part. This is due to the question if the ice crystal has survived so far. In the supersaturated layer below any radar signal at any height is of interest. As soon as the ice crystal reaches this supersaturated layer it has survived and does not decrease in size any more. A cloud lower down can therefore still be influenced by this ice crystal. It should be kept in mind, that the different ways of averaging in the supersaturated layers could lead to different results for the same layer (regarding two different subsaturated layers) (see figure A.11).

The classification using only radiosoundings leads to categories regarding super- and subsaturated layers. The combined classification using both radiosounding and radar leads to additional subcategories. The subcategory 1. (no cloud below, no cloud in between, no cloud above) occurs in all cases to a high percentage. Even if supersaturation is reached, the lack of CCN and IN can prevent cloud condensation. This is in good agreement with Gierens and Spichtinger (2000); Spichtinger et al. (2003) who investigated the global occurrence of this phenomena in detail. Supersaturation but cloud formation just afterwards or cloud dissipation just before but still supersaturation (at 6 km height on 22 October 2016, figure A.22) are also good reasons why radiosounding and radar did not always match. From the rest of subcategories only the two most obvious subcategories 2. (cloud below, no cloud in between, cloud above) and 3. (cloud below, cloud in between, cloud above) are counted as multilayer cloud. The subcategory 3. is also in the non-seeding cases counted as multilayer cloud. This is questionable since neither a visible multilayer cloud in the radar nor seeding can explain why this should be a multilayer cloud. Though, some of these cases are still multilayer clouds. An example to this is the subsaturated layer 3 on the 28 April 2017 (between 0.9 km and 3.2 km height in figure A.23). In this way, if taking the 3. subcategory for the non-seeding cases away, then some wrong sorted multilayer clouds have to be accepted.

Days showing multilayer clouds by radar are also found in some of the other categories. The most striking error is then, that the classification only considers layers just next to each other. Both on the 17 August 2016 and on the 30 June 2016 (see figure A.20 and A.21) non seeding multilayer clouds are visible in the radar image. But since in both cases an additional supersaturated layer, but with no cloud signal in the radar, disrupts the detection, the case is not categorized correctly. One improvement could be to search for any kind of cloud layer below a subsaturated layer. A second way of improvement could be to test the opposite way of detection: First identifying cloud boundaries by radar and secondly identifying super- and subsaturated layers inside the cloud boundaries by radiosounding. Though, since super- and subsaturated layers were frequently discussed (Treffeisen et al., 2007; Maturilli and Kayser, 2017; Nygård et al., 2014), my way leads to interesting answers about how these different layers behave regarding cloud formation.

A correct assumption for the ice crystal size is crucial for the sublimation calculation and was discussed in section 3.2, but no final answer could be found. In that way the occurrence of the different subcategories in the combined classification were evaluated for the different sizes $r = 50\,\mu$m, $100\,\mu$m and $150\,\mu$m (see figure A.12, A.13, 4.9, 4.10, A.14 and A.15). For the correct size the following is expected: In the non-seeding cases a high percentage of the subcategory 2. (cloud below, no cloud in between, cloud above) and a low percentage in the subcategory 3. (cloud be-

low, cloud in between, cloud above). Additionally, in the seeding cases a low percentage of the subcategory 2. (cloud below, no cloud in between, cloud above) and a high percentage in the subcategory 3. (cloud below, cloud in between, cloud above) is expected. For the ice crystal of $r = 50\,\mu$m the subcategory 2. in the non-seeding case (20%) is bigger than the subcategory 3. (9%) (see figure A.12). For the ice crystal of $r = 150\,\mu$m the subcategory 2. occurs in the seeding case (1%) (see figure A.15), where as it does not for the other two sizes. These two results indicate that $r = 100\,\mu$m is the best choice for an average ice crystal size. Therefore I have the main focus on $r = 100\,\mu$m.

4.5.2 Evaluation with Cloudnet

Regarding the question if multilayer clouds do interact microphysically by seeding, I can answer it by referring to the non-occurrence and occurrence of two subcategories in the combined classification. The subcategory 2. (cloud below, no cloud in between, cloud above) does not occur in the seeding cases (see figure 4.10). Instead I count the subcategory 3. (cloud below, cloud in mid, cloud above, light green in figure 4.10) as seeding multilayer cloud. This leads to the question if the radar measurements can be interpreted in more detail regarding if it actually is a cloud or precipitating ice crystals that lead to the measured radar reflectivity factor inside the subsaturated layer. As an example I use the subsaturated layers 2, 3 and 4 on the 3 November 2016 (see figure 4.4). These three subsaturated layers are seeding cases and belong to the subcategory 3. (cloud below, cloud in between, cloud above). In order to interpret the doppler velocity and doppler spectral width (see figure 4.2) some kind of horizontal layering structure in the supersaturated layers and some kind of vertical fall strikes from precipitating ice crystals in the subsaturated layers is expected. No clear structures can be identified in theses two variables and therefore I do not consider these variables further.

In order to gain more microphysical information from cloud measurements, Cloudnet (Cloudnet; Illingworth et al., 2007) was developed. Cloudnet combines a doppler cloud radar, a lidar and a microwave radiometer (measures radiation in the microwave wavelength). In figure 4.13 the cloudnet classifiation for Ny-Ålesund on the 3 November 2016 is shown (data source see acknowledgements in section A.12). Ice is classified when the radar doppler velocity indicates falling particles and the dew-point temperature is below 0 °C (Bühl et al., 2016) (yellow in figure 4.13). In the case of Ny- Ålesund, temperatures for Cloudnet are taken from the ICON (Icosahedral Nonhydrostatic) global model. A cloud is classified as mixed-phase (green in figure 4.13), if additionally to the detection of ice, liquid is detected by lidar. Liquid droplets result in high lidar backscatter and near-zero lidar depolarisation (Luke et al., 2010). Unfortunately a micropulse-lidar providing lidar backscatter and lidar depolarisation had existed in Ny-Ålesund, but this ended at 16 June 2016 (Lidar, 2017). Thereby it was not available during the time of interest (10 June 2016 - 9 June 2017). Instead a ceilometer (detecting cloud base) was used for the Cloudnet classification in Ny-Ålesund. A ceilometer measures only the lowest cloud base and thereby its vertical range is limited. The reduced vertical coverage of the lidar (=ceilometer) in Ny-Ålesund on the 3 November 2016 is shown in figure 4.14 (green=radar and lidar, blue= only radar). Since the lidar/ceilometer did not provide the needed information in the total vertical range, the cloud phase distinction of Cloudnet for the 3 November 2016 in Ny-Ålesund is strongly dependent on

temperature. In the temperature range between 0 °C and −38 °C the clouds are almost entirely classified as ice (yellow in figure 4.13). Bühl et al. (2016) presents a further developed Cloudnet classification, which is less dependent on model temperature. Applying this to the Ny-Ålesund case could potentially increase the knowledge on microphysics of the measured clouds. But so far is remains an open question whether I have clouds or precipitating ice in the subsaturated layers 2, 3 and 4 on the 3 November 2016.

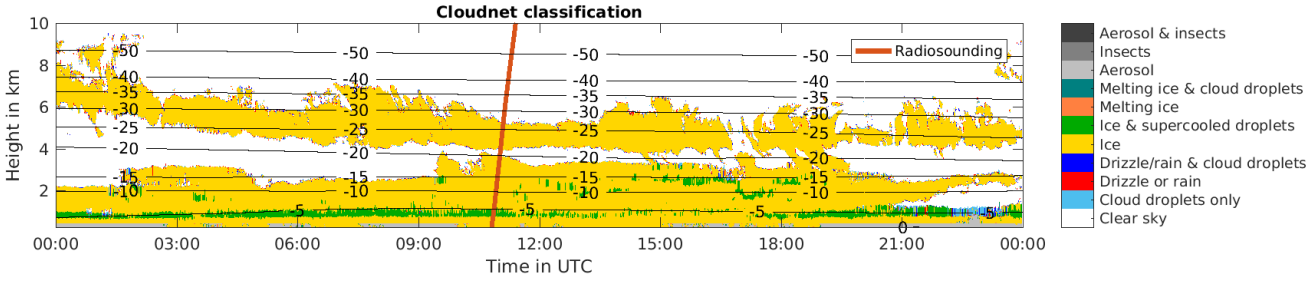

Figure 4.13: Cloudnet classification at 3 November 2016 in Ny-Ålesund. Mainly ice (yellow) and ice & supercooled droplets (green) are relevant categories. Black lines show the temperature isolines based on the ICON global model. The red line indicates the radiosounding used on that day. Data source: see Cloudnet and acknowledgements in section A.12.

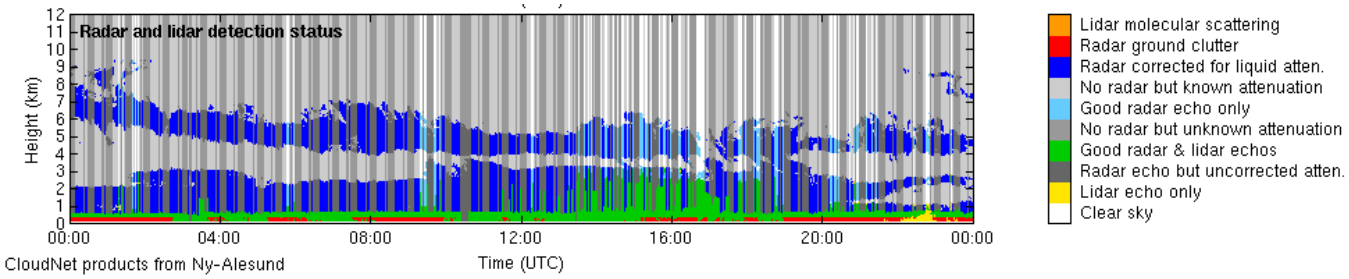

Figure 4.14: Radar and lidar (ceilometer) detection status at 3 November 2016 in Ny-Ålesund. Mainly only radar (blue and dark grey) was used for the Cloudnet classification shown in figure 4.13. Radar and lidar together occurred only in the lowest levels (green). Data source: see Cloudnet and acknowledgements in section A.12.

4.5.3 Visual evaluation

As the combined classification has many uncertainties, an evaluation is needed to investigate its reliability. The easiest way for doing so, is a visual evaluation of the radar reflectivity factor data. For the visual classifiation the same time period as for the one-year combined classification is used. Out from the continuous radar signal only one hour at the time equal to the radisoundings (12 UTC) is considered. The results are shown in figure 4.15 and its temporal distribution is shown in A.24. The radar measurements are evaluated regarding no cloud (22%), single layer (57%) and multilayer clouds (22%) (see figure 4.15). Regarding the temporal distribution (see figure A.24), a slight reduction of multilayer clouds occurs in January, March, April and December. But no clear seasonal trend is visible. No distinction between seeding and non seeding can be done. Additionally no evaluation of in-cloud layers can be done.

The radiosounding detection method gives categories with seeding and non-seeding subsaturated layers in 75% of the investigated cased (23% yellow + 40% orange + 12% red in figure 4.6). The

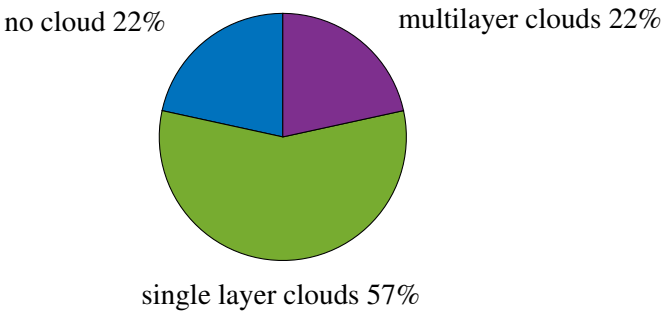

Figure 4.15: Relative distribution of days by visual detection. 100% equals 278 days between 10 June 2016 - 9 June 2017.

comparison of the visual detection (see figure 4.15) with the detection only using radiosoundings (see figure 4.6) clarifies a discrepancy. Multiple supersaturated layers do not necessarily entail multiple cloud layers. Instead these multiple super- and subsaturated layers can be embedded in a continuous cloud radar signal (in-cloud layers). Additionally multiple super- and subsaturated layers can also occur where there is no cloud formation at all.

The comparison of the visual detection (see figure 4.15) to the detection using both radiosounding and radar (see figure 4.11) reveals much better agreement. In the combined classification 6%+14%=20% belongs to the no cloud category. The visual detection gives 22%. The combined classification gives 18%+24%=46% for the single layer cloud category. The visual detection gives 57%. For the multilayer clouds the visual detection gives 22%. The combined classification gives 6%+6%=12% for the multilayer clouds. In the combined classification additionally the category only seeding multilayer clouds is 25%. These seeding cases can either be due to precipitating ice crystals or due to smaller non precipitating ice crystals and cloud droplets. A further distinction without more measurement techniques (lidar) appears difficult. For the case of the 3 November 2017 I considered this by presenting the method of Cloudnet. As also Cloudnet did not give any clear information whether these seeding layers are in-cloud layers or not, the category only seeding multilayer clouds should be counted as both multilayer clouds and single layer clouds.

In summary, even if the category only seeding multilayer clouds remains as uncertainty, the comparison of the visual detection with the combined classification shows good agreement. According to the combined classification, multilayer clouds occur between 12% (=6%+6%) and 37% (=6%+6%+25%). To not only compare the percentages in the same category of visible and combined classification, but also to evaluate if specific days actually belong to the same category a skill score table could be developed. In this way, regarding seeding and non-seeding multilayer cloud layers, the amount of hits (both visible and combined classification agree) and fails (visible and combined classification disagree) could be evaluated in even more detail. Hopefully, thereby also an answer to the correct sorting of the subcategory 3. (cloud below, cloud in between, cloud above) for the non-seeding cases could be found.

4.5.4 Discussion

The combined classification is developed using both ground based radiosoundings and radar reflectivity factor measurements. For the combined classification one main improvement would be

to make the minimum considered subsaturated layer height more uniform. Secondly, an extension to search in multiple layers for non-seeding multilayer clouds should also be considered. Nevertheless, some uncertainties remain. For the seeding calculation I set, since I assume this to be most likely, the ice crystal size to $r = 100\,\mu$m. Further, the wind transports the radiosounding, which makes an exact accordance between radiosounding and radar limited. Besides supersaturation also enough CCN, IN and their activation is needed to form clouds. Since for IN activation, in contrast to CCN activation, only low supersaturations are needed, cloud ice activation has probably the major influence on the disagreement between radiosounding and radar. The evaluation of the combined classification is done using a very simple visual detection method. To evaluate the hits and fails between the visible and combined classification even more a skill-score could be applied. However, the combined classification resulted in a classification of 12-37% multilayer clouds over Ny-Ålesund during a one-year time period. This is in very good agreement to a very simple visual detection of 22% multilayer clouds. Also satellite measurements show similar results. For the area Barents Sea, to which Ny- Ålesund belongs to, multilayer clouds occurred on an annual average in 25% (Liu et al., 2012). Nevertheless, the satellites did only include layers of a minimum thickness of 960 m (Liu et al., 2012). Many both in-cloud and visible separated layers were much thinner. In this way the satellite is assumed to underestimate the multilayer cloud amount.

In the combined classification of using both radiosoundings and radar the seasonal cycle is almost not visible, except of a slight increase in autumn and early spring. In order to question the reliability of this weak seasonal cycle three arguments are considered. Firstly, in the satellite data a seasonal cycle was reported (Liu et al., 2012). Though, for the area of Ny-Ålesund the seasonal cycle was almost not visible. Secondly , in the visible detection I do not find any seasonal cycle. Thirdly, when only using radiosounding there is no seasonal cycle in the one-year period, but in the 24.5-year period. The latter is in agreement with Treffeisen et al. (2007) and this indicates that the time period in the combined classification is too short. For these three reasons the significance of the weak seasonal cycle in the one-year combined classification should be questioned.

Regarding the question about microphysical interaction of multilayer clouds, I summarize it with that seeding is potentially possible in 31% of the investigated cases. Seeding occurs only if there is a radar signal in the subsaturated layer. The latter is in agreements with Verlinde et al. (2007) and Khvorostyanov et al. (2001). Both related the seeder-feeder-mechanism to measured radar signals. In the combined classification I use a minimum considered layer height of 100 m for the supersaturation and approximately 20 m for the subsaturated layers. In this way, much thinner layers than when using satellite data (minimum 960 m in Liu et al. (2012)) are included. Thereby I am able to gain great insights about how often microphysical interaction is possible and how these super- and subsaturated layers correspond to cloud layers visible in radar measurements.

5 The modelling setup in COSMO

The detection algorithm resulted in 12% non-seeding multilayer cloud occurrence. If not microphysically, then these non-seeding multilayer clouds can still interact through radiation. The possible effects of this radiative interaction was shortly presented in figure 2.8. To verify those assumptions (grey labels) made in figure 2.8, in the following the radiative multilayer cloud interactions are investigated. In order to show the effects two clouds have on each other the weather model COSMO (Consortium for Small-Scale Modelling) is used. LES (large-eddy-simulations) modelling is applied and for this data from the ASCOS (Arctic Summer Cloud Ocean Study) field campaign is used as initial input. The modelling setup and the initial input is presented in this section 5 and in section 6 the model results are shown.

5.1 The COSMO model

The COSMO model was developed by the German Meteorological service DWD and was in use since 1999 (Doms and Baldauf, 2015; Doms et al., 2011; Schättler et al., 2016). COSMO is a nonhydrostatic limited-area atmospheric prediction model. It is based on the Euler equations describing compressible flow in a moist atmosphere. The geographical coordinate system is formulated as rotated spherical coordinates. The pole is tilted in the way that the equator runs though the model domain. Thereby convergence of the meridians is minimized and the grid-cells become quadratic. The grid structure is an Arakawa C-grid with a Lorenz vertical grid staggering. In the Arakawa C-grid scalars are calculated at grid-cells and the wind velocities are calculated in the mid-point between. In the vertical, on a Lorenz-grid most variables are defined in the middle of each layer (main level) and only vertical velocities and turbulent vertical fluxes are on half levels. The vertical coordinates are height-based Gal-Chen coordinates. Normal height-based coordinates would give high computational costs for calculating the lower boundary conditions when including orography. The transformation into Gal-Chen coordinates circumvents this problem by being terrain-following. Further the Gal-Chen coordinates are hybrid, which means that they become flat at a given height above the orography. Time integration is a third-order Runge-Kutta scheme.

Since many meteorological processes are on much smaller scales than the grid-scale of the model, these small scale processes are calculated separately. Their calculation schemes are thereby usually based on parameterizations. Parameterizations are empirical descriptions of the effects on the large-scale processes given by the small scale processes. The three schemes most relevant for my study are the cloud microphysics, the radiation and the surface interactions through sea ice. These three schemes are shortly described in the following (Doms et al., 2011; Schättler et al., 2016).

Two-moment microphysics scheme

Cloud microphysics deal with the representation of precipitation and cloud formation. Thereby the focus is on the processes at the 1×10^{-6} m=μm-scale. In order to model clouds and precipitation the two-moment microphysics scheme of Seifert and Beheng (2006) is used. The two-moment scheme is based on the idea of using power moments for easily deriving both the number density (zeroth moment $M^0 \equiv QNC$) and mass density (first moment $M^1 \equiv LWC$) for water etc.. For liquid (l) this is

$$M_l^0 = \int_0^\infty f_l(x)\, dx \equiv QNC \tag{5.1}$$

$$M_l^1 = \int_0^\infty x f_l(x)\, dx \equiv LWC. \tag{5.2}$$

x refers to the mass and $f_l(x)$ to the number density size distribution function. In a similar way the number densities and masses of six hydrometeor types (cloud droplets, cloud ice, raindrops, snow, graupel and hail) are calculated separately. In order to distinguish small cloud droplets from precipitating rain a separation was done at a radius of r =40 μm. In the case of Arctic clouds, the amount of graupel and hail is negligible small. For the cloud formation processes I prescribe the number concentration (see section 6). Provided that there is supersaturation, the model calculates liquid particle growth due to condensation and autoconversion (particles collide and merge, see also section 2.1.2). Rain droplets are formed through autoconversion, accretion (one raindrop collects further cloud droplets) and also through the melting of ice. Evaporation, precipitation and particle break-up processes are considered as sinks.

For the growth of ice crystals and snow nucleation, growth by water vapour deposition and autoconversion are considered (see section 2.1.2). Also riming (ice and supercooled water collide, see section 2.1.2) and freezing of raindrops is included. Melting, precipitation and break-up are considered as sinks. The ice nucleation parameterization used is based on Fletcher (1962). He suggested an empirical formula, where the amount of activated ice nuclei N_I is only dependent on the air temperature T. Huffman and Vali (1973) represented an adjustment were they included the dependence of the ice activation on supersaturation

$$N_I = N_0 \cdot \left(\frac{S}{S_0}\right)^{4.5} \exp\left(-0.6 \cdot (\max(T, T_m) - 273.15)\right) \qquad \text{with } N_0 = 1 \times 10^{-2}\,\mathrm{m}^{-3}. \tag{5.3}$$

N_0 is the initial ice nuclei number. S is the actual saturation regarding water and S_0 is the supersaturation regarding water at ice equilibrium at the actual temperature ($(e_l^\star(T)/e_i^\star(T)) - 1$, see also equation 2.3). To avoid unrealistic high values of activated ice at low temperatures, there was a need to limit ice activation at temperatures lower than T_m=246 K (Reisner et al., 1998). Since the two-moment microphysics scheme treats cloud liquid and cloud ice separately and thereby includes the liquid – ice interaction processes, the two-moment scheme is especially suitable for mixed-phase clouds.

Radiation scheme

Arctic clouds do not depend on convection generated by heating of the surface. Instead cloud top cooling due to longwave radiation plays an important role to form Arctic clouds (see section 2.1.3). The radiation scheme in COSMO was developed after Ritter and Geleyn (1992). The parameterization is based on the radiative transfer equation and calculates the change of radiative flux due to cloud particles, aerosol and gases. As input the scheme uses mean values of variables like temperature, specific humidity, cloud fraction, cloud liquid and ice content in separated atmospheric layers. These variables are then converted into radiative properties such as optical depth by using empirical relations. Further, these optical properties are then used to calculate the change in radiation flux due to scattering, absorption and emission. Thereby the scheme accounts for radiation of eight spectral intervals of wavelength. Assuming a plane parallel atmosphere, where neighbouring columns do not interact, reduces the equation to a one-dimensional one. In the vertical fluxes are considered in both upward and downward direction. The calculation of radiation flux requires the atmosphere to be subdivided into layers of mean optical properties. Thereby the scheme allows for partial cloud cover in any model height. Though, for the case of clear interstice in between cloud layers the validity for used assumptions is questioned and discussed further in Ritter and Geleyn (1992). Anyhow, the result is a calculation of the heating rate due to longwave and shortwave radiation in each model height. Thereby the clouds can be modified due to radiation.

Sea ice model

Arctic surface conditions are often defined by sea ice instead of open water. The sea ice causes an increase of albedo and surface roughness (Notz, 2005; Guest and Davidson, 1991). The much higher albedo means an enhanced shortwave reflection. Simultaneously the sea ice acts as an insulation layer and reduces the fluxes of longwave radiation, sensible and latent heat from the ocean to the atmosphere. In order to account for all this when modelling clouds above sea ice, a sea ice scheme was included in the COSMO model (Doms et al., 2011; Mironov and Ritter, 2004). The sea ice scheme does not account for horizontal ice movement and does not initialize new sea ice formation. Though, the scheme accounts for melting and freezing of an existing ice layer as a response to the difference in ocean and atmospheric energy fluxes. Prescribing an initial ice thickness H_{ice}, the evolution of the ice surface temperature with time $\Delta T_{ice}/\Delta t$ is given by

$$\frac{\Delta T_{ice}}{\Delta t} = \frac{1}{c\, H_{ice}} \left[\frac{Q_A + Q_I}{\rho_{ice} C_{ice}} \right]. \tag{5.4}$$

Q_A are atmospheric energy fluxes, Q_I is the vertical conductive flux through the ice layer, ρ_{ice} is the ice density, C_{ice} is the ice heat capacity and c is a shape factor. H_{ice} is variable with time. In case of a surface cooling atmospheric flux, H_{ice} increases. Thereby the vertical conductive flux through the ice layer, Q_I, is computed out of the difference between the assumed constant temperature of $-1.7\,°C$ (freezing temperature of the salty Arctic Ocean) at the ice bottom and the ice surface temperature. In this way Q_I represents the released latent heat due to freezing at the ice bottom. The great advantage of the scheme is that it allows for a more correct surface temperature. Having sea ice means that the surface temperature is much lower than if the surface would be open water.

The ice surface temperature is then used for an adjusted surface albedo. I do not consider any snow on top of the sea ice.

5.2 ASCOS field campaign

In the model initial conditions need to be prescribed. For this I use the radiosounding at 5:31 UTC on 19 August 2008 during the Arctic Summer Cloud Ocean Study (ASCOS) field campaign. On the 19 August 2008 there was a non-seeding multilayer cloud structure between 0 - 14 UTC. The height profiles of pressure, temperature, wind and relative humidity are used. When the model starts there are no clouds existing in the model. Therefore LWC and IWC have to be added to the relative humidity. Thereby the model receives the right total moisture and the clouds can evolve during spin-up. Now the ASCOS field campaign and the measurements taken during the day chosen for initialization are shortly described. In section 6 the model results are validated by comparison to the measurements. The reason for choosing a multilayer cloud from ASCOS and not from Ny-Ålesund is that Ny-Ålesund is surrounded by mountains. To account for the mountains' influence on clouds when modelling is difficult. In contrast, ASCOS was on the sea and thereby in flat environment.

The Arctic Summer Cloud Ocean Study (ASCOS) was conducted between 2 August and 9 September 2008 with the icebreaker Oden. The ship went from Svalbard northwest to the Fram Strait. Pack ice, the marginal ice zone and open water were on their way. At 12 August they anchored in the ice at 87°21′ N and 1°29′ W and then they drifted with the ice until 1 September. During the field campaign various measurements of the boundary layer and clouds were collected. Detailed information is found in Tjernström et al. (2012, 2014).

Between 0 and 14 UTC of the 19 August 2008 the meteorological situation at ASCOS was mainly influenced by a high pressure located south of Svalbard (see figure A.25). The weather was calm and without precipitation. During this time a multilayer cloud occurred and its liquid water content, ice water content and cloud phase are presented in figure 5.1. Ice properties (figure 5.1b)) are based on millimetre cloud doppler radar measurements (Shupe et al., 2005). Liquid water content (figure 5.1a)) is not measured directly. Instead, liquid water path is derived out of the brightness temperature measured with a vertically-pointing, dual-channel (23 and 30 GHz) microwave radiometer. Then, taking cloud boundaries from radar/ceilometer measurements and temperature profiles from the radiosoundings, finally a adiabatic profile of liquid water content was derived (ASCOS Data, 2009). Cloud phase (figure 5.1c)) is based on millimetre cloud radar, microwave radiometer, ceilometer, and radiosoundings. This is explained further in Shupe (2007) and is comparable to Cloudnet (see section 4.5.2). In figure 5.2 the height profiles of temperature (figure 5.2a)) and relative humidity with respect to water and ice (figure 5.2b)) are shown. These variables are taken from the radiosounding at 5:31 UTC on the 19 August 2008. Also LWC and IWC are shown in figure 5.2. Their values are taken from the time indicated by a red line in figure 5.1. In the lowest kilometre (0 km to 1 km) temperatures (see figure 5.2a)) were just below 0 °C. Relative humidity was at about 100% both regarding RH_{liq} and RH_{ice} (see figure 5.2b)). In figure 5.1 in the height between 0 km to 1 km a cloud of both mixed-phase (dark yellow in figure 5.1c)) and ice (blue in figure 5.1c)) exists. In figure 5.2a) cloud top (1 km) becomes visible through a slight temperature inversion. In the height level between 1 km to 3 km there is no

cloud (see figure 5.1). Temperatures were between 0 °C to −10 °C (see figure 5.2a)). In the levels between 1.7 km to 2.3 km relative humidity with respect to ice was slightly above 100%, while in the height between 2.3 km to 3.0 km the relative humidity was much lower. Between 3 km and 4 km the upper cloud evolved (see figure 5.1). In this level there was supersaturation regarding ice, but subsaturation regarding water (see figure 5.2c)). The cloud existed of ice (blue in figure 5.1) and mixed-phase (dark yellow in figure 5.1) and had a liquid cloud top (light blue in figure 5.1). At 3.6 km both *LWC* and *IWC* reach their maxima (see figure 5.2). Temperatures were between −10 °C and −20 °C (see figure 5.2a)). Again a temperature inversion was visible at cloud top.

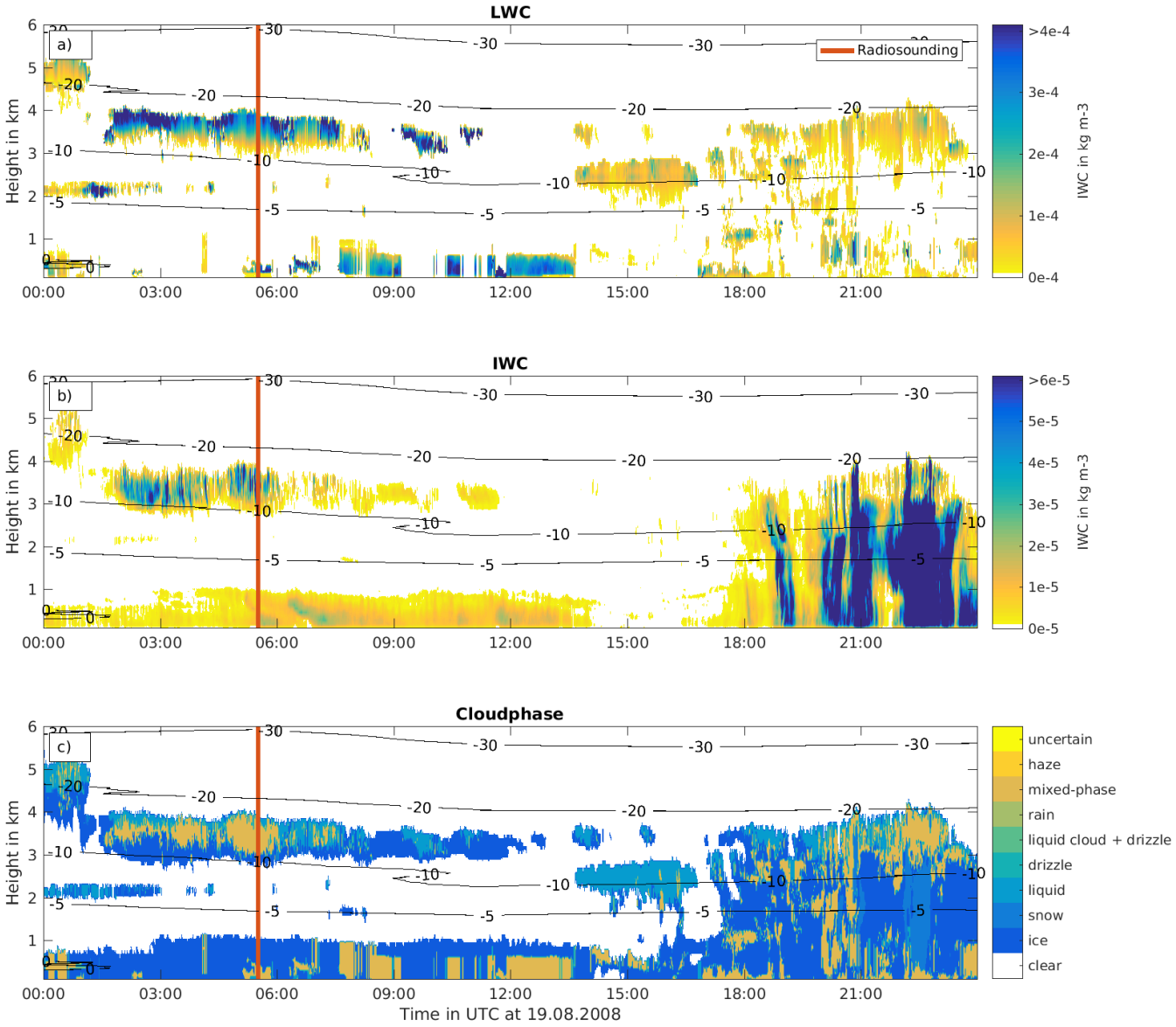

Figure 5.1: 19 August 2008 during ASCOS: a) liquid water content, b) ice water content, c) cloud phase. The red line shows the time of the radiosounding used in the model (ASCOS Data, 2009).

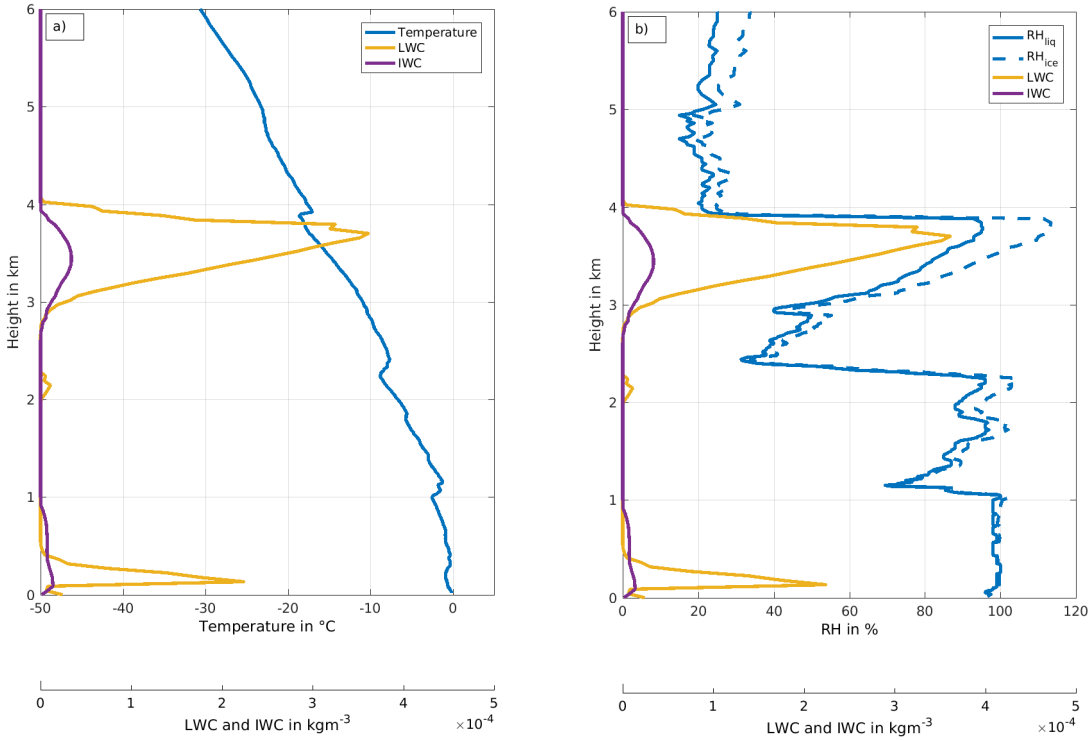

Figure 5.2: Overview over different height profiles measured at 5:31 UTC on the 19 August 2008 during ASCOS: a) Temperature, LWC and IWC. b) Relative humidity with respect to water (RH_{liq}), relative humidity with respect to ice (RH_{ice}), LWC and IWC (ASCOS Data, 2009).

6 Model simulations: Cloud interaction by radiation

For the COSMO simulations, where I want to study the radiative interactions of multilayer clouds, some case specific settings are needed. The setup is semi-idealized, which means that there is no outer three-dimensional field of initial variables. Instead initial conditions are adjusted by the radiosounding at 5:31 UTC on 19 August 2008 during ASCOS, as described in section 5.2. The model domain is at the size of 6.3 km x 6.3 km and has a horizontal resolution of 100 m. The center of the model domain is at 87°49′ N and 9°37′ W. This equals the position of ASCOS on the 19 August at 5 UTC. In the vertical the domain reaches until 22 km and has 200 levels. At the surface these levels are the closest and have a increasing distance above. The lowest level is at the surface, the first level at 17.10 m, the second level at 42.15 m. Boundary conditions are set to be periodic, which means that the opposite sites (north/south and east/west) are interconnected. The surface is sea ice of 1 m thickness and its surface roughness is 0.01 m. The temperature at the sea ice to air transition is -3.15 °C.

The model run started at 5 UTC and was then running for 10 hours with a time step of 2 s. In the first two hours all cloud ice processes were turned off in order to let a liquid cloud develop first. After approximately 4 hours all spin up processes are finished. I set the cloud droplet number *QNC* to be constant. The model has also the option to prescribe not the cloud droplet number *QNC* but the *CCN* concentration. Though, in that case the number of cloud droplets activated becomes much too small. This is connected to a modelled vertical velocity only being downwards in which cloud droplet activation is not possible. Instead *QNC* is set to be constant at $30 \times 10^6\,\mathrm{m}^{-3}$. Deciding a reasonable value for a constant *QNC* depends on two considerations. Firstly, *QNC* should agree with the ACSOS observations. *CCN* concentrations during ASCOS were usually less than $100 \times 10^6\,\mathrm{m}^{-3}$. On the 19 August 2008 the *CCN* concentration varied between $10 \times 10^6\,\mathrm{m}^{-3}$ to $35 \times 10^6\,\mathrm{m}^{-3}$ (ASCOS Data, 2009). I assume further, similar to Mauritsen et al. (2011), that the *CCN* number and *QNC* number are of approximately the same magnitude. Secondly, modelled *LWP* is influenced by the *QNC* number (constant *QNC* reaching a maximum droplet size leads to precipitation and thereby reduction in *LWP*) and therefore also a reasonable *LWP* (see section 6.1.1) is taken into account when I choose $QNC = 30 \times 10^6\,\mathrm{m}^{-3}$.

The number of activated ice nuclei (N_I) is calculated in COSMO by using equation 5.3 and an initial ice nuclei number of $N_0 = 1 \times 10^{-2}\,\mathrm{m}^{-3}$. This ice nuclei number is a good approximation for the mid-latitudes. In my case this resulted in an upper cloud only consisting of ice. In order to get an upper mixed-phase cloud, as it was measured during ASCOS (see figure 5.1), N_0 was reduced to $1 \times 10^{-3}\,\mathrm{m}^{-3}$. Less initial ice nuclei means less activated ice nuclei and thereby less cloud ice is able to form. The reduction of the amount of initial available ice nuclei is justified in the way, that the amount of Arctic aerosol is usually lower than in mid-latitudes. Additionally,

Arctic aerosol conditions often reach a seasonal minimum in summer (see section 2.1.2). Since my reference case took place during Arctic summer (19 August 2008) and in order to get a cloud similar to the observations (see figure 5.1), it seems acceptable to reduce the initial ice nuclei number in my simulations.
A setting of very slow autoconversion (cloud droplet to raindrop conversion) turned out to be useful. This led to a reduce of the removal of cloud moisture during the spin up due to precipitating rain and snow. The setting of very slow autoconversion uses a wider width parameter for the particle size distributions (generalized gamma distributions) than the default setting uses (width parameter $\nu = 6.0$, exponential parameter $\mu = 1.0$ instead of $\nu = 0.33$, $\mu = 0.66$).
These specifications are all used in the following model simulations. In order to understand the radiative effects two clouds have on each other three cases are considered: Firstly a standard run being the best representation of the observed multilayer cloud structure is shown. Secondly the low cloud is varied (removed) in order to understand its effect on the upper cloud. Thirdly the upper cloud is varied (removed and moved) in order to understand its influence on the lower cloud.

6.1 The standard run

The standard run uses the radiosounding at 5:31 UTC on the 19 August 2008 during ASCOS as described in section 5.2. In order to get the correct amount of liquid as input for the model, *LWC* and *IWC* are added to the existing humidity profile. This modified relative humidity profile is shown in figure A.26. The semi-idealized model setup leads to horizontal homogeneous variables. There were then horizontally averaged and only the time evolution of the different variables is shown in the following. Since the cloud number concentration is prescribed, no big changes are expected with time. The resulting plot is shown in figure A.27. The model start time was at 5 UTC. This equals 0 in the plots. Ice processes were turned on after 2 hours and it becomes visible in the plot that spin up of the microphysical processes are finished after 4 hours. This is indicated by a solid black line.
In order to study the atmospheric stratification the potential temperature and the equivalent potential temperature are used. The potential temperature θ is defined as

$$\theta = T \left(\frac{P_0}{P} \right)^{R_{air}/cp}. \tag{6.1}$$

Here T is the temperature, P_0 is a reference pressure, P is the pressure, R_{air} is the specific gas constant of dry air and c_p is the specific heat capacity of air. The equivalent potential temperature θ_e is defined as

$$\theta_e = \theta \exp \left(\frac{L_v \, q_v}{cp \, T} \right) \tag{6.2}$$

were additionally L_v is the latent heat of condensation and q_v is the specific humidity. It becomes clear that the potential temperature includes only temperature, whereas equivalent potential temperature includes both temperature and moisture in the calculation. Further, constant potential and equivalent potential temperature with height means neutral stratification, increasing potential and

equivalent potential temperature with height means stable stratification and decreasing potential and equivalent potential temperature with height means labile stratification. The more labile the stratification is, the more buoyancy driven mixing is possible.

6.1.1 Results of the standard run in comparison to ASCOS measurements

In figure 6.1 the *LWC* and *IWC* of the modelled multilayer cloud structure is shown. In table 6.1 values of the model are compared to those of the measurements. In the model after the spin-up a mixed-phase upper cloud has developed between 3 km and 4 km. A thin layer of liquid occurs at cloud top and the rest of the upper cloud is only ice containing. The heating rate due to shortwave and longwave radiation is shown in figure 6.2. The calculation of the heating rate (for both shortwave and longwave in all following figures) was done by averaging over the time after the spin up. The shortwave heating is continuously warming (positive values in figure 6.2a)). Maximum values occur at cloud top of the upper cloud (in 4 km height, see table 6.1). Inside the upper cloud shortwave warming is slightly higher (at 3.5 km height) than in the non cloudy area below (between 1 km to 3 km height). The longwave heating is continuously cooling (negative values in figure 6.2b)). Maximum cooling occurs at cloud top of the upper cloud in 4 km height (see table 6.1). Inside the upper cloud (3.5 km height) there is slightly more cooling than in the non cloudy part below (between 1 km to 3 km height). In figure 6.3 the evolution of the temperature (see figure 6.3a)) and the potential temperature (see figure 6.3b)) is shown. Temperatures of the upper cloud are between $-10\,°C$ and $-20\,°C$ (blue line in figure 6.3a)). At cloud top a strong temperature inversion occurs. The potential temperature shows a very well mixed, neutral stratification for the upper cloud (blue line between 3 km to 4 km in figure 6.3b)). Both the temperature inversion and the neutral stratification strengthens towards the end of the simulation time (blue after 4 h, purple after 7 h and red after 10 h in figure 6.3a) and b)) due to the continuous longwave cooling rate at cloud-top. Since shortwave warming at cloud top is of one magnitude smaller than longwave cooling this does not limit the cloud top cooling noticeable.

In both the model and the observations the upper cloud is a mixed-phase cloud with a liquid cloud top (see figure 6.1 and 5.1). The modelled height and the thickness of the upper cloud agrees well with the observations. Even if the model shows slightly lower values of *LWC*, the size of magnitude is the same (see table 6.1). Though the vertical extend of *LWC* does only contain the upper cloud top in the model, but the entire upper cloud in the observations. Modelled *IWC* in the upper cloud is in accordance to the measurements (see table 6.1). Both the model and the observations show a strong temperature inversion at the upper cloud top (see blue and yellow line at 4 km height in figure 6.3a)). Though, the inversion in the model is slightly stronger than in the measurements and this becomes even more visible in the potential and equivalent potential temperature (see blue and yellow line and dotted line at 4 km height in figure 6.3b)).

Besides the upper cloud, the simulation shows a lower cloud at a height of 0 km to 0.5 km (see figure 6.1). This lower cloud is entirely liquid (see values in table 6.1). At the end of the simulation time (after 9 to 10 hours) a very thin liquid cloud layer at 1 km forms additionally. Maximum shortwave warming is much less pronounced than in the upper cloud (see figure 6.2a)). Also longwave cooling at cloud top is much less pronounced than in the upper cloud and just slightly more than in the non cloudy areas (between 1 km to 3 km). The stratification of the lower cloud (0 km to

1 km height) is more stable than that of the upper cloud (yellow and blue line in figure 6.3b)) and there is no evolution with simulation time. Modelled temperatures between 0 km to 1 km height are between 0 °C and −3 °C (see figure 6.3a)). A temperature increase at 1 km height exists, but is very weak.
Compared to the measurements, in the model the lower cloud is too thin (see figure 5.1c), figure 6.1 and table 6.1). Additionally in the model the lower cloud is entirely liquid, whereas in the measurements the lower cloud contains mainly ice and only to a smaller extend also mixed-phase (see 5.1b) and c)). The stratification is in both the model and the observations stable (blue and yellow line between 0 km to 1 km height in figure 6.3b)). Though, in the measurements the equivalent potential temperature does show an slight inversion at the height of 1 km (yellow dash-dotted in figure 6.3b)). This inversion is not visible in the modelled equivalent potential temperature (blue dash-dotted in figure 6.3b)). These discrepancies, especially regarding thickness and ice content, in the lower cloud are the mayor differences between model and observations.

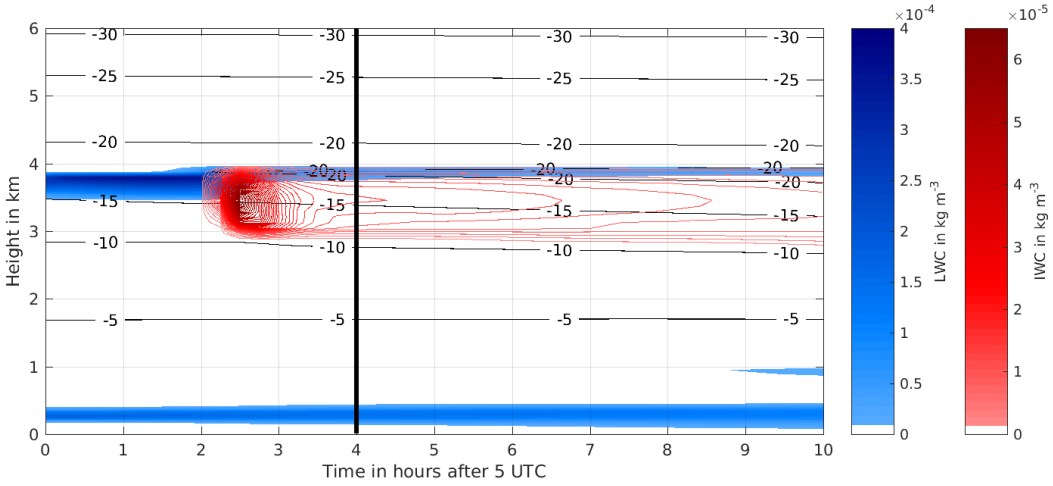

Figure 6.1: Standard run: Cloud liquid water content (*LWC*) in blue and cloud ice content (*IWC*) in red. The time of finished spin-up is indicated by the solid black line. Thin black lines indicate the temperatures in °C.

In figure 6.4 the modelled *LWP* and *IWP* are shown and in figure A.28 the modelled rain and snow content are shown. Both *LWP* (see figure 6.4a)) and *IWP* (at 2-3 h in figure 6.4b)) reach maximum values before spin up. Then, between 2 and 3 hours of simulation there are high amounts of rain and snow precipitation (see figure A.28). Due to this loss of moisture, after spin-up modelled *LWP* is little (see table 6.1). In figure 6.5 the measured *LWP* (figure 6.5a)) is shown for the time 5 - 11 UTC on the 19 August 2008 during ASCOS. Between 5 and 8 UTC *LWP* shows slightly higher values than between 8 and 10 UTC, but overall the measured *LWP* is much higher than the modelled one (see table 6.1). The measured *IWP* (figure 6.5b)) shows quite high variability between 5 - 6 UTC. After 6 UTC *IWP* is more constant and the measured *IWP* is thereby in good agreement with the modelled *IWP* (see table 6.1).

6.1.2 Discussion of the standard run

LWC was not measured directly during ASCOS but was derived out from *LWP* (see table 6.1). Therefore *LWC* might not be correct and *LWP* is a much more reliable variable to use for compar-

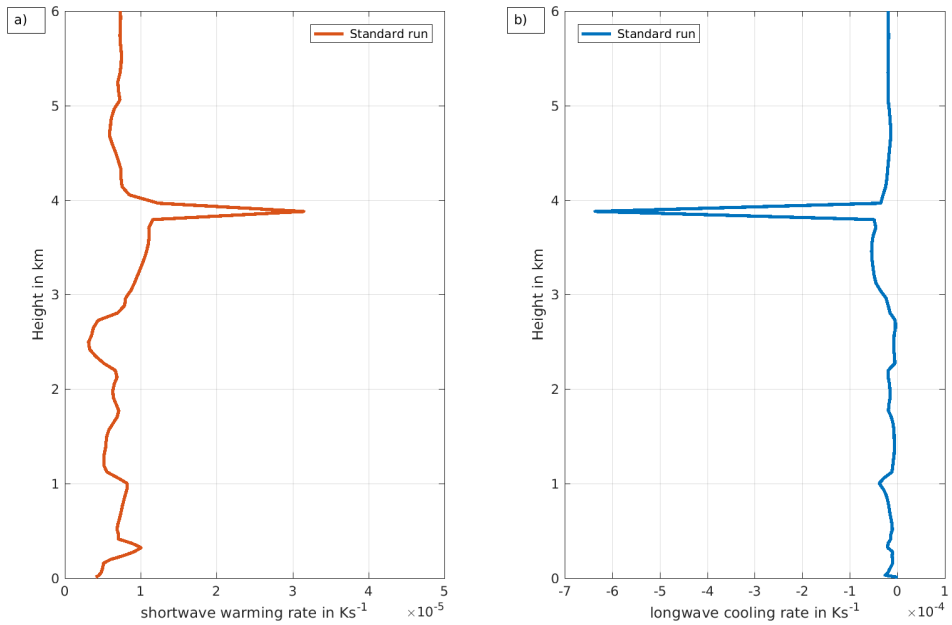

Figure 6.2: Standard run: a) Shortwave warming and b) longwave cooling rate. Negative values means cooling, positive values means warming. For the averaging only the time after finished spin-up is used.

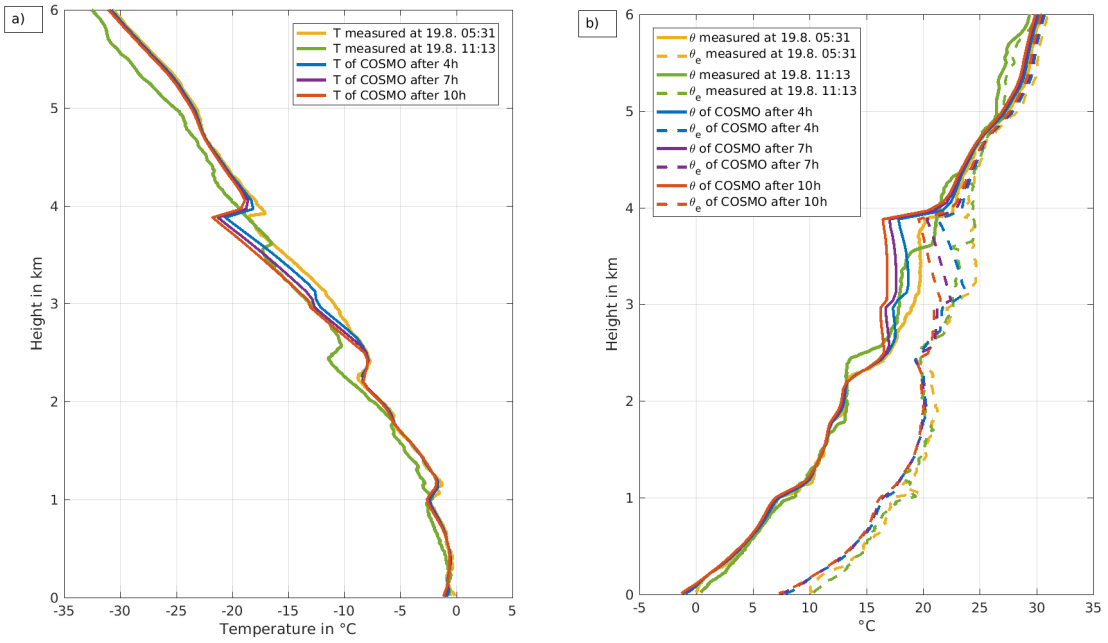

Figure 6.3: Standard run: a) Temperature height profiles and b) Height profiles of potential temperature (lines) and equivalent potential temperature (dash-dotted). The measured profiles are taken from ASCOS observations (ASCOS Data, 2009). The COSMO height profiles are the modelled ones.

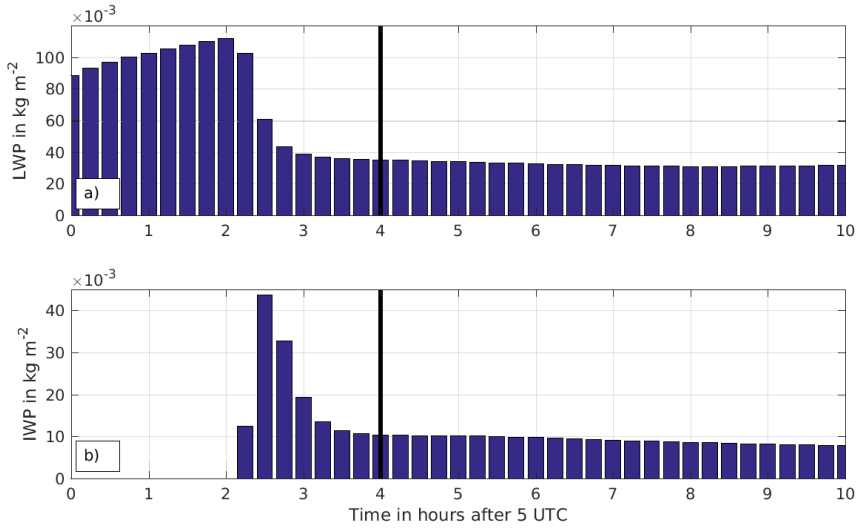

Figure 6.4: Standard run: a) Liquid water path LWP and b) ice water path IWP. The time of finished spin-up is indicated by the solid black line.

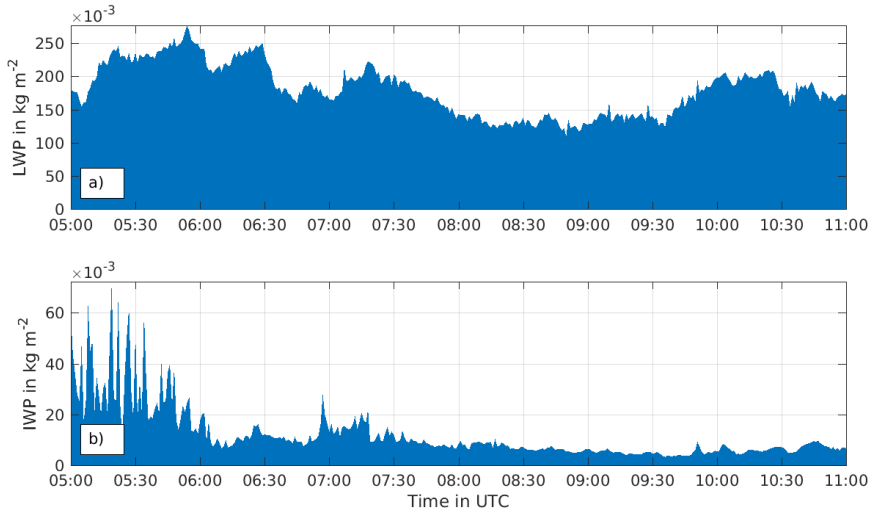

Figure 6.5: Measured: a) Liquid water path LWP and b) ice water path IWP between 5 and 11 UTC at the 19 August 2009. Data from ASCOS Data (2009).

ison. The model strongly underpredicts LWP. This might be due to the missing LWC in the upper cloud, except at cloud top. IWP of the model and the simulations is in good accordance. A similar model to observations comparison was done by Morrison et al. (2009) regarding Arctic multilayer clouds. For single layer clouds their models often underpredicted LWP and overpredicted IWP. For multilayer clouds their models often overpredicted LWP but underpredicted IWP. This result is not in agreement with my result where I got a underprediction of LWP and a IWP similar to the observations.

The model adjustment to very slow autoconversion and the reduction of the initial ice nuclei concentration (N_0) do both influence modelled LWP and IWP. Higher initial ice nuclei concentration would lead to even less LWP and the upper cloud would be entirely icy. Using fast autoconversion instead of slow autoconversion leads to high precipitation and thereby loss of cloud liquid and ice

Table 6.1: Comparisons of standard run to ASCOS measurements. Values of shortwave (SW) warming and longwave (LW) cooling refer to cloud top.

	Standard run	ASCOS measurements
upper cloud		
	3 – 4 km	3 – 4 km
	$T = -10\,°C$ and $-20\,°C$	$T = -10\,°C$ and $-20\,°C$
	$LWC = 1 \times 10^{-4}\,kg\,m^{-3}$	$LWC = 3 \times 10^{-4}\,kg\,m^{-3}$
	$IWC = 1 \times 10^{-5}\,kg\,m^{-3}$	$IWC = 1 \times 10^{-5}$ to $4 \times 10^{-5}\,kg\,m^{-3}$
	SW warming $3.3 \times 10^{-5}\,K\,s^{-1}$	
	LW cooling $-6.2 \times 10^{-4}\,K\,s^{-1}$	
lower cloud		
	0 – 0.5 km	0 – 1 km
	$T = 0\,°C$ to $-3\,°C$	$T = 0\,°C$ to $-3\,°C$
	$LWC = 1 \times 10^{-4}\,kg\,m^{-3}$	$LWC = 0\,kg\,m^{-3}$ and $3 \times 10^{-4}\,kg\,m^{-3}$
	no IWC	$IWC = 1 \times 10^{-5}\,kg\,m^{-3}$
	SW warming: $1.0 \times 10^{-5}\,K\,s^{-1}$	
	LW cooling: $-0.4 \times 10^{-4}\,K\,s^{-1}$	
both clouds in total		
	$LWP = 30 \times 10^{-3}\,kg\,m^{-2}$	$LWP = 100 \times 10^{-3}$ to $250 \times 10^{-3}\,kg\,m^{-2}$
	$IWP = 10 \times 10^{-3}\,kg\,m^{-2}$	$IWP = 10 \times 10^{-3}\,kg\,m^{-2}$

before end of spin up. Also this does not improve the modelled LWP. Therefore the decision is to use the settings described above as the standard.

The shortwave warming rate is of one order of magnitude smaller than the longwave cooling rate (see table 6.1). The standard run is repeated for December instead of in August (see figure A.29). In the December run there is no shortwave radiation due to polar night but the same cloud structure as in August develops. These arguments prove that the influence of shortwave radiation on Arctic multilayer clouds is negligible in contrast to longwave radiation.

The stratification of the upper cloud in both the model and the observations is strongly neutral (see blue and yellow line between 3 km to 4 km height in figure 6.3b)). This neutral stratification allows for in-cloud mixing and thereby cloud formation. In contrast the stratification of the lower cloud is stable in both the model and the observations (see blue and yellow line between 0 km to 1 km height in figure 6.3b)). Though, even in stable environment the lower cloud develops. Verlinde et al. (2013) did also a study about the stratification in multilayer clouds. For this they used the measured multilayer cloud presented in figure 2.6, but the time period was prolonged. As they found the lower cloud to be in more stable environment than the upper cloud our results are in good agreement with theirs. This result verifies the assumption shown in figure 2.8 where the mixing of the lower cloud is less strong than that of the upper cloud.

6.2 Lower cloud variation

In order to understand if the lower cloud affects the upper cloud a simulation where the lower cloud is removed is done. The initial input for this is shown in figure 6.6. The relative humidity regarding water RH_{liq} is reduced to 90% between 0 km to 1 km height. The resulting LWC and IWC is shown in figure 6.7. When the lower cloud is removed the upper cloud is very similar to the upper cloud in the standard case. The upper cloud consists of a thin liquid layer at cloud top and the rest of the upper cloud contains only ice. All in all removing the lower cloud does not influence the upper cloud.

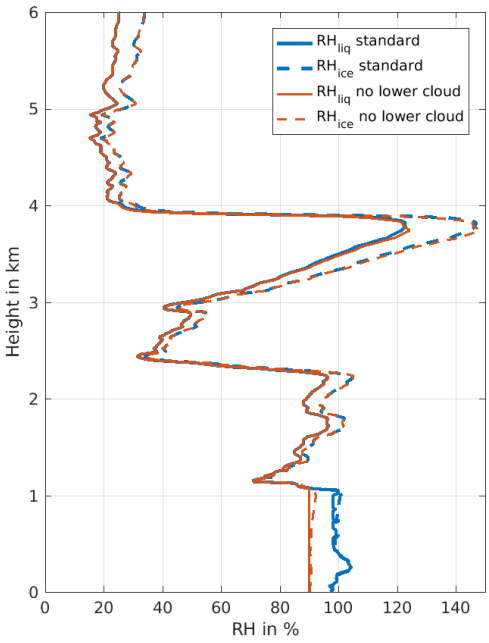

Figure 6.6: No lower cloud: Relative humidity regarding water RH_{liq} and regarding ice RH_{ice} as input for the run without lower cloud in red. The standard is shown for comparison in blue.

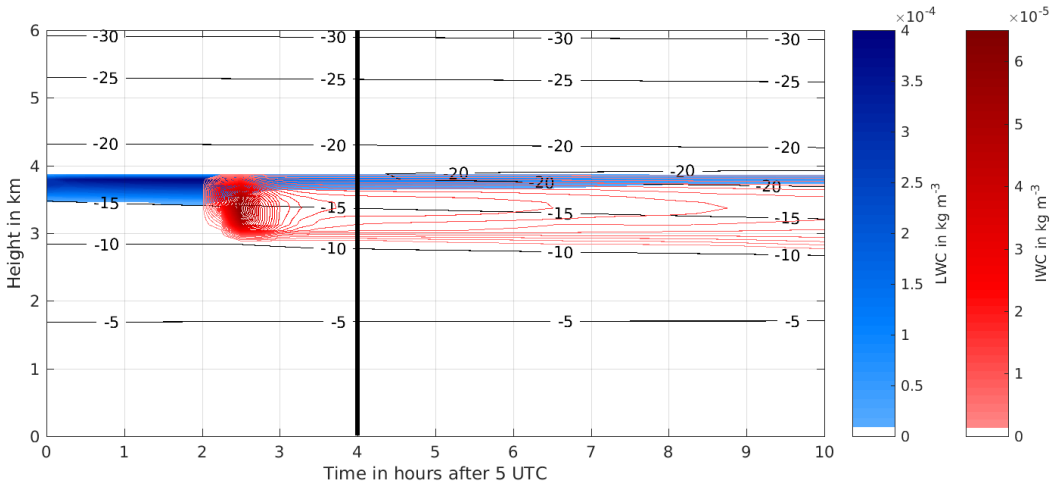

Figure 6.7: No lower cloud: Cloud liquid water content (LWC) in blue and cloud ice content (IWC) in red. The time of finished spin-up is indicated by the solid black line. Thin black lines indicate the temperatures in °C.

6.3 Upper cloud variations

In order to understand how the upper cloud influences the lower cloud, two simulations where the upper cloud is modified are done. First the upper cloud is removed. The resulting initial input for COSMO is shown in figure 6.8a). Between 3 km to 4 km height RH_{liq} had to be lowered to maximum 60% in order to remove the upper cloud. In addition to that a reduction of RH_{liq} to maximum 80% between 1.2 km to 3 km height was needed. Else there would have been cloud formation at this level. Secondly the upper cloud is moved further down. The resulting initial input for this case is shown in figure 6.8b). Moving the upper cloud further up would cause the upper cloud to glaciate completely, then precipitating snow would cause the upper cloud to dissipate. As this leads to a single lower cloud, this is not shown.

6.3.1 Results: No upper cloud

Removing the upper cloud leads to LWC and IWC as shown in figure 6.9. Without an upper cloud the lower cloud becomes very different in comparison to the standard run (see figure 6.1). Note the different scales in figure 6.9 and in figure 6.1. The new lower cloud reaches from 0 km to 1.2 km. Between 0 km to 0.5 km there is a liquid layer. This is very similar to the liquid layer in the lower cloud of the standard run. At cloud top in the no upper cloud run there is a second liquid layer between 0.7 km to 1.2 km height. In figure 6.9 the lower cloud seems to be mixed-phase. Though it is noticeable that IWC is of the magnitude only of about $4 \times 10^{-9}\,\mathrm{kg\,m^{-3}}$. This is more ice in the lower cloud than in the standard run, but still less than in the observations. In this way, the removal of the upper cloud leads to a strengthened lower cloud of primarily liquid.

The strengthened lower cloud is due to the changed balance in longwave radiation as described in section 2.2.4. At the lower cloud top the balance in longwave radiation is given by outgoing and incoming radiation. When there is no upper cloud, then the incoming radiation is only from the much colder atmosphere (space) above (see equation 2.14). In contrast, in the existence of an upper cloud, the incoming radiation is modified (see equation 2.15). Firstly we have the atmospheric

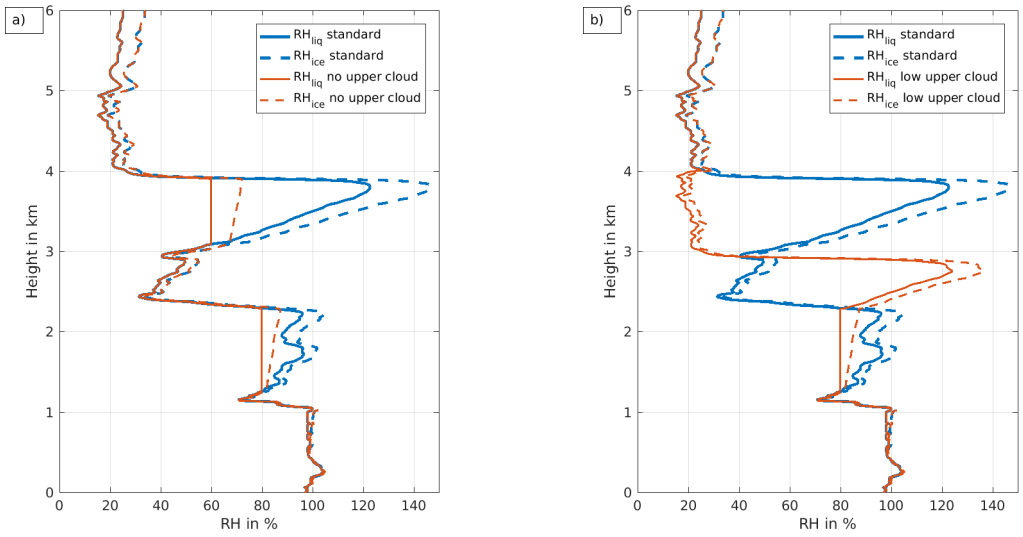

Figure 6.8: Upper cloud variations: a) No upper cloud b) lower upper cloud than standard. Relative humidity regarding water RH_{liq} and regarding ice RH_{ice} as input for the run without upper cloud in red. The standard is shown for comparison in blue.

layer between the two clouds and secondly we have the upper cloud. As these two components radiate downwards in the longwave and this radiation flux is mainly determined by the 4^{th} power of their temperature, it becomes clear that this flux is much greater than that from space. Thereby the radiation balance at the lower cloud top is changed. In the absence of an upper cloud the outgoing longwave flux at cloud top is much greater than the incoming longwave flux. This becomes visible through the increased longwave cooling rate at cloud top (see figure A.30b)). The shortwave heating (see figure A.30a)) is again of one magnitude smaller than the longwave cooling and therefore negligible. The enhanced cloud top cooling of the lower cloud becomes also visible in the temperature profile (see figure 6.10a)) and in the potential temperature profile (see figure 6.10b)). Now the temperature inversion at the lower cloud top is much more pronounced in comparison to the standard run (see blue line in at 1 km height in figure 6.10a)). Out of the cloud top cooling also a more neutral stratification develops in the lower cloud (see blue, purple and red line in between 0.5 km to 1.2 km height in figure 6.10b)). As the more neutral stratification enables in-cloud mixing all components together lead to a classical mixed-phase cloud as described in section 2.1.3. In this way the conditions for the formation of a mixed-phase cloud are much more favourable than in the standard run and the lower cloud is thereby strengthened.

The result of a strengthened lower cloud when there is no upper cloud seems to be in agreement with the observations between 8 UTC -14 UTC, given that we assume the measurements to be reliable. During 8 UTC -14 UTC the upper cloud has less liquid (see figure 5.1a)) and the lower cloud shows slightly more liquid, in addition to the same amount of ice, than before (mixed-phase between 8 UTC - 14 UTC in contrast to only ice between 1 UTC - 8 UTC in figure 5.1c)).

The vertical extent of the lower cloud without the upper cloud (0 km to 1.2 km in figure 6.9) agrees quite good with the vertical extend of the observed lower cloud (0 km to 1 km height between 5

- 11 UTC in figure 5.1). Also the cloud phase now being more mixed-phase, even if still not reaching the measured *IWC* values, agrees better with the measurements (figure 5.1c)). This rises the question of the influence of the upper cloud on the lower cloud being too strong. This influence is calculated by the radiation scheme in the model and is due to a too high longwave downward flux from the upper cloud. According to equation 2.17 mainly temperature and emissivity of the upper cloud (see equation 2.17 and section 5.1) should influence this downward longwave flux and therefore these two components are now investigated.

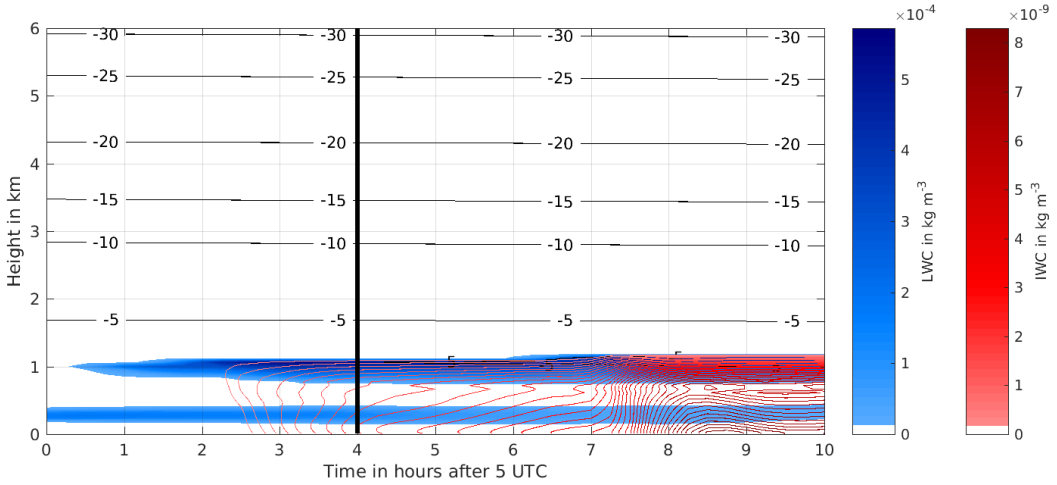

Figure 6.9: No upper cloud: Cloud liquid water content (*LWC*) in blue and cloud ice content (*IWC*) in red. The time of finished spin-up is indicated by the solid black line. Thin black lines indicate the temperatures in °C. Note the different scale than in figure 6.1.

6.3.2 Results: Lower upper cloud than standard

In order to understand the effect of the upper cloud on the lower cloud in the model even better, the upper cloud is moved to a lower height. Lowering the height of the cloud means mainly increasing the temperature of the cloud and thereby changing the proportions of cloud liquid and cloud ice. For moving the upper cloud from 3 km–4 km height, as in the standard run, down to 2 km–3 km height I use the initial input profile shown in figure 6.8b). This leads to the multilayer cloud structure shown in figure 6.11. The upper cloud shows a thick layer of liquid between 2.6 km to 3 km height. The upper cloud consists also of ice and thereby the *IWC* values are increasing towards the end of the simulation time. Even at simulation end the values are of the size smaller than in the standard run. Both the increased liquid and the reduced ice are in agreement to the warmer temperatures. Similar as in the standard run shortwave warming is of one order of magnitude smaller than the longwave cooling. The longwave cooling causes high cloud top cooling at 3 km height (see figure A.31). Further, quite similar to the standard run, the longwave cloud top cooling at the upper cloud top leads to a temperature inversion (at 3 km height) and neutral stratification below (see figure A.32). In the upper cloud (3 km to 4 km height) temperatures are between -7 °C to -16 °C and this is warmer than in comparison to -10 °C to -20 °C in 3 km–4 km height in the standard run. The lower cloud (see figure 6.11) does not change much compared to the standard (see figure 6.1). In both cases the lower cloud only contains water and reaches from 0 km to 0.5 km height. In the lower cloud temperatures are similar as in the standard run, between 0 °C to -3 °C.

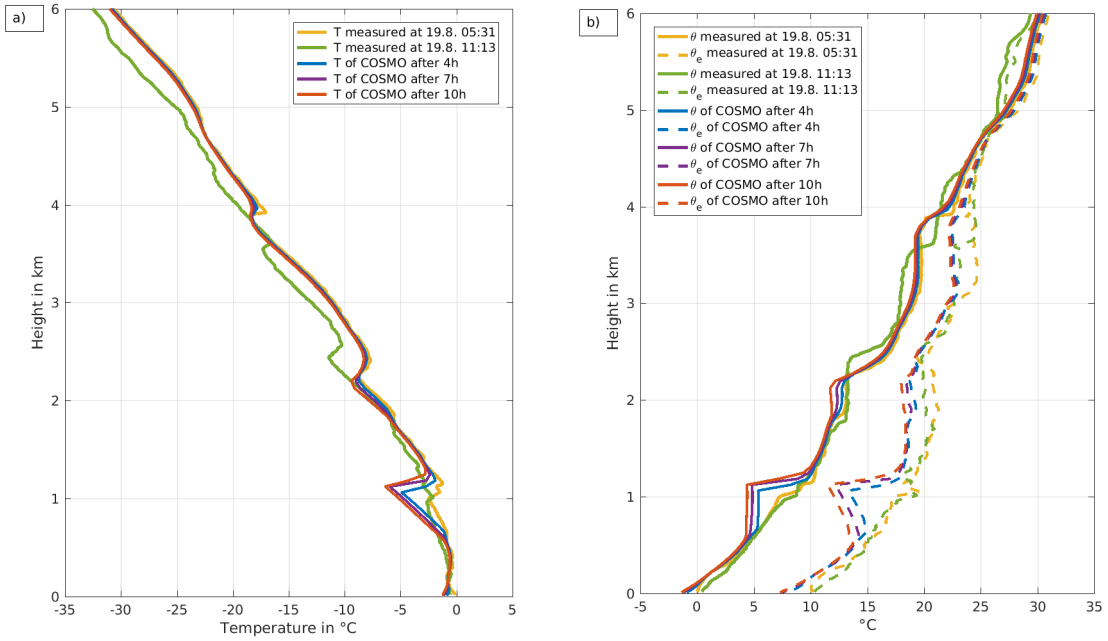

Figure 6.10: No upper cloud: a) Temperature height profiles and b) Potential temperature height profile. The measured profiles are taken from ASCOS observations (ASCOS Data, 2009). The COSMO height profiles are modelled.

A lowered upper cloud into warmer temperatures does also occur in the measurements. At 13 UTC a middle cloud evolves between 2 km to 3 km height (see figure 5.1c)). This middle cloud is only liquid and in the temperature range between $-5\,°C$ to $-15\,°C$. Thereby these temperatures are similar to those of the modelled lowered cloud ($-7\,°C$ to $-16\,°C$). In the observations when the middle cloud exists the lower cloud weakens significantly.

In figure 6.12 a) the modelled LWP and in figure 6.12 b) the modelled IWP is shown for the lower upper cloud run. IWP is increasing after spin up and reaches at the end of the simulation time values similar as in the standard run. LWP is constant at $130 \times 10^{-3}\,kg\,m^{-2}$ and this is much more in agreement with the observations than the standard run is (see table 6.1). This higher LWP is due to the thicker liquid layer of the upper cloud in the lower upper cloud run and this is the major difference to the standard run.

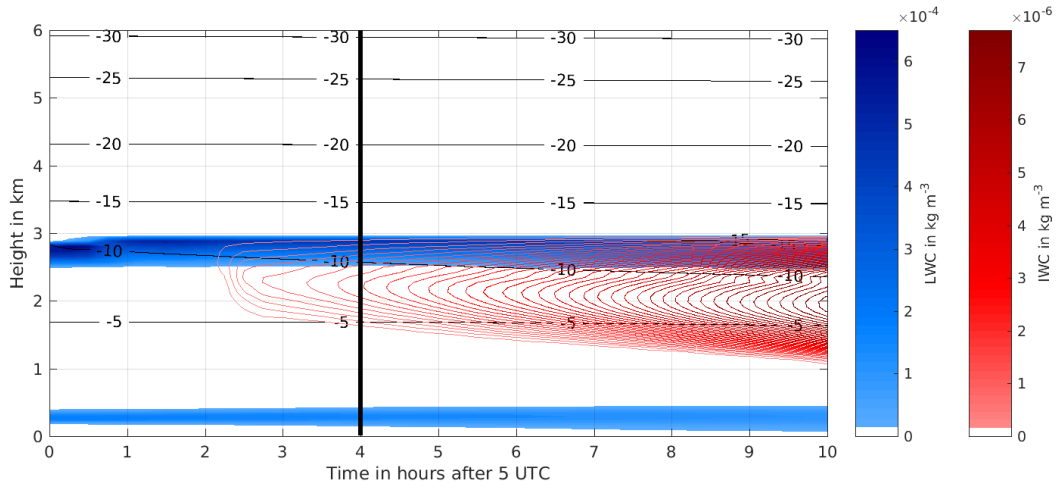

Figure 6.11: Low upper cloud: Cloud liquid water content (*LWC*) in blue and cloud ice content (*IWC*) in red. The time of finished spin-up is indicated by the solid black line. Thin black lines indicate the temperatures in °C. Note the different scale than in figure 6.1.

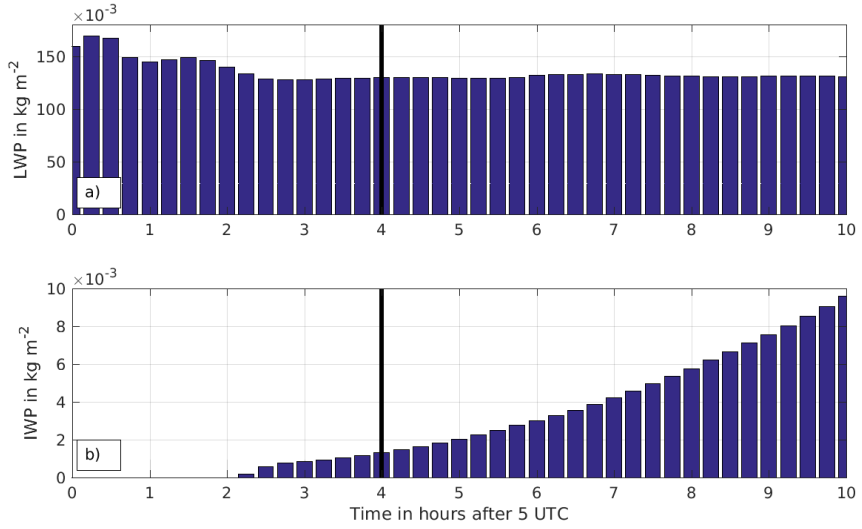

Figure 6.12: Low upper cloud: a) Liquid water path *LWP* and b) ice water path *IWP*. The time of finished spin-up is indicated by the solid black line.

6.4 Discussion

The model shows that there is no influence of the lower cloud on the upper cloud. This is in accordance to the concept of cloud top cooling being the most important aspect causing and maintaining Arctic mixed-phase clouds (see section 2.1.3). This is also in agreement to Sotiropoulou et al. (2014). They showed that when there are stable conditions below a well-mixed cloud layer, then the influence of the stable layers are not of importance for the cloud in the well-mixed layer. With the no upper cloud simulation (see figure 6.9) it becomes clear that the lower cloud is strongly affected by the upper cloud. Removing the upper cloud leads to a strengthened lower cloud. This strengthening is mainly visible in the *LWC* as an additional liquid layer forms at cloud top (at 1 km height in figure 6.9) in comparison to the standard run (see figure 6.1). In the no upper cloud case there is also some ice in the lower cloud, but this is of the magnitude of about 4×10^{-9} kg m^{-3} and

therefore negligible small. The remarkable change of the lower cloud comes from enhanced cloud top cooling in comparison to the standard run. Through enhanced cloud top cooling a stronger temperature inversion develops (see blue line in figure 6.10a) and figure 6.3a)) and thereby a more neutral stratification (see blue line in figure 6.10b and figure 6.3b)) allows for more in-cloud mixing and a stronger lower cloud than in the standard run. The assumption done in figure 2.8 that the lower cloud is thinner in the multilayer case (right in figure 2.8) than in the single layer case (left in figure 2.8) is hereby shown.

The enhanced cloud top cooling of the lower cloud is due to the removed upper cloud. An upper cloud influences the lower cloud by downward longwave radiation, which is given by temperature and emissivity of the upper cloud. This is in accordance to equation 2.17. In contrast, when the upper cloud is moved downwards into a warmer temperature range, the low cloud is not influenced by the upper cloud. As a lowered upper cloud causes higher cloud temperatures and much higher LWP than in the standard run this stands in conflict with equation 2.17.

The downward longwave radiation of a cloud depends only on LWP until LWP=$30 \times 10^{-3}\,\mathrm{kg\,m^{-2}}$ (see section 2.1.4). Above this LWP threshold a cloud emits as a black body and a further increase of LWP does not influence the longwave radiation any more. This LWP threshold could help to explain why the low cloud does not change with a higher LWP in the lower upper cloud run than in the standard run. In the lower upper cloud run LWP is at $130 \times 10^{-3}\,\mathrm{kg\,m^{-2}}$ which is much higher than the LWP limit. Further, in the standard run LWP is at $30 \times 10^{-3}\,\mathrm{kg\,m^{-2}}$, and even if taking away the LWP belonging to the lower cloud, LWP is close to the LWP threshold. In this way, the influence of increased LWP on the downward longwave radiation is therefore expected to be small. The radiation scheme does take the LWC into account when calculating the downward radiation. Though, in order to understand if the radiation scheme also takes this LWP limit into account, further investigation is needed.

However, besides of LWP, the longwave downward radiation is also determined by temperature. The no upper cloud run indicated that the downward radiation flux in presence of an upper cloud was to high. Since temperature influences longwave radiation with the 4^{th} power, an impact on the lower cloud would be expected when the upper cloud is warmer. This was the case in the observations (between 13 -16 UTC in figure 5.1c)) but not in the lower upper cloud run. In order to understand this further, a closer look on the radiation scheme used in the model would be necessary. It seems that the treatment of radiative interactions between multiple cloudy and non-cloudy layers is insufficient. The definition of theses layers and thereby the calculation of the mean temperature inside these layers should be investigated. Secondly, further examples in the measurements would also be helpful.

Another discrepancy of the model and the observations is the general simulation of the lower cloud. While in the observations this cloud to a large extend contains ice (blue in figure 5.1c)), in the simulations it is entirely liquid. Removing the upper cloud leads to a better representation, especially regarding the vertical extend. Though, in the model the strengthened lower cloud in the absence of the upper cloud goes in hand with strong cloud top cooling (see blue line between 0.5 km to 1.2 km height in figure 6.10b)). In contrast, in the observations no such cloud top cooling is needed to form a thick and mixed-phase lower cloud (see yellow line between 0.5 km to 1.2 km height in figure 6.10b)). Further, in the observations an inversion of the equivalent potential temperature is visible at the lower cloud top (see yellow dash-dotted line in 1 km height

in figure 6.10b)). This inversion was neither captured in the standard run nor in the no upper cloud run. In this way it seems that the model has some difficulties of modelling a mixed-phase cloud in the stable Arctic boundary layer, even in the single layer case. Then, in the multilayer case, this problem becomes even more pronounced since the lower cloud experiences too much incoming longwave radiation from above.

Last but not least, we have to keep in mind that the simulated vertical velocity did not produce reasonable values in my model simulations. Having a correct upward vertical velocity could mean further cloud droplet activation and thereby less removal of LWP trough precipitation during the spin up of the standard run. If a correct vertical velocity would reduce the precipitation and thereby improve the modelled LWP and the lower cloud remains an open question.

7 Summary and conclusions

In this thesis I investigated the microphysical and radiative interaction of multilayer clouds. In the first part of this thesis I analysed if microphysical interaction of two clouds is possible. For this radiosounding and radar measurements of one year in Ny-Ålesund were used. First subsaturated layers embedded in between two supersaturated layers were analysed. Such subsaturated layers occur frequently, in 75% of the one-year dataset. Microphysical interaction of two supersaturated layers can then occur through seeding. Seeding means that an ice crystal can survive even if it sublimates when falling through the subsaturated layer. For the calculation of the sublimation in the subsaturated layers an initial ice crystal size of $r = 100\,\mu$m was chosen. Further all subsaturated layers thicker than 21.7 m and their measured atmospheric conditions were included. Seeding occurs more often than non-seeding. There was no seasonal trend in the one-year dataset, but in the 24.5-years dataset. In order to relate the high number of seeding and non-seeding cases to the actual multilayer cloud occurrence, the detection algorithm was extended by including radar measurements. For this the subsaturated layer and the two supersaturated layers were analysed regarding measured cloud signals of radar reflectivity factor. Here multilayer clouds occurred in 37% of the one-year dataset. The big discrepancy of only 37% multilayer clouds to 75% occurrence of subsaturated layers is mainly due to the high occurrence of supersaturation in non-cloudy environment. This is explained by the need of both supersaturation and sufficient *CCN* and *IN* for cloud activation in order to get cloud formation. The 37% multilayer clouds are composed of the occurrence of only seeding multilayer clouds in 25%, the occurrence of non-seeding multilayer clouds in 6% and the occurrence of multilayer clouds having both seeding and non-seeding layers in 6%. Among the seeding multilayer clouds (31%=25%+6%) it did not happen that the radar showed two cloud layers separated by clear interstice in between. Instead, these seeding multilayer clouds showed cloud detection in all three layers, the upper supersaturated layer, the subsaturated layer and the lower supersaturated layer. Among the non-seeding multilayer clouds (12%=6%+6%) in 14% the radar showed two cloud layers separated by clear interstice in between. Radar cloud detection in all three layers did occur 7%. In literature the term multilayer cloud is used both in connection with clear interstice in between two cloud layers and as layers inside a cloud of larger extend (Intrieri et al., 2002b; Liu et al., 2012; Khvorostyanov et al., 2001; Verlinde et al., 2007). I showed that multilayer cloud interaction through seeding is possible. Though, given that there is seeding, then this goes in hand with a continuous cloud radar signal. This means that a seeding multilayer cloud can not be defined by a clear visible interstice but is rather continuous, similar to the one described by Verlinde et al. (2007). The classification showed a weak seasonal trend regarding multilayer cloud occurrence. There was a slight increase during autumn and spring. However, mainly due to the too short time of study, the validity of this has to be questioned. Finally, the classification was evaluated by a very simple visual detection leading to 22% multilayer cloud occurrence. These 22% multilayer clouds had all a clear interstice. Therefore,

taking the result of the classification into account, they were assumed to be non-seeding. This caused a discrepancy to 12% non-seeding multilayer clouds derived by my classification. Wind transporting the radiosounding away from the radar, the averaging of the originally continuous radar images and the chosen ice crystal size did all have large impacts on the classification and this discrepancy.
In the second part of this thesis the focus was on the radiative interaction of non-seeding multilayer clouds. For this semi-idealized COSMO simulations of a multilayer cloud case observed during the ASCOS field campaign are used. The model was able to simulate a multilayer cloud structure. The upper cloud was a mixed-phase cloud and in good agreement with the observations. The lower cloud was not in that good agreement to the observations. The modelled cloud was too thin and only liquid, but in the observations thicker and more ice containing. On the same time the liquid water path was much too low in the model. Dealing with the radiative interaction of multilayer clouds, it is irrelevant if the multilayer cloud occurs in summer or winter. This is due to the shortwave heating in Arctic summer being one order of magnitude smaller than the longwave cooling. Thereby the pronounced seasonal cycle of shortwave radiation in the Arctic can be excluded as a reason for the possible seasonal trend in multilayer cloud occurrence. The model was able to show the main impacts multilayer clouds have on each other. The upper cloud is not influenced by the lower cloud. Since the upper cloud is a typical Arctic mixed-phase cloud, it is primary controlled by cloud top cooling generating in-cloud mixing. The boundary layer below is often, under Arctic conditions with sea ice, stable stratified. Thereby the influence of a cloud inside this stable boundary layer on the upper cloud is unlikely. In more southerly latitudes mixing in the vertical is much more likely due to convection. Taking this into account, it seems reasonable that the Arctic multilayer cloud occurrence of 37% is much higher than 11% globally (Christensen et al., 2013). The lower cloud is influenced by the upper cloud. Without any upper cloud the lower cloud is thicker and shows cloud top cooling, in-cloud mixing and the generation of ice. In contrast, in the existence of an upper cloud the lower cloud was thinner and liquid only. It is shielded from cloud top cooling and the in-cloud mixing is reduced. Even if the distance between multilayer clouds is wide and seeding is not possible, then the multilayer clouds still interact through longwave radiation.

7.1 Outlook

The aim of this thesis was to understand the interaction processes that are relevant for multilayer clouds. I found that microphysical interaction is possible through seeding in 31% of the investigated cases. If so, then this becomes visible in the radar image by a continuous cloud signal. Validating this cloud signal in the subsaturated layer is challenging. The signal could either be due to falling ice crystals, but also due to the existence of cloud liquid and small ice crystals not big enough to fall. In this way, the validation of seeding multilayer cloud occurrence needs further research. Given that an ice crystal reaches into the lower cloud layer, then the following microphysical interaction could be the ice crystal growing further. This would be due to the Bergeron-Wegener-Findeisen process and could cause in-cloud clearings. In my classification no cloud below occurred in less than <2% of the seeding cases. In this way the effects inside the lower cloud layer remains an open question.

Also non-seeding multilayer clouds are not in all details fully understood yet. First of all the discrepancy of the visual detection to my classification should be evaluated further, e.g. by using a skill score table, to review the assumptions used. For the non-seeding multilayer clouds the radiative influence is given by a reduced lower cloud. In the observations the lower cloud almost dissipated when having an upper cloud in a warmer temperature range. I would expect the influence of the upper cloud on the lower cloud to increase when the upper cloud is thicker and warmer. In the modelling study this was not the case. Increasing the liquid in the upper cloud did not show any effect on the lower cloud. An explanation to this could be the threshold limiting the effect of liquid on the emissivity of the upper cloud. Above this threshold the upper cloud emits as a black body and thereby only in dependence on temperature. However, in the model the increased temperature in the upper cloud did not influence the lower cloud. An explanation to this could be the assumptions done in the radiation scheme of the model. A suggestion would be to investigate how the calculation of mean temperature and mean cloud liquid for the emissivity of the cloud layer is done. Further, it should be investigated how this cloud emissivity affects multilayer clouds, given that there is a clear interstice in between. Finally, since the model showed overall larger problems simulating the lower cloud than the upper cloud, this raises the question if the trouble is also due to the existence of the lower cloud in stable stratification.

A Appendix

A.1 Radiosounding and radar

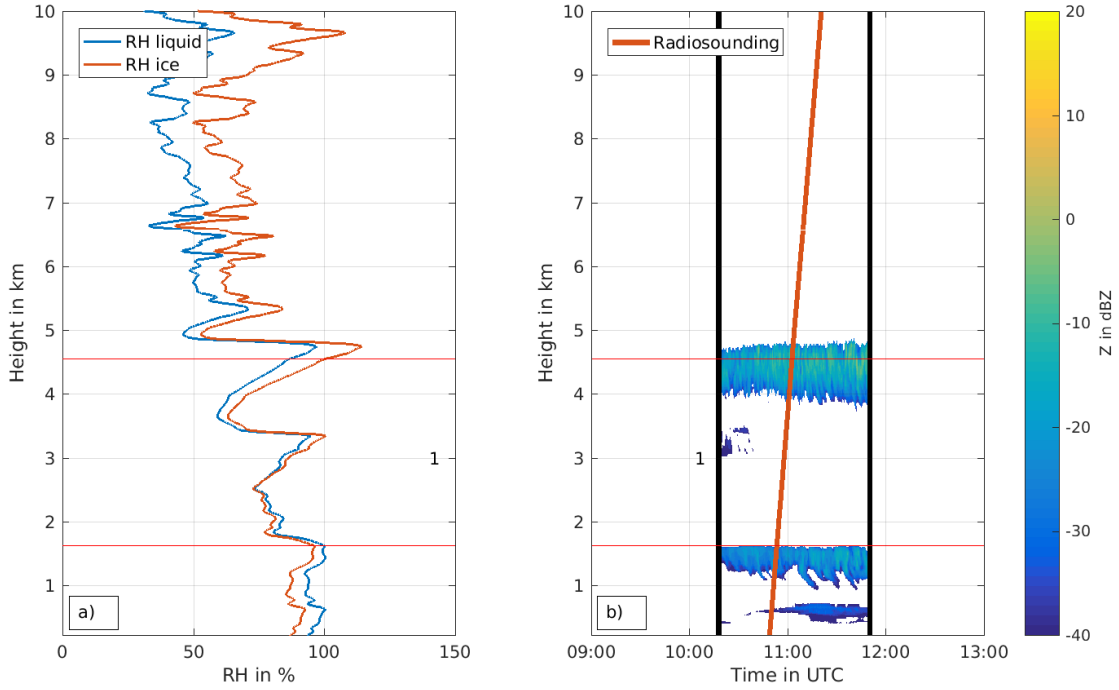

Figure A.1: 16 July 2016: a) Relative humidity with respect to water in blue and relative humidity with respect to ice in red and b) radar reflectivity factor. The subsaturated layer between approx 0.6 km to 1.3 km height was not considered further. The supersaturated layers at approx 3.3 km height and at approx 9.6 km height were not considered further. The red horizontal lines and the number 1 visualise the subsaturated layer.

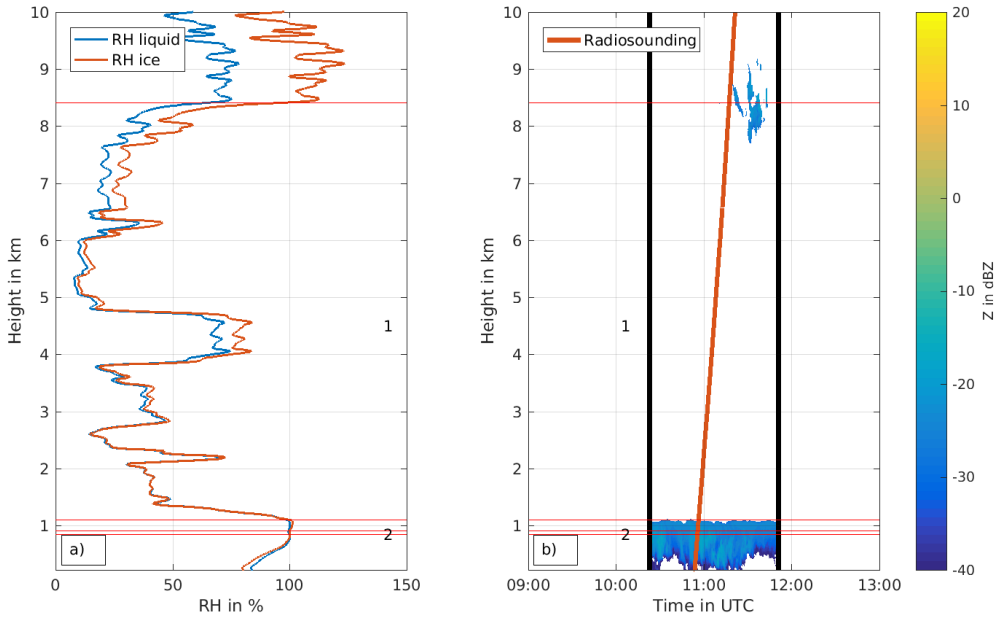

Figure A.2: 27 July 2016: a) Relative humidity with respect to water in blue and relative humidity with respect to ice in red and b) radar reflectivity factor. The subsaturated layers at approx 9.5 km height and at approx 9.6 km height were not considered further. The subsaturated layer at approx 9.5 km height was the one with maximum thickness of approx. 21.7 m and that one was not considered further. The red horizontal lines and the numbers 1 and 2 visualise the subsaturated layers.

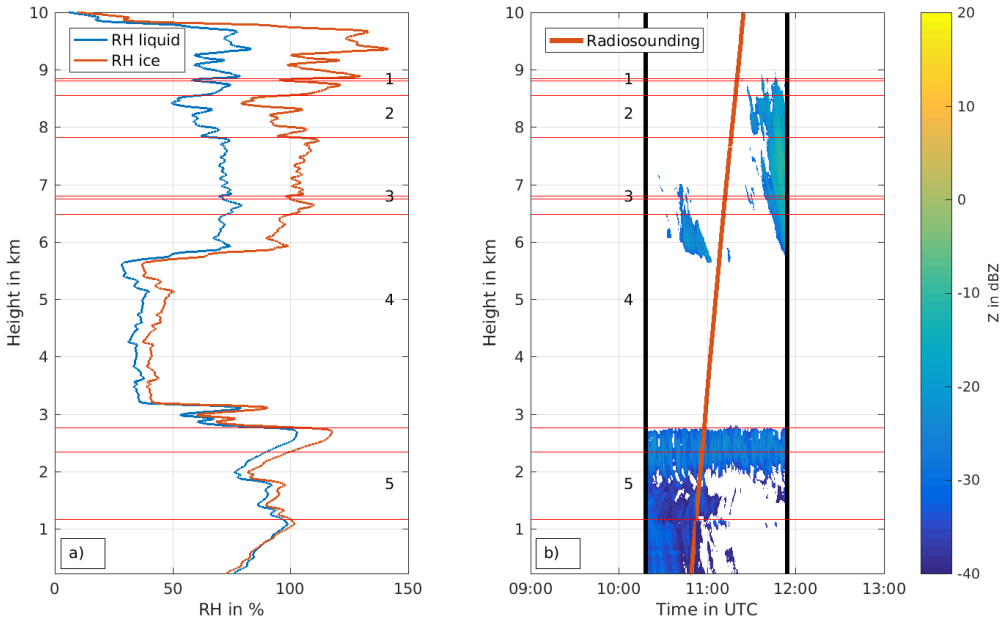

Figure A.3: 13 August 2016: a) Relative humidity with respect to water in blue and relative humidity with respect to ice in red and b) radar reflectivity factor. The subsaturated layer at approx 9.1 km height was not considered further. Thin subsaturated layers such as at 8.8 km height were considered further. Thin supersaturations at 8.4 km and 8.0 km were not considered further. The red horizontal lines and the numbers 1, 2, 3, 4 and 5 visualise the subsaturated layers.

A.2 Sublimation calculations

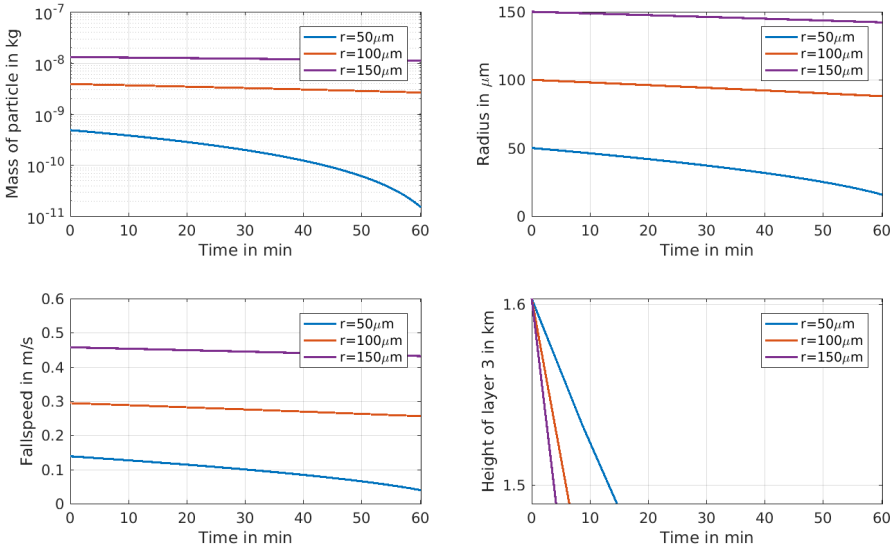

Figure A.4: Sublimation calculation for the subsaturated layer between 1.60 km and 1.49 km height (layer 3 in figure 4.3) at 3 November 2016. Average values were pressure $p = 844.70$ hPa, temperature $T = -7.74\,^{\circ}$C and relative humidity with respect to ice $RH_i = 98.83\,\%$. Different sizes at begin are $r = 50\,\mu$m, $100\,\mu$m and $150\,\mu$m. The height pot shows only the height level of the subsaturated layer between 1.60 km and 1.49 km. All ice crystals reach the lower supersaturated layer.

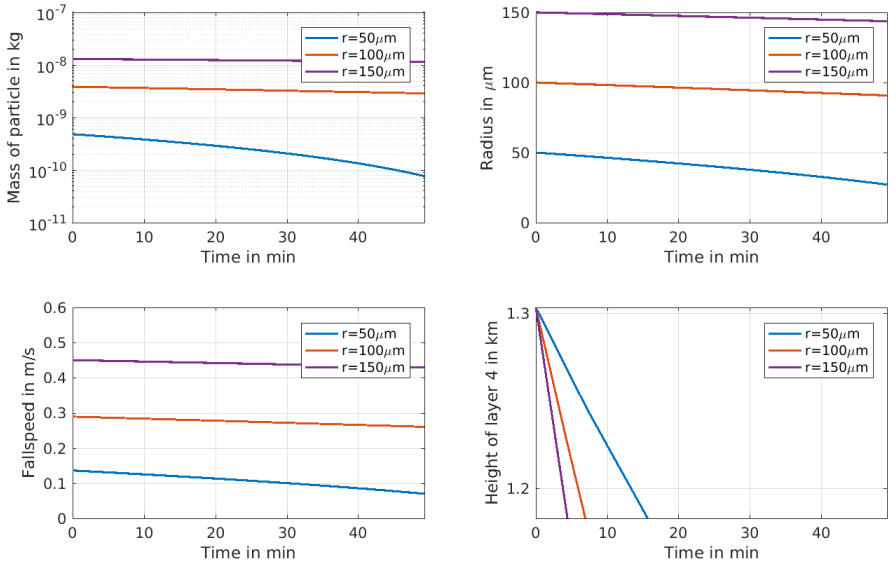

Figure A.5: Sublimation calculation for the subsaturated layer between 1.3 km and 1.18 km height (layer 4 in figure 4.3) at 3 November 2016. Average values were pressure $p = 878.19$ hPa, temperature $T = -5.90\,^{\circ}$C and relative humidity with respect to ice $RH_i = 98.97\,\%$. Different sizes at begin are $r = 50\,\mu$m, $100\,\mu$m and $150\,\mu$m. The time axis reaches until the $r = 150\,\mu$m ice crystal has reached the ground. The height axis shows the total height of the subsaturated layer between 1.3 km and 1.18 km. All ice crystals reach the lower supersaturated layer.

A.3 Results of the detection algorithm using only radiosoundings

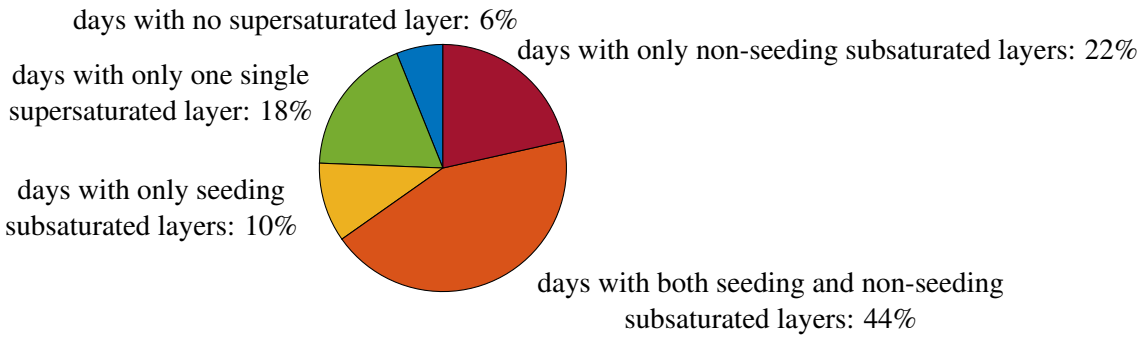

Figure A.6: Relative distribution of days of different cloud occurrence between 10 June 2016 - 9 June 2017. 100% equals 278 days. Seeding and non-seeding is calculated using an ice crystal of the size $r = 50\,\mu$m.

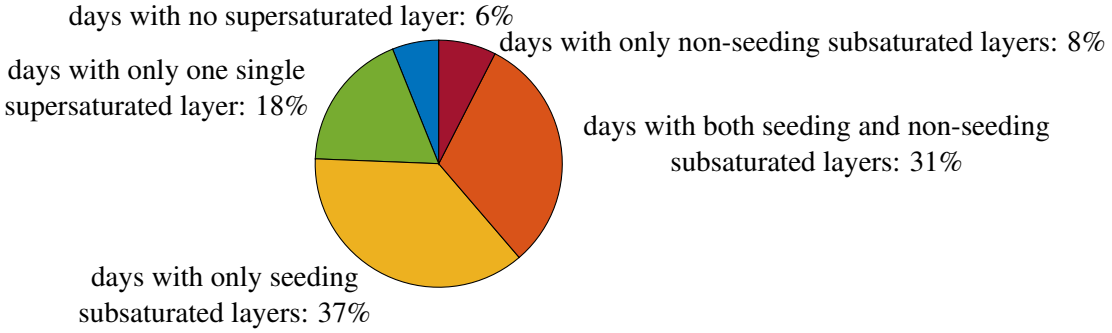

Figure A.7: Relative distribution of days between 10 June 2016 - 9 June 2017. 100% equals 278 days. Seeding and non-seeding is calculated using an ice crystal of the size $r = 150\,\mu$m.

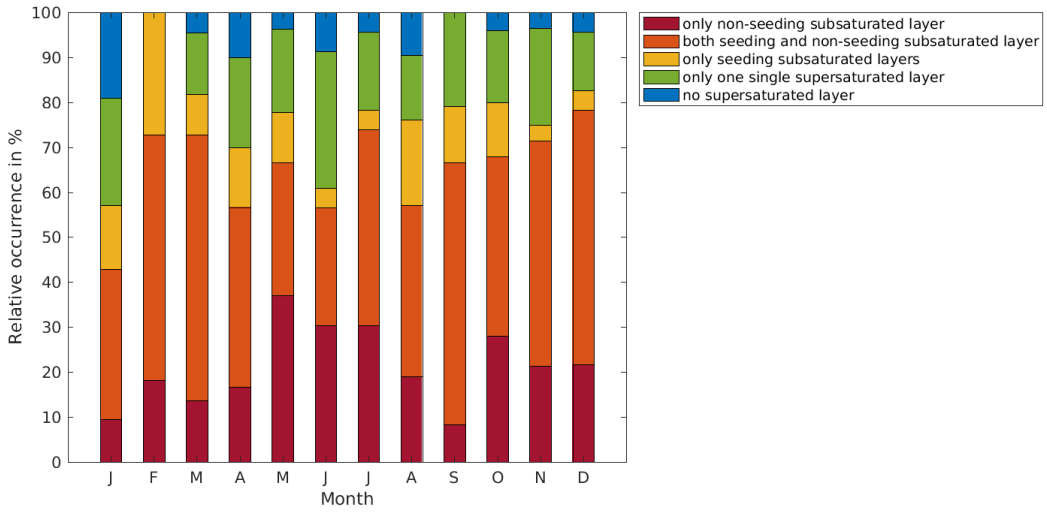

Figure A.8: Temporal distribution of days of different cloud occurrence between 10 June 2016 - 9 June 2017. Seeding and non-seeding is calculated using an ice crystal of the size $r = 50\,\mu$m.

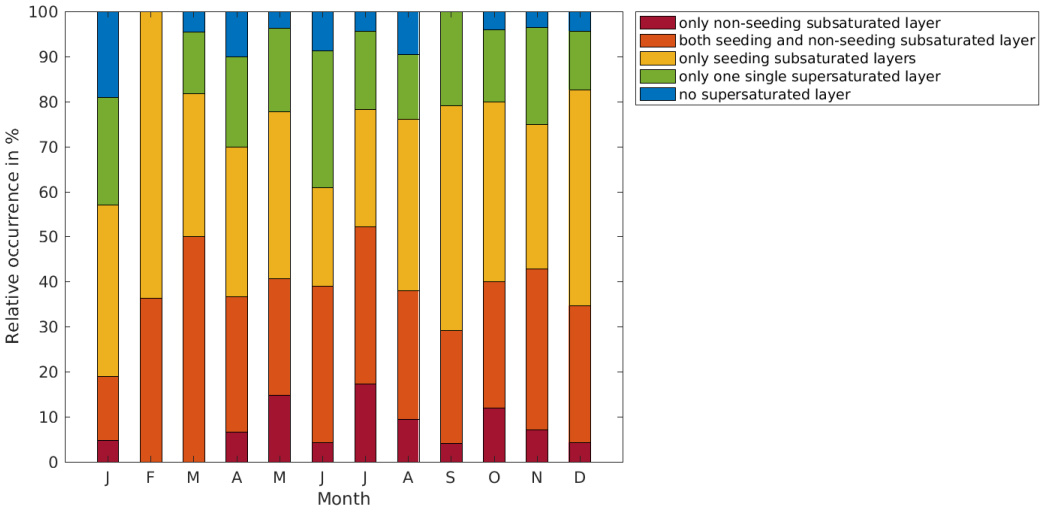

Figure A.9: Temporal distribution of days between 10 June 2016 - 9 June 2017. Seeding and non-seeding is calculated using an ice crystal of the size $r = 150\,\mu$m.

A.4 Results of the detection algorithm upgraded by radar

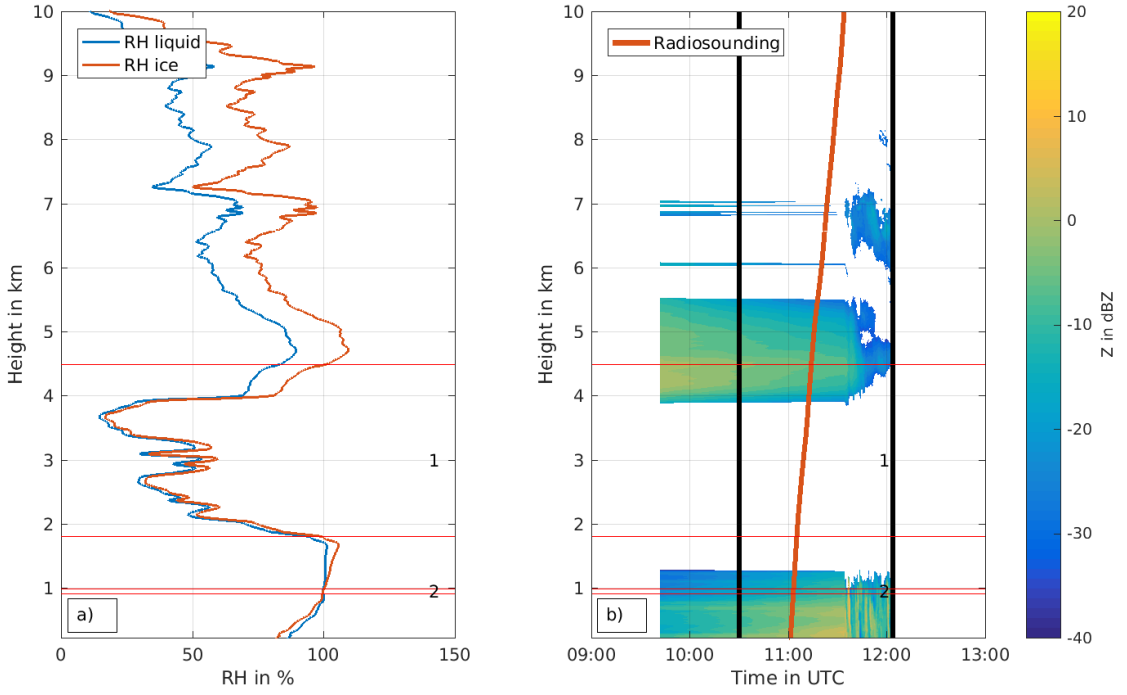

Figure A.10: 10 October 2016: a) Relative humidity with respect to water in blue and relative humidity with respect to ice in red and b) radar reflectivity factor. The measurement error becomes visible as constant measured radar reflectivity factor. The red horizontal lines and the numbers 1 and 2 visualise the subsaturated layers.

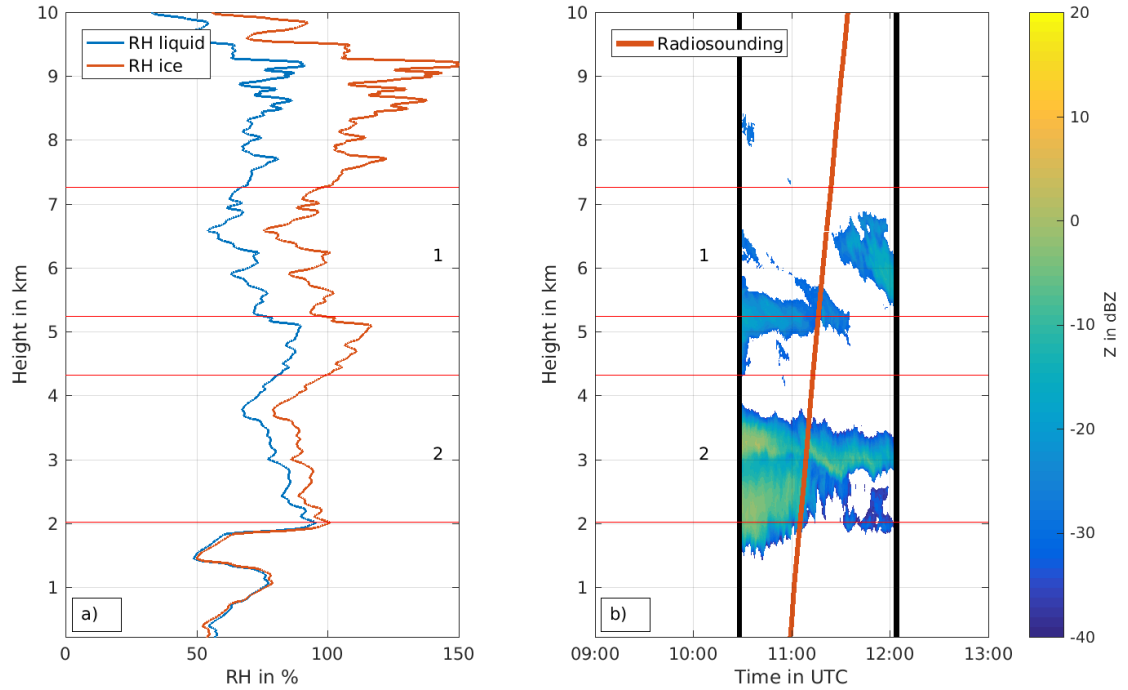

Figure A.11: 27 October 2016: a) Relative humidity with respect to water in blue and relative humidity with respect to ice in red and b) radar reflectivity factor. The supersaturated layer between 4.2 km and 5.2 km height was considered as no cloud as supersaturated layer above the subsaturated layer (layer 2) between 2.0 km and 4.2 km. The same supersaturated layer was considered as cloud when evaluated as supersaturated layer below the subsaturated layer (layer 2) between 5.2 km and 7.2 km. The red horizontal lines and the numbers 1 and 2 visualise the subsaturated layers.

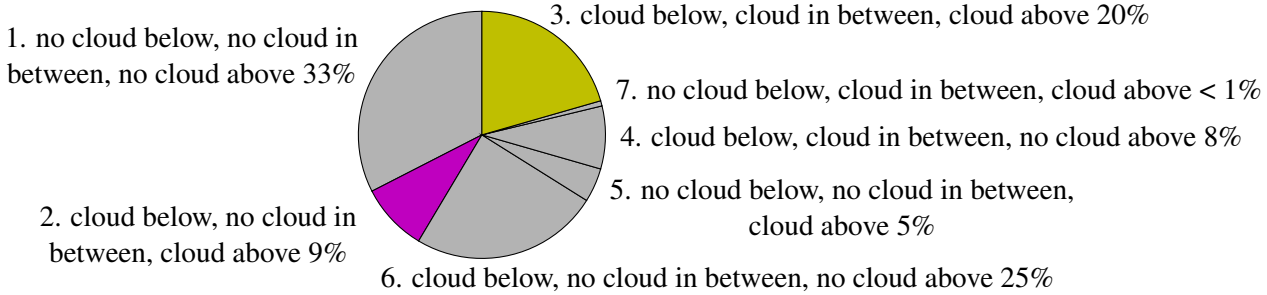

Figure A.12: Non-seeding: Subcategories of all non-seeding subsaturated layers. In between refers to the subsaturated layer. Below and above refers to the supersaturated layers just next to the subsaturated layer. 100% equals all non-seeding subsaturated layers. Non-seeding is calculated using an ice crystal of the size $r = 50\,\mu$m.

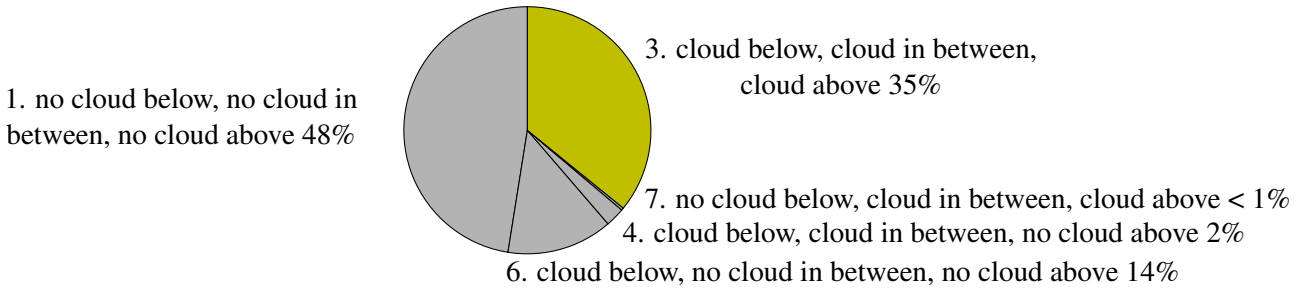

Figure A.13: Seeding: Subcategories of all seeding subsaturated layers. In between refers to the subsaturated layer. Below and above refers to the supersaturated layers just next to the subsaturated layer. 100% equals all seeding subsaturated layers. Seeding is calculated using an ice crystal of the size $r = 50\,\mu$m.

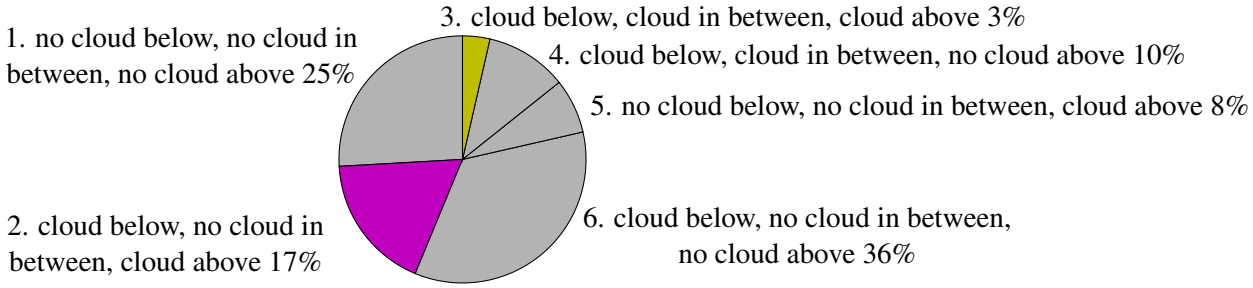

Figure A.14: Non-seeding: Subcategories of all non-seeding subsaturated layers. In between refers to the subsaturated layer. Below and above refers to the supersaturated layers just next to the subsaturated layer. 100% equals all non-seeding subsaturated layers. Non-seeding is calculated using an ice crystal of the size $r = 150\,\mu$m.

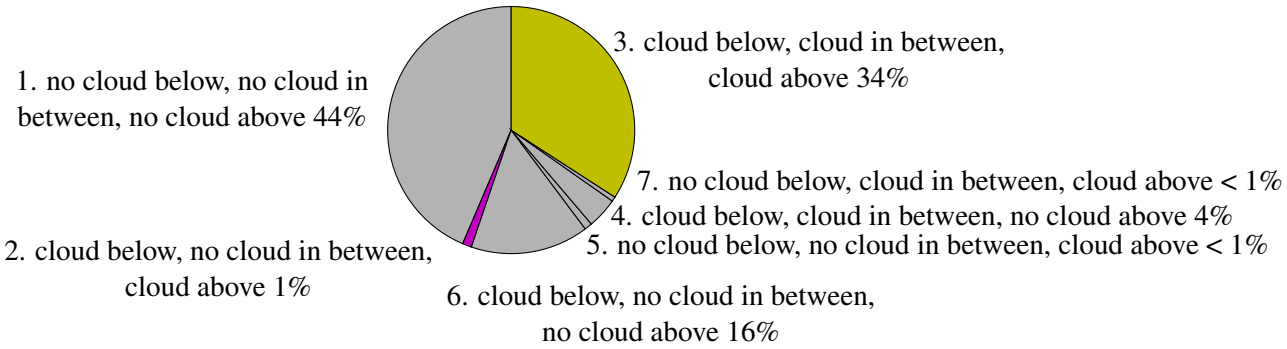

Figure A.15: Seeding: Subcategories of all seeding subsaturated layers. In between refers to the subsaturated layer. Below and above refers to the supersaturated layers just next to the subsaturated layer. 100% equals all seeding subsaturated layers. Seeding is calculated using an ice crystal of the size $r = 150\,\mu$m.

A.5 Detection algorithm using both radiosounding and radar

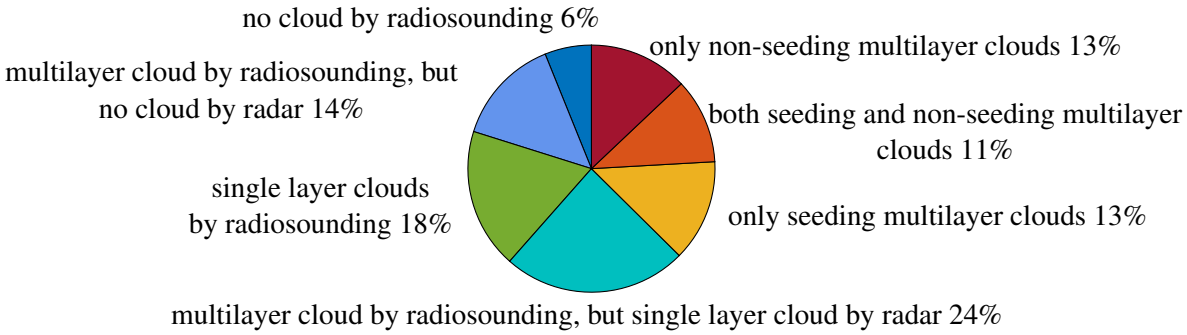

Figure A.16: Cloud occurrence derived from using both radiosounding and radar for detection. 100% equals 278 days between 10 June 2016 - 9 June 2017. Seeding and non-seeding is calculated using an ice crystal of the size $r = 50\,\mu$m.

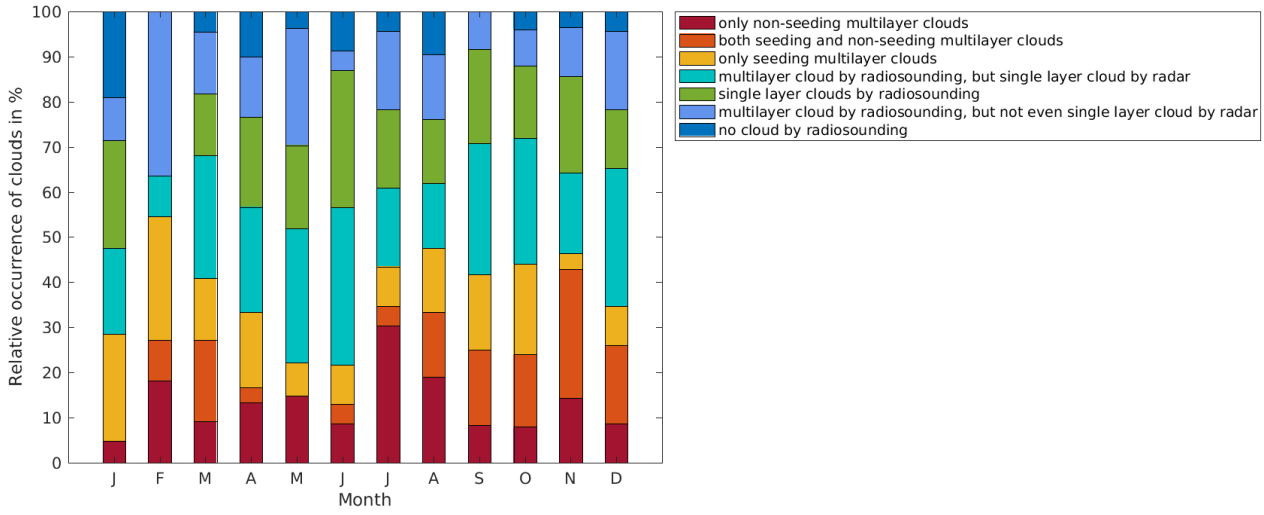

Figure A.17: Temporal distribution of cloud occurrence using both radiosounding and radar. Seeding and non-seeding is calculated using an ice crystal of the size $r = 50\,\mu$m.

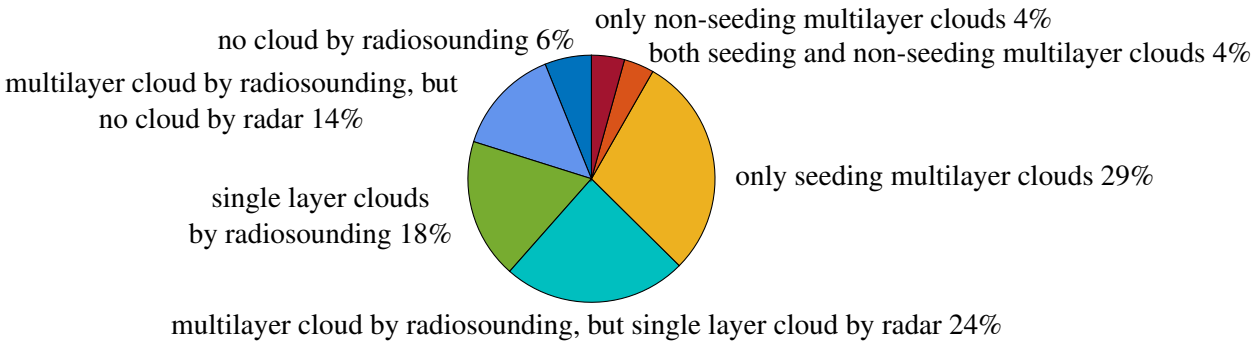

Figure A.18: Cloud occurrence derived from using both radiosounding and radar for detection. 100% equals 278 days between 10 June 2016 - 9 June 2017. Seeding and non-seeding is calculated using an ice cystal of the size $r = 150\,\mu$m.

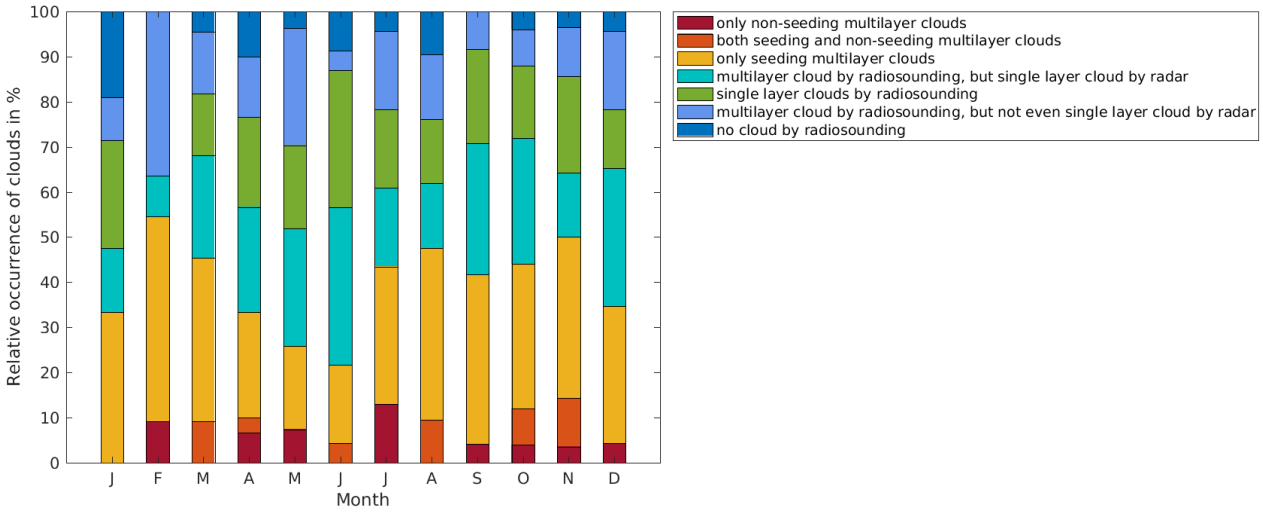

Figure A.19: Temporal distribution of cloud occurrence using both radiosounding and radar. Seeding and non-seeding is calculated using an ice cystal of the size $r = 150\,\mu$m.

A.6 Limitations and evaluation of classification

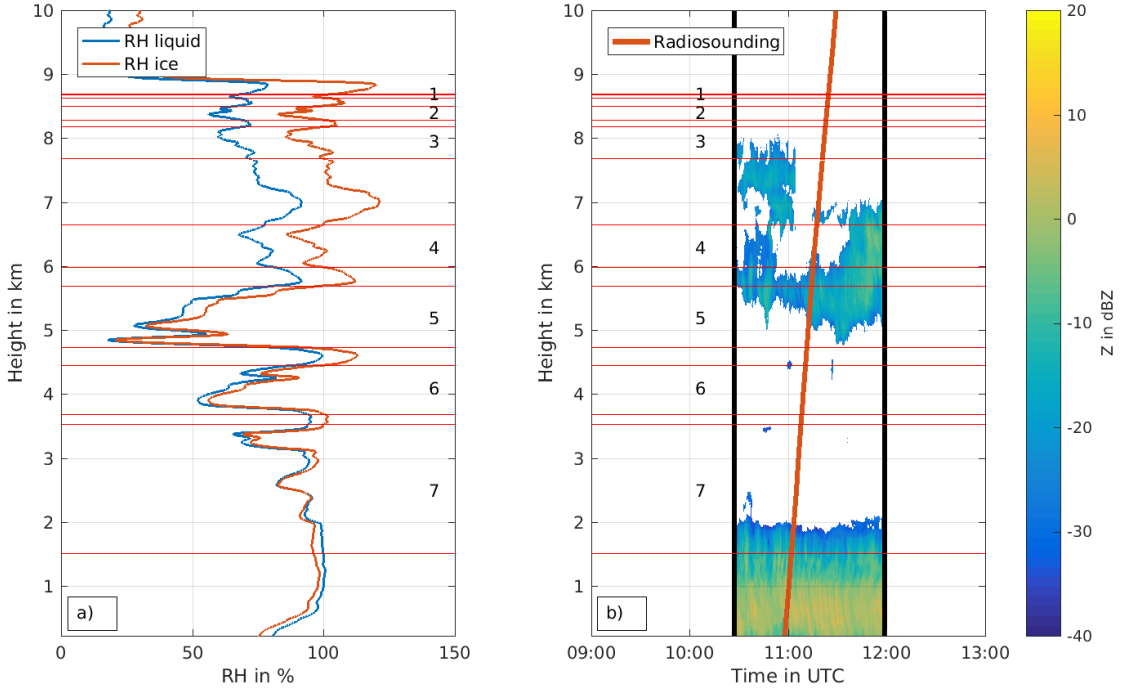

Figure A.20: 17 August 2016: a) Relative humidity with respect to water in blue and relative humidity with respect to ice in red and b) radar reflectivity factor. The supersaturated layer at 1.7 km is limited by the $RH_i = 100\%$ threshold. The radar shows a cloud top at 2.0 km. The red horizontal lines and the numbers 1, 2, 3, 4, 5, 6 and 7 visualise the subsaturated layers.

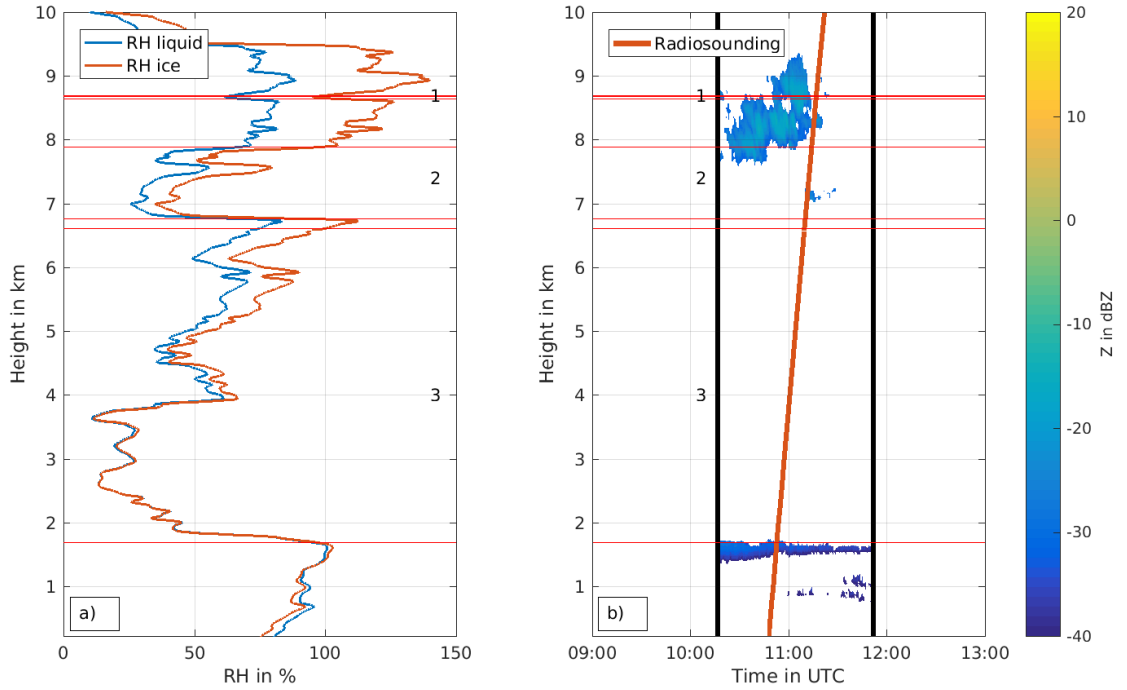

Figure A.21: 30 June 2016: a) Relative humidity with respect to water in blue and relative humidity with respect to ice in red and b) radar reflectivity factor. The supersaturated layer at 1.6 km is 250 m thick. At the same height the radar shows a cloud layer. The red horizontal lines and the numbers 1, 2 and 3 visualise the subsaturated layers.

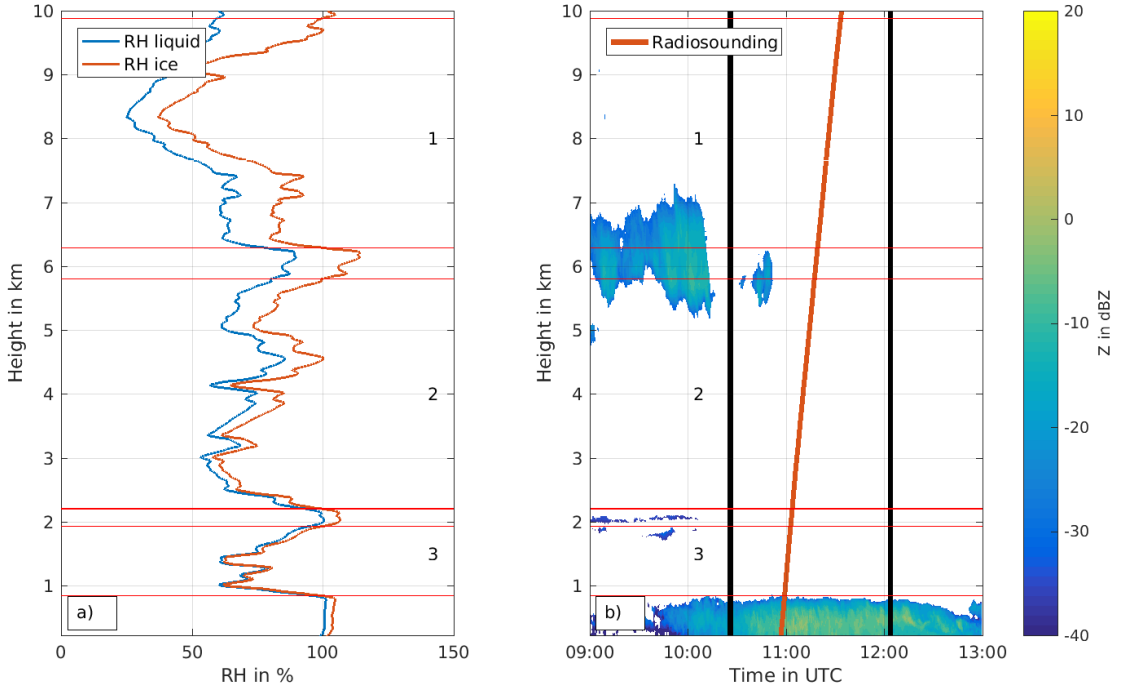

Figure A.22: 22 October 2016: a) Relative humidity with respect to water in blue and relative humidity with respect to ice in red and b) radar reflectivity factor. For the supersaturated layer at 6 km cloud dissipation occurred before the radiosounding was launched. The red horizontal lines and the numbers 1, 2 and 3 visualise the subsaturated layers.

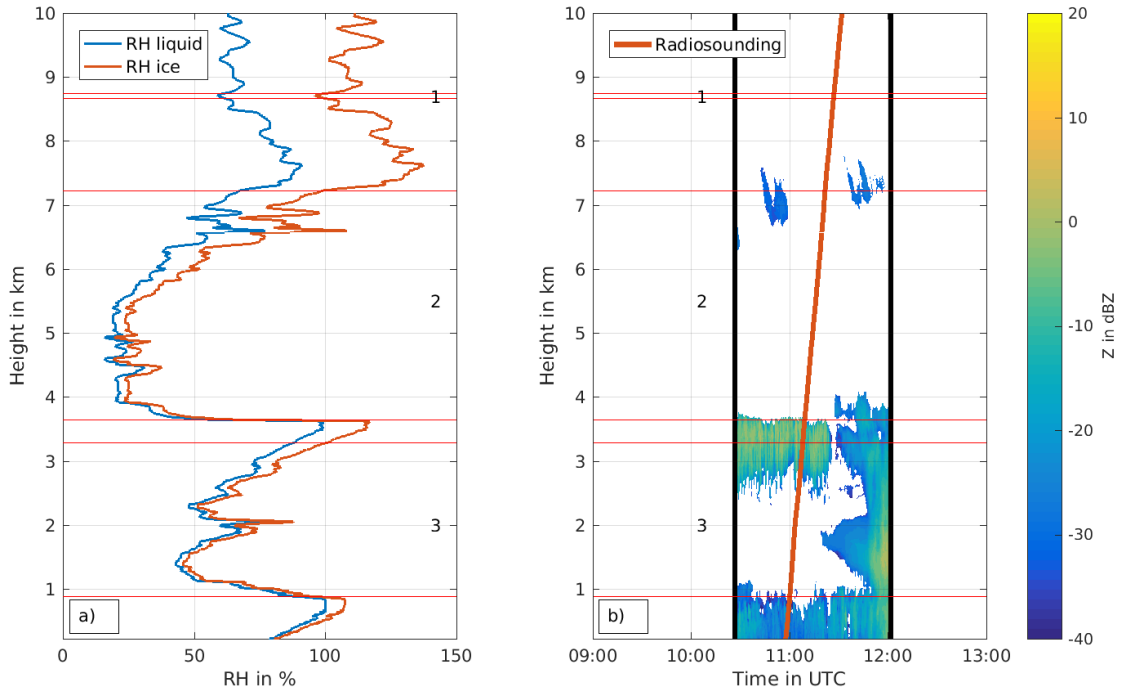

Figure A.23: 28 April 2017: a) Relative humidity with respect to water in blue and relative humidity with respect to ice in red and b) radar reflectivity factor. The subsaturated layer 3 (between 0.9 km and 3.2 km was categorized as non-seeding and subcategory 3. (cloud below, cloud in between, cloud above).

A.7 Visual evaluation

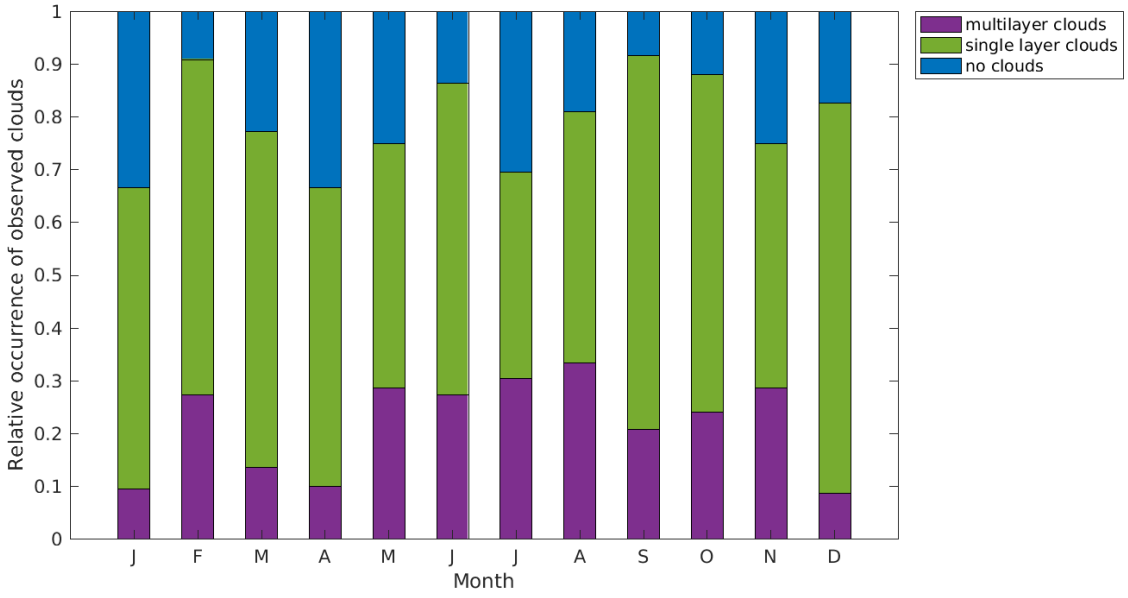

Figure A.24: Temporal distribution of days by visual detection. Data between 10 June 2016 - 9 June 2017.

A.8 ASCOS Surface pressure chart

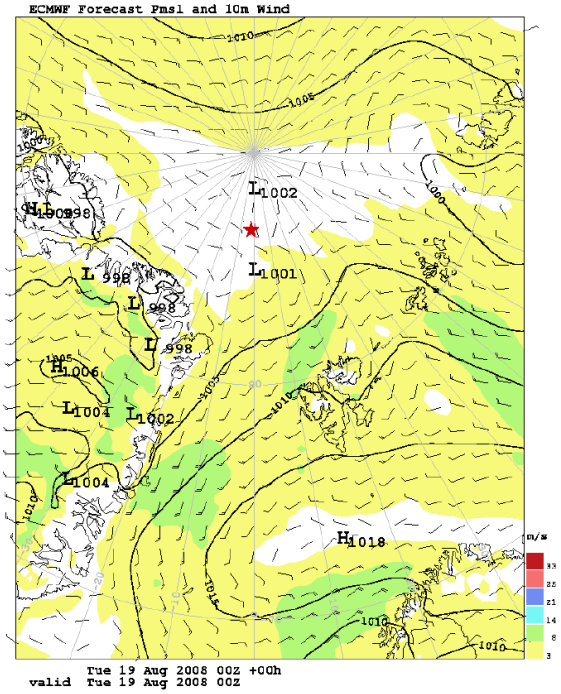

Figure A.25: ECMWF map of surface pressure and 10 m wind. The position of ASCOS is indicated by a red star (ASCOS Data, 2009).

A.9 COSMO standard run

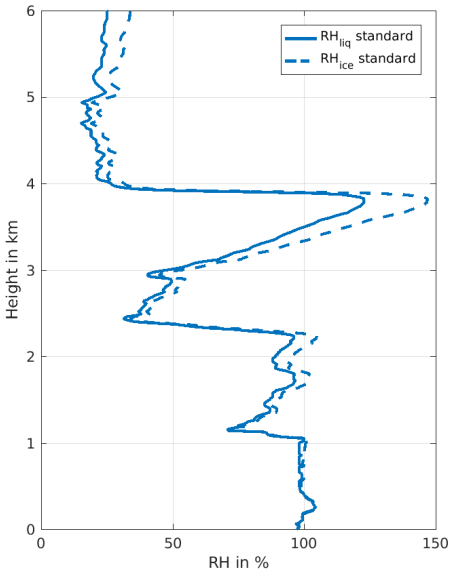

Figure A.26: Standard run: Relative humidity with respect to water R_{liq} and regarding ice R_{ice} as input for the standard run with COSMO. *LWC* and *IWC* were added to the original relative humidity shown in figure 5.2b.

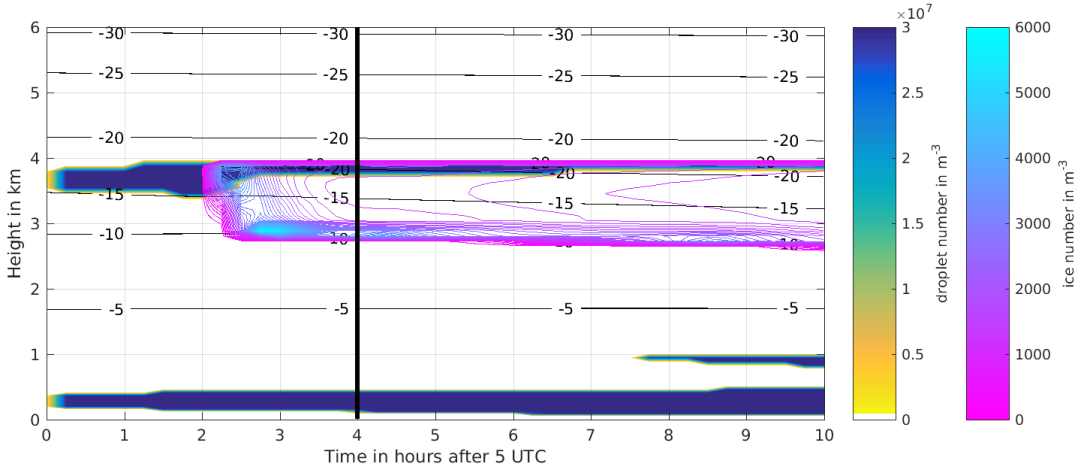

Figure A.27: Standard run: Cloud droplet number and cloud ice number. Cloud droplet number was prescribed as constant $QNC = 30 \times 10^6\,\mathrm{m}^{-3}$. The time of finished spin-up is indicated by the solid black line.

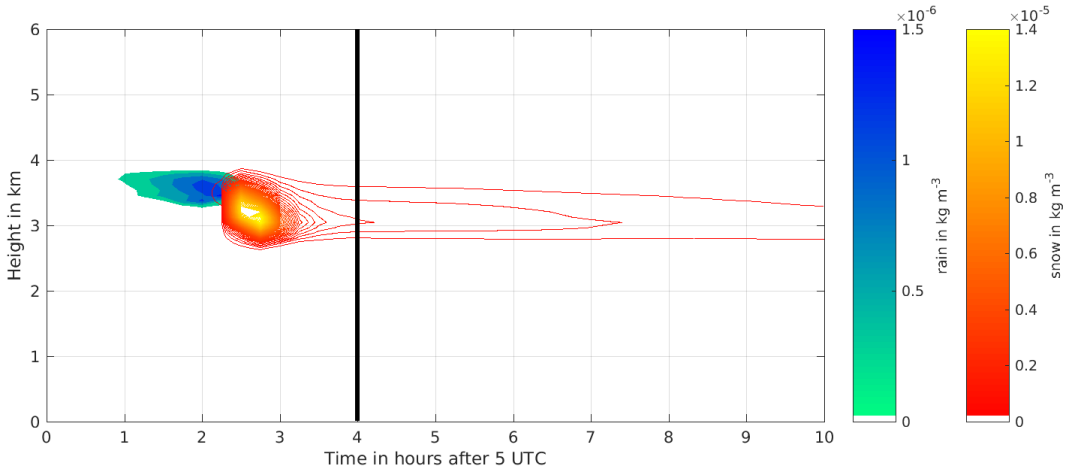

Figure A.28: Standard run: Rain and snow amount. The time of finished spin-up is indicated by the solid black line.

A.10 COSMO no shortwave run

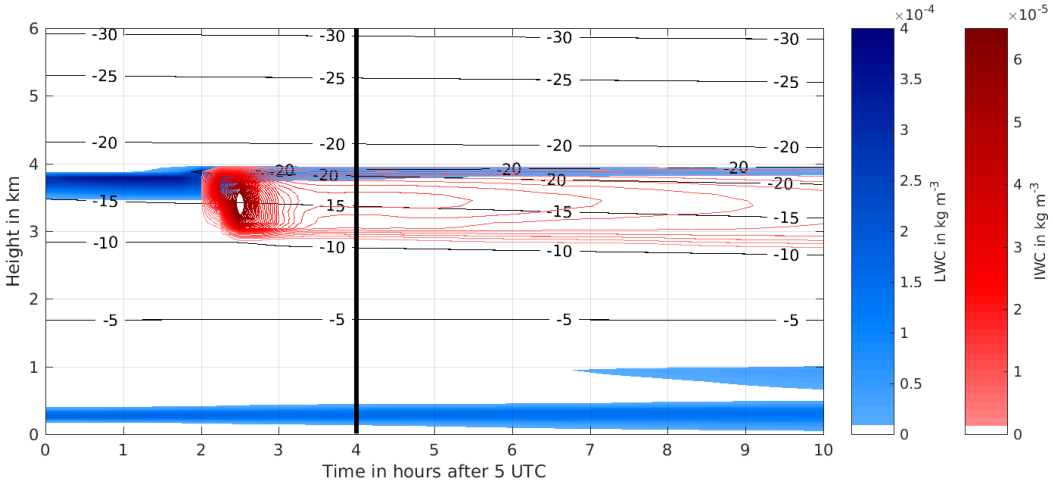

Figure A.29: No shortwave run: Cloud liquid water content (*LWC*) in blue and cloud ice content (*IWC*) in red. This no shortwave run is the standard run, but on 19 December 2008 instead of 19 August 2008. The time of finished spin-up is indicated by the solid black line. Thin black lines indicate the temperatures in °C.

A.11 COSMO no upper cloud run

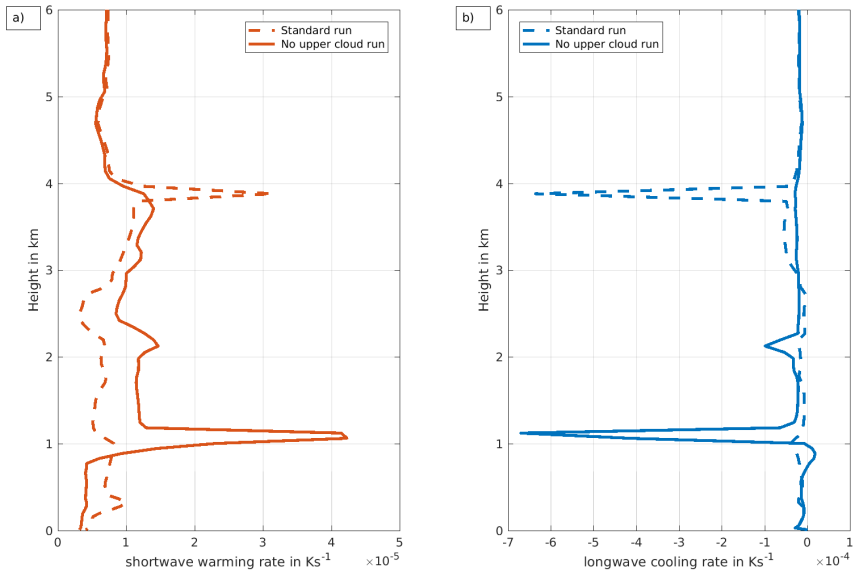

Figure A.30: No upper cloud: a) Shortwave warming and b) longwave cooling rate. Negative values means cooling, positive values means warming. Solid lines are used for the no upper cloud run, dash-dotted lines are used for the standard run (see also figure 6.2). For the averaging only the time after finished spin-up is used.

A.12 COSMO low upper cloud run

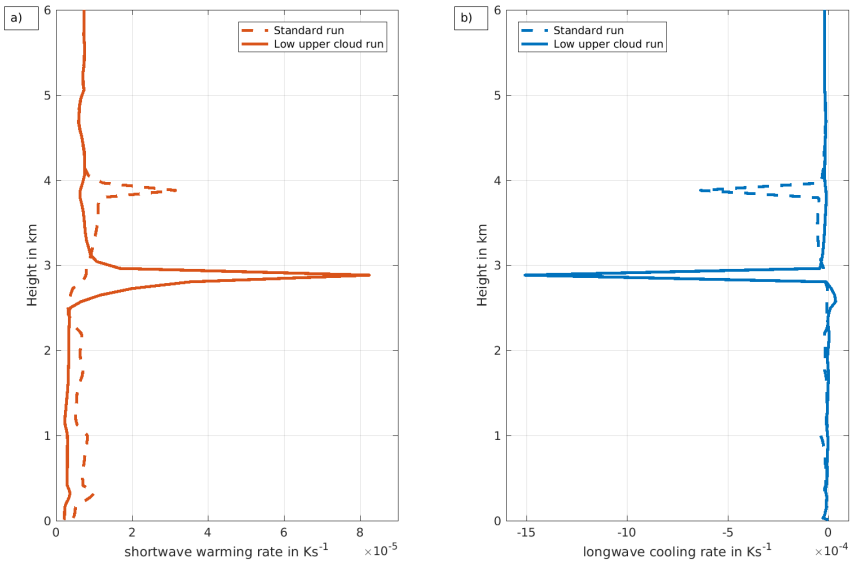

Figure A.31: Low upper cloud: a) Shortwave warming and b) longwave cooling rate. Negative values means cooling, positive values means warming. Solid lines are used for the no upper cloud run, dash-dotted lines are used for the standard run (see also figure 6.2). For the averaging only the time after finished spin-up is used.

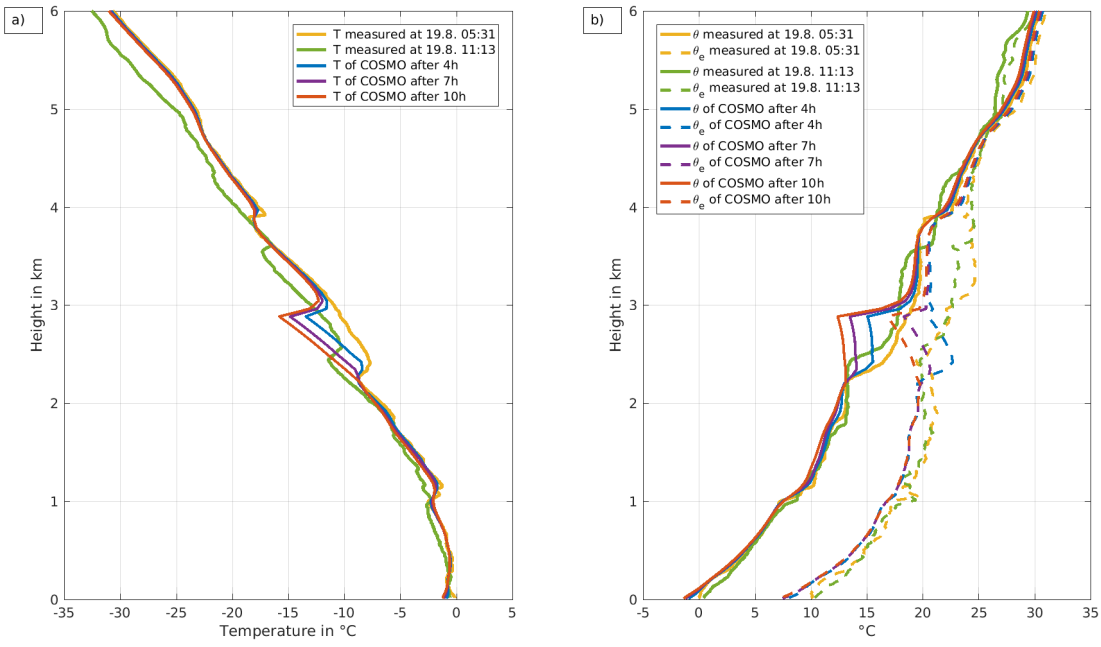

Figure A.32: Low upper cloud: a) Temperature height profiles and b) Potential temperature height profile. The measured profiles are taken from ASCOS observations (ASCOS Data, 2009). The COSMO height profiles are modelled.

Bibliography

C. Andronache. *Mixed-Phase Clouds*. Elsevier, 2018.

AROME-Arctic. Webpage, 2015. URL `https://www.met.no/en/projects/The-weather-model-AROME-Arctic`. Last visited 2018-02-07.

ASCOS Data. Data base, 2009. URL `http://www.ascos.se/index.php?q=data`. Last visited 2018-01-15.

A. Barrett, R. Hogan, and R. Forbes. *Why Can't Models Simulate Mixed-phase Clouds Correctly?* PhD thesis, University of Reading, 2012.

J. Bühl, P. Seifert, A. Myagkov, and A. Ansmann. Measuring ice-and liquid-water properties in mixed-phase cloud layers at the Leipzig Cloudnet station. *Atmospheric Chemistry and Physics*, 16(16):10609–10620, 2016.

M. W. Christensen, G. G. Carrió, G. L. Stephens, and W. R. Cotton. Radiative impacts of free-tropospheric clouds on the properties of marine stratocumulus. *Journal of the Atmospheric Sciences*, 70(10):3102–3118, 2013.

Cloudnet. See acknowledgements, but also:. URL `http://gop.meteo.uni-koeln.de/~Hatpro/dataBrowser/dataBrowser1.html?site=Ny-Alesund&date=2016-06-10&UpperLeft=Joyrad94_CN-Classification`. Last visited 2017-05-15.

J. A. Curry and E. E. Ebert. Annual cycle of radiation fluxes over the Arctic Ocean: Sensitivity to cloud optical properties. *Journal of Climate*, 5(11):1267–1280, 1992.

J. A. Curry, J. L. Schramm, W. B. Rossow, and D. Randall. Overview of Arctic cloud and radiation characteristics. *Journal of Climate*, 9(8):1731–1764, 1996.

G. Doms and M. Baldauf. Description of the Nonhydrostatic Regional COSMO Model, Part I: Dynamics and Numerics, 2015.

G. Doms, J. Forstner, E. Heise, H.-J. Herzog, D. Mironov, M. Raschendorfer, T. Reinhardt, B. Ritter, R. Schrodin, J.-P. Schulz, and G. Vogel. Description of the Nonhydrostatic Regional COSMO Model, Part II: Physical Parametrization, 2011.

ECMWF. Webpage, 2017. URL `https://www.ecmwf.int/en/faq/how-are-low-medium-and-high-cloud-cover-defined`. Last visited 2017-03-12.

N. Fletcher. The Physics of Rainclouds, 1962.

E. J. Førland, R. Benestad, I. Hanssen-Bauer, J. E. Haugen, and T. E. Skaugen. Temperature and precipitation development at Svalbard 1900–2100. *Advances in Meteorology*, 2011, 2011.

R. A. Frey, S. A. Ackerman, Y. Liu, K. I. Strabala, H. Zhang, J. R. Key, and X. Wang. Cloud detection with MODIS. Part I: Improvements in the MODIS cloud mask for collection 5. *Journal of Atmospheric and Oceanic Technology*, 25(7):1057–1072, 2008.

K. Gierens and P. Spichtinger. On the size distribution of ice-supersaturated regions in the upper troposphere and lowermost stratosphere. In *Annales Geophysicae*, volume 18, pages 499–504. Springer, 2000.

Gruan. Data provided by Marion Maturilli, Alfred Wegner Insitute, 2017. URL `https://www.gruan.org/data/file-archive/`. Last visited 2017-05-15.

P. S. Guest and K. L. Davidson. The aerodynamic roughness of different types of sea ice. *Journal of Geophysical Research: Oceans*, 96(C3):4709–4721, 1991.

W. Hall and H. Pruppacher. The survival of ice particles falling from cirrus clouds in subsaturated air. *Journal of the Atmospheric Sciences*, 33(10):1995–2006, 1976.

J. Y. Harrington, M. P. Meyers, R. L. Walko, and W. R. Cotton. Parameterization of ice crystal conversion processes due to vapor deposition for mesoscale models using double-moment basis functions. Part I: Basic formulation and parcel model results. *Journal of the atmospheric sciences*, 52(23):4344–4366, 1995.

G. Herman and R. Goody. Formation and persistence of summertime Arctic stratus clouds. *Journal of the Atmospheric Sciences*, 33(8):1537–1553, 1976.

A. Holtslag, G. Svensson, P. Baas, S. Basu, B. Beare, A. Beljaars, F. Bosveld, J. Cuxart, J. Lindvall, G. Steeneveld, et al. Stable atmospheric boundary layers and diurnal cycles: challenges for weather and climate models. *Bulletin of the American Meteorological Society*, 94(11):1691–1706, 2013.

R. A. Houze Jr. *Cloud dynamics*, volume 53. Academic press, 1993.

P. J. Huffman and G. Vali. The effect of vapor depletion on ice nucleus measurements with membrane filters. *Journal of Applied Meteorology*, 12(6):1018–1024, 1973.

R. E. Huschke. Arctic cloud statistics from 'air-calibrated' surface weather observations. Technical report, 1969.

A. Illingworth, R. Hogan, E. O'connor, D. Bouniol, J. Delanoë, J. Pelon, A. Protat, M. Brooks, N. Gaussiat, D. Wilson, et al. Cloudnet: Continuous evaluation of cloud profiles in seven operational models using ground-based observations. *Bulletin of the American Meteorological Society*, 88(6):883–898, 2007.

J. Intrieri, C. Fairall, M. Shupe, P. Persson, E. Andreas, P. Guest, and R. Moritz. An annual cycle of Arctic surface cloud forcing at SHEBA. *Journal of Geophysical Research: Oceans*, 107 (C10), 2002a.

J. Intrieri, M. Shupe, T. Uttal, and B. McCarty. An annual cycle of Arctic cloud characteristics observed by radar and lidar at SHEBA. *Journal of Geophysical Research: Oceans*, 107(C10), 2002b.

K. Jayaweera and T. Ohtake. Concentration of ice crystals in Arctic stratus clouds. *J. Rech. Atmos*, 7:199–207, 1973.

V. Khvorostyanov, J. Curry, J. Pinto, M. Shupe, B. Baker, and K. Sassen. Modeling with explicit spectral water and ice microphysics of a two-layer cloud system of altostratus and cirrus observed during the FIRE Arctic Clouds Experiment. *Journal of Geophysical Research: Atmospheres*, 106(D14):15099–15112, 2001.

A. Korolev. Limitations of the Wegener–Bergeron–Findeisen mechanism in the evolution of mixed-phase clouds. *Journal of the Atmospheric Sciences*, 64(9):3372–3375, 2007.

N. Küchler, S. Kneifel, U. Löhnert, P. Kollias, H. Czekala, and T. Rose. A W-Band Radar–Radiometer System for Accurate and Continuous Monitoring of Clouds and Precipitation. *Journal of Atmospheric and Oceanic Technology*, 34(11):2375–2392, 2017.

D. Lamb and J. Verlinde. *Physics and chemistry of clouds*. Cambridge University Press, 2011.

A. Lampert. Airborne lidar observations of tropospheric Arctic clouds. *Berichte zur Polar-und Meeresforschung (Reports on Polar and Marine Research)*, 608, 2010.

T. Lathem, A. Beyersdorf, K. Thornhill, E. Winstead, M. Cubison, A. Hecobian, J. Jimenez, R. Weber, B. Anderson, and A. Nenes. Analysis of CCN activity of Arctic aerosol and Canadian biomass burning during summer 2008. *Atmospheric Chemistry and Physics*, 13(5):2735–2756, 2013.

R. P. Lawson, B. A. Baker, C. G. Schmitt, and T. Jensen. An overview of microphysical properties of Arctic clouds observed in May and July 1998 during FIRE ACE. *Journal of Geophysical Research: Atmospheres*, 106(D14):14989–15014, 2001.

Lidar. Webpage, 2017. URL `https://mplnet.gsfc.nasa.gov/data?v=V2&s=Ny_Alesund&t=20030605`. Last visited 2017-05-15.

Y. Liu, J. R. Key, R. A. Frey, S. A. Ackerman, and W. P. Menzel. Nighttime polar cloud detection with MODIS. *Remote sensing of environment*, 92(2):181–194, 2004.

Y. Liu, J. R. Key, and X. Wang. Influence of changes in sea ice concentration and cloud cover on recent Arctic surface temperature trends. *Geophysical Research Letters*, 36(20), 2009.

Y. Liu, J. R. Key, S. A. Ackerman, G. G. Mace, and Q. Zhang. Arctic cloud macrophysical characteristics from CloudSat and CALIPSO. *Remote sensing of environment*, 124:159–173, 2012.

K. Loewe. *Arctic mixed-phase clouds: Macro-and microphysical insights with a numerical model*, volume 72. KIT Scientific Publishing, 2017.

D. Lubin and E. Morrow. Evaluation of an AVHRR cloud detection and classification method over the central Arctic Ocean. *Journal of Applied Meteorology*, 37(2):166–183, 1998.

E. P. Luke, P. Kollias, and M. D. Shupe. Detection of supercooled liquid in mixed-phase clouds using radar Doppler spectra. *Journal of Geophysical Research: Atmospheres*, 115(D19), 2010.

M. Maturilli. High resolution radiosonde measurements from station Ny-Ålesund (2017-04,05,06), 2017. URL https://doi.org/10.1594/PANGAEA.879767;https://doi.org/10.1594/PANGAEA.879820;https://doi.org/10.1594/PANGAEA.879822.

M. Maturilli and M. Kayser. Homogenized radiosonde record at station Ny-Ålesund, Spitsbergen, 1993-2014, 2016. URL https://doi.pangaea.de/10.1594/PANGAEA.845373. Supplement to: Maturilli, M; Kayser, M (2017).

M. Maturilli and M. Kayser. Arctic warming, moisture increase and circulation changes observed in the Ny-Ålesund homogenized radiosonde record. *Theoretical and Applied Climatology*, 130 (1-2):1–17, 2017.

M. Maturilli, A. Herber, and G. König-Langlo. Surface radiation climatology for Ny-Ålesund, Svalbard (78.9 N), basic observations for trend detection. *Theoretical and Applied Climatology*, 120(1-2):331–339, 2015.

T. Mauritsen, J. Sedlar, M. Tjernström, C. Leck, M. Martin, M. Shupe, S. Sjogren, B. Sierau, P. Persson, I. Brooks, et al. An Arctic CCN-limited cloud-aerosol regime. *Atmospheric Chemistry and Physics*, 11(1):165–173, 2011.

L. M. Miloshevich, H. Vömel, A. Paukkunen, A. J. Heymsfield, and S. J. Oltmans. Characterization and correction of relative humidity measurements from Vaisala RS80-A radiosondes at cold temperatures. *Journal of Atmospheric and Oceanic Technology*, 18(2):135–156, 2001.

L. M. Miloshevich, A. Paukkunen, H. Vömel, and S. J. Oltmans. Development and validation of a time-lag correction for Vaisala radiosonde humidity measurements. *Journal of Atmospheric and Oceanic Technology*, 21(9):1305–1327, 2004.

G. Mioche, O. Jourdan, J. Delanoë, C. Gourbeyre, G. Febvre, R. Dupuy, M. Monier, F. Szczap, A. Schwarzenboeck, and J.-F. Gayet. Vertical distribution of microphysical properties of Arctic springtime low-level mixed-phase clouds over the Greenland and Norwegian seas. *Atmospheric Chemistry and Physics*, 17(20):12845, 2017.

D. Mironov and B. Ritter. Testing the new ice model for the global NWP system GME of the German Weather Service. *Research Activities in Atmospheric and Oceanic Modelling*, pages 4–21, 2004.

H. Morrison, R. B. McCoy, S. A. Klein, S. Xie, Y. Luo, A. Avramov, M. Chen, J. N. Cole, M. Falk, M. J. Foster, et al. Intercomparison of model simulations of mixed-phase clouds observed during the ARM Mixed-Phase Arctic Cloud Experiment. II: Multilayer cloud. *Quarterly Journal of the Royal Meteorological Society*, 135(641):1003–1019, 2009.

H. Morrison, G. De Boer, G. Feingold, J. Harrington, M. D. Shupe, and K. Sulia. Resilience of persistent Arctic mixed-phase clouds. *Nature Geoscience*, 5(1):11–17, 2012.

D. Murphy and T. Koop. Review of the vapour pressures of ice and supercooled water for atmospheric applications. *Quarterly Journal of the Royal Meteorological Society*, 131(608):1539–1565, 2005.

Noahhowell. Map, 2018. URL http://www.noahhowell.com/wp-content/uploads/2011/06/Screen-shot-2011-04-26-at-6.25.20-PM.png. Last visited 2018-02-05.

Norwegian Polar Institute. Map, 2018. URL http://toposvalbard.npolar.no/. Last visited 2018-02-04.

D. Notz. *Thermodynamic and fluid-dynamical processes in sea ice*. PhD thesis, University of Cambridge, 2005.

T. Nygård, T. Valkonen, and T. Vihma. Antarctic low-tropospheric humidity inversions: 10-yr climatology. *Journal of Climate*, 26(14):5205–5219, 2013.

T. Nygård, T. Valkonen, and T. Vihma. Characteristics of Arctic low-tropospheric humidity inversions based on radio soundings. *Atmospheric Chemistry and Physics*, 14(4):1959–1971, 2014.

O. Persson and T. Vihma. The atmosphere over sea ice. *Sea Ice*, pages 160–196, 2017.

G. W. Petty. *A first course in atmospheric radiation*. Sundog Pub, 2006.

J. Reisner, R. M. Rasmussen, and R. Bruintjes. Explicit forecasting of supercooled liquid water in winter storms using the MM5 mesoscale model. *Quarterly Journal of the Royal Meteorological Society*, 124(548):1071–1107, 1998.

B. Ritter and J.-F. Geleyn. A comprehensive radiation scheme for numerical weather prediction models with potential applications in climate simulations. *Monthly Weather Review*, 120(2): 303–325, 1992.

J. Savre, A. M. Ekman, G. Svensson, and M. Tjernström. Large-eddy simulations of an Arctic mixed-phase stratiform cloud observed during ISDAC: sensitivity to moisture aloft, surface fluxes and large-scale forcing. *Quarterly Journal of the Royal Meteorological Society*, 141 (689):1177–1190, 2015.

U. Schättler, G. Doms, and C. Schraff. Description of the Nonhydrostatic Regional COSMO Model, Part VII: User's guide, 2016.

J. Sedlar, M. D. Shupe, and M. Tjernström. On the relationship between thermodynamic structure and cloud top, and its climate significance in the Arctic. *Journal of Climate*, 25(7):2374–2393, 2012.

A. Seifert and K. Beheng. A two-moment cloud microphysics parameterization for mixed-phase clouds. Part 1: Model description. *Meteorology and atmospheric physics*, 92(1):45–66, 2006.

M. C. Serreze, A. P. Barrett, A. G. Slater, M. Steele, J. Zhang, and K. E. Trenberth. The large-scale energy budget of the Arctic. *Journal of Geophysical Research: Atmospheres*, 112(D11), 2007.

M. Shupe, P. Persson, I. Brooks, M. Tjernström, J. Sedlar, T. Mauritsen, S. Sjogren, and C. Leck. Cloud and boundary layer interactions over the Arctic sea ice in late summer. *Atmospheric Chemistry and Physics*, 13:9379–9400, 2013.

M. D. Shupe. A ground-based multisensor cloud phase classifier. *Geophysical Research Letters*, 34(22), 2007.

M. D. Shupe and J. M. Intrieri. Cloud radiative forcing of the Arctic surface: The influence of cloud properties, surface albedo, and solar zenith angle. *Journal of Climate*, 17(3):616–628, 2004.

M. D. Shupe, T. Uttal, and S. Y. Matrosov. Arctic cloud microphysics retrievals from surface-based remote sensors at SHEBA. *Journal of Applied Meteorology*, 44(10):1544–1562, 2005.

M. D. Shupe, S. Y. Matrosov, and T. Uttal. Arctic mixed-phase cloud properties derived from surface-based sensors at SHEBA. *Journal of the atmospheric sciences*, 63(2):697–711, 2006.

P. Smithson, K. Addison, and K. Atkinson. *Fundamentals of the physical environment*. Routledge, 2013.

G. Sotiropoulou, J. Sedlar, M. Tjernström, M. D. Shupe, I. M. Brooks, and P. O. G. Persson. The thermodynamic structure of summer Arctic stratocumulus and the dynamic coupling to the surface. *Atmospheric Chemistry and Physics*, 14(22):12573–12592, 2014.

P. Spichtinger, K. Gierens, and W. Read. The global distribution of ice-supersaturated regions as seen by the Microwave Limb Sounder. *Quarterly Journal of the Royal Meteorological Society*, 129(595):3391–3410, 2003.

M. Tjernström, C. Leck, C. Birch, I. Brooks, M. Shupe, P. Persson, C. Wheeler, J. Sedlar, T. Mauritsen, J. Paatero, et al. Meteorological conditions in the central Arctic summer during the Arctic Summer Cloud Ocean Study (ASCOS). *Atmospheric Chemistry and Physics*, 12(15): 6863–6889, 2012.

M. Tjernström, C. Leck, C. E. Birch, J. W. Bottenheim, B. J. Brooks, I. M. Brooks, L. Bäcklin, R.-W. Chang, G. de Leeuw, L. Di Liberto, et al. The Arctic Summer Cloud Ocean Study (ASCOS): overview and experimental design. *Atmospheric Chemistry and Physics*, 14(6):2823–2869, 2014.

R. Treffeisen, R. Krejci, J. Ström, A.-C. Engvall, A. Herber, and L. Thomason. Humidity observations in the Arctic troposphere over Ny-Ålesund, Svalbard based on 15 years of radiosonde data. *Atmospheric Chemistry and Physics*, 7(10):2721–2732, 2007.

S.-C. Tsay and K. Jayaweera. Physical characteristics of Arctic stratus clouds. *Journal of climate and applied meteorology*, 23(4):584–596, 1984.

T. Uttal, J. A. Curry, M. G. Mcphee, D. K. Perovich, R. E. Moritz, J. A. Maslanik, P. S. Guest, H. L. Stern, J. A. Moore, R. Turenne, et al. Surface heat budget of the Arctic Ocean. *Bulletin of the American Meteorological Society*, 83(2):255–275, 2002.

J. Verlinde, J. Y. Harrington, V. Yannuzzi, A. Avramov, S. Greenberg, S. Richardson, C. Bahrmann, G. McFarquhar, G. Zhang, N. Johnson, et al. The mixed-phase Arctic cloud experiment. *Bulletin of the American Meteorological Society*, 88(2):205–221, 2007.

J. Verlinde, M. P. Rambukkange, E. E. Clothiaux, G. M. McFarquhar, and E. W. Eloranta. Arctic multilayered, mixed-phase cloud processes revealed in millimeter-wave cloud radar Doppler spectra. *Journal of Geophysical Research: Atmospheres*, 118(23), 2013.

D. M. Winker, J. Pelon, and M. P. McCormick. The CALIPSO mission: Spaceborne lidar for observation of aerosols and clouds. In *Proc. Spie*, volume 4893, pages 1–11, 2003.

T. Yamanouchi, R. Treffeisen, A. Herber, M. Shiobara, S. Yamagata, K. Hara, K. Sato, M. Yabuki, Y. Tomikawa, A. Rinke, et al. Arctic study of tropospheric aerosol and radiation (ASTAR) 2000: Arctic haze case study. *Tellus B*, 57(2):141–152, 2005.

Acknowledgements

A special thanks goes to Prof. Dr. Corinna Hoose for having the brilliant idea of studying Arctic Multilayer Clouds. All her input has been essential for this work.
I am very thankful that Prof. Dr. Christoph Kottmeier is the correferent for this thesis. His knowledge about the polar regions will be of great value.
I would like to thank Dr. Luisa Ickes extraordinarily for all the discussions about further steps, upcoming problems and results. Here continuous participation has been crucial to this work. Further, I would also like to thank her for making my stay in Stockholm such a nice and successful experience.
I am grateful that I had the opportunity to spend 2.5 months at MISU (Department of Meteorology at Stockholm University). I would especially like to thank the professors Annica Ekman, Michael Tjernström and Gunilla Svensson for their scientific input. Additionally, I would like to thank all the fantastic people at MISU for including me in a lovely way to all their social activities.
I would like to thank Kerstin Ebell from the University of Cologne for providing the Radar and Cloudnet Data. The Radar is part of the (AC)³ project, which is funded by the German Research Foundation (DFG, Deutsche Forschungsgemeinschaft). The classification is part of the Cloudnet project (European Union contract EVK2-2000-00611).
I would also like to thank the cloud physics group at IMK-TRO for helping me setting up the model and always coming up with new and helpful input during group meetings and conversations.
A special thank goes also to my friends and family always supporting me and believing in me.

Erklärung

Ich versichere wahrheitsgemäß, die Arbeit selbstständig angefertigt, alle benutzten Hilfsmittel vollständig und genau angegeben und alles kenntlich gemacht zu haben, was aus Arbeiten anderer unverändert oder mit Abänderungen entnommen.

Karlsruhe, den 08. 02. 2018

Maiken Vassel